Time-Domain Simulations of Aerodynamic Forces on Three-Dimensional Configurations, Unstable Aeroelastic Responses, and Control by Neural Network Systems

Zhicun Wang

Dissertation submitted to the Faculty of the

Virginia Polytechnic Institute and State University

in partial fulfillment of the requirements for the degree of

Doctor of Philosophy

in

Engineering Mechanics

Dean T. Mook, Chair

David Y. Gao

Muhammad R. Hajj

Scott L. Hendricks

Liviu Librescu

Sergio Preidikman

May 7, 2004

Blacksburg, Virginia

Keywords: Aeroelasticity, Aerodynamics, Vortex-lattice Method, Flutter, Rigid-Body Motion, Neural Network Control

Time-Domain Simulations of Aerodynamic Forces on Three-Dimensional Configurations, Unstable Aeroelastic Responses, and Control by Neural Network Systems

Zhicun Wang

(ABSTRACT)

The nonlinear interactions between aerodynamic forces and wing structures are numerically investigated as integrated dynamic systems, including structural models, aerodynamics, and control systems, in the time domain. An elastic beam model coupled with rigid-body rotation is developed for the wing structure, and the natural frequencies and mode shapes are found by the finite-element method. A general unsteady vortex-lattice method is used to provide aerodynamic forces. This method is verified by comparing the numerical solutions with the experimental results for several cases; and thereafter applied to several applications such as the inboard-wing/twin-fuselage configuration, and formation flights. The original thought that the twin fuselage could achieve two-dimensional flow on the wing by eliminating free wing tips appears to be incorrect. The numerical results show that there can be a lift increase when two or more wings fly together, compared to when they fly alone. Flutter analysis is carried out for a High-Altitude-Long-Endurance aircraft wing cantilevered from the wall of the wind tunnel, a full-span wing mounted on a free-to-roll sting at its mid-span without and with a center mass (fuselage). Numerical solutions show that the rigidity added by the wall results in a higher flutter speed for the wall-mounted semi-model than that for the full-span model.

In addition, a predictive control technique based on neural networks is investigated to suppress flutter oscillations. The controller uses a neural network model to predict future plant responses to potential control signals. A search algorithm is used to select the best control input that optimizes future plant performance. The control force is assumed to be given by an actuator that can apply a distributed torque along the spanwise direction of the wing. The solutions with the wing-tip twist or the wing-tip deflection as the plant output show that the flutter oscillations are successfully suppressed with the neural network predictive control scheme.

Acknowledgements

I would like to express my greatest gratitude and appreciatation to my advisor, Dr. Dean T. Mook. who has not only guided and supported me with my Ph.D. study, but also has always been willing to help me with any problems that I have had. His insight into problems both academic and others has been a great source of advice and inspiration. I have enjoyed the flights with Dr. Mook, during which I have viewed the beautiful scenes of the land of Virginia, and at the same time could think about the aerodynamic and aeroelastic theories behind the real situations. I am so lucky to have you, Dr. Mook, as my advisor.

I am also very grateful to the members of my advisory committee, Dr. David Y. Gao, Dr. Muhammad R. Hajj, Dr. Scott L. Hendricks, Dr. Liviu Librescu, and Dr. Sergio Preidikman. The outstanding instructions that they have provided in Mathematics, Turbulent Flow, Dynamics, and Theory of Plates and Shells have greatly advanced my level of understanding in applied mechanics, and have always left me wondering when I will be able to, like them, know everything and have unfading memories. Especially, I would like to thank Dr. Preidikman for his excellent work which forms the solid ground of my dissertation research.

I am very grateful to Dr. Ali H. Nayfeh, who at one time served in my advisory committee. The knowledge that I gained from his Perturbation and Nonlinear System classes is immeasurable. Nonlinearity will always be hanging around my mind.

I sincerely thank Dr. Romesh Batra for giving me an opportunity to work on an impact problem, by which I could further my understanding of non-linear elasticity and finite-element modeling.

I am also indebted to Sally Shrader, Joyce Smith, and Loretta Tickle for their continuous help during my stay at the department of Engineering Science and Mechanics. They have been accessible, always gladly taking time to help me with all sorts of tedious problems.

Finally, I thank my beloved wife Yutao and my lovely daughter Lu for their accompanying through these years. Without their support and encouragement, my education

and life in America would not be imaginable.

Contents

List of Figures

x

List of Tables

Chapter 1

Introduction and Literature Review

1.1 Introduction

The subject of this dissertation is to continue the development of numerical simulations of nonlinear unsteady aerodynamics/structural interactions.

The effect of aerodynamic forces on elastic bodies forms the subject of aeroelasticity, which is obviously a multidisciplinary subject. To facilitate our discussion, we begin with the famous Collar's diagram of triangle shown in Figure 1-1. The three vertices in the diagram are Elasticity, Aerodynamics, and Dynamics. Each one of them represents a subject of interest individually. Combining either two of them or all of them yields different aspects of aeroelastic analysis.

When considering only elasticity and aerodynamics, it means that the wing is treated as an elastic body subjected to an aerodynamic force which is considered in steady state. This is a static aeroelasticity problem. Two typical examples are wing-divergence phenomenon and reversal of ailerons, which are static instabilities of a lifting surface of an aircraft in flight. At low speeds of flight, the effect of elastic deformation is small. But at higher speeds, the effect of elastic deformation can become so serious as to cause a wing to be unstable, or to render a control surface ineffective, or even to reverse the sense of control.

Aerodynamics and Dynamics together give us a classical aerodynamics analysis. In

this case, the aircraft or the wing is assumed rigid; no elastic deformation is induced. In the helicopter or wind mill industries, when analyzing the blades, this is a very typical approach.

All three subjects together are needed to solve an unsteady aeroelastic problem such as flutter phenomena and buffeting. To give a concise definition for flutter, it is a dynamic instability occurring in an aircraft in flight. At a speed called the flutter speed, the interaction between elastic deformations and aerodynamics causes a sustained oscillation of the wing or control surfaces; see Bisplinghoff *et al.* (1955) and Fung (1955).

The phenomenon of flutter has been observed from the early days of powered flights as well as in civil engineering. The oscillations associated with flutter can be very serious and sometimes catastrophic. A well-known flutter example happened on November 7, 1940, when the Tacoma Narrows bridge in the State of Washington was destroyed by wind action. Since then, aeroelasticity has been a very important factor in the design of long-span suspension bridges.

The oscillatory motion of a fluttering wing, in general, involves the coupling of several degrees of freedom. A rigid airfoil so constrained as to have only the deflection, which simulates the flexural degree of freedom, does not flutter. A rigid airfoil with only the torsional degree of freedom can flutter only if the angle of attack is at or near the stalling angle. The coupling between various degrees of freedom accounts for the phase shift between the motions in those degrees of freedom. Experiments on cantilever wings show that the flexural motions at all points across the span are approximately in phase with one another, and likewise the torsional motions are all approximately in phase, but the deflection is considerably out of phase from the torsional motion. This phase difference at the critical flutter speed brings about the flutter in such a way that energy can be extracted from the airstream passing by.

In this dissertation, we focus on the flutter problem. Flutter analysis is very challenging because of its inherent coupling and nonlinear characteristics. One can not determine the structural response without first knowing the applied loads, and on the other hand, one can not calculate the aerodynamic loads on a body without first knowing the state

(position, velocity) of that body.

Because of the inherent complexity of the aeroelastic problem, one often seeks some simplicity, either in the part of structural model, or the aerodynamic part, or both of them. A very common approach in flutter analysis is to solve in the frequency domain. The aerodynamic forces are given by Theodorsen's (1935, 1940) method, in which the wing or airfoil is assumed to have simple-harmonic motion. This approach has been very successful to predict the flutter speed as well as the flutter frequency. However, it is limited to predict the onset of flutter; it can not tell us the behavior of the aircraft or the wing thereafter.

We will proceed with our flutter analysis in the time domain. The governing equations of the whole dynamic system, including the control system if there is any, will be integrated simultaneously and interactively in time. To further the analysis for flutter, we intend to include the rigid-body motion, especially the rolling motion of air-vehicles, into the structural model, and investigate the effects of this inclusion. As a numerical example, we analyze a High-Altitude-Long-Endurance (HALE) aircraft wing model same as the one in Hall (1999 and 2001). HALE aircraft are intended for observation, communication, and other applications. Though there may be other options, one is led immediately to consider very lightweight, high-aspect wings in order to acquire the needed aerodynamic efficiency. Most likely, such wings will also be very flexible and, hence, experience large, by current standards at least, deflections. The large deflections will significantly affect both the static and dynamic loads. In this dissertation, we present an inherently nonlinear method for numerically simulating the steady and unsteady behavior of large flexible wings flying in the subsonic regime.

1.2   Literature Review

We divide our literature review into three major topics:

- Research related to aerodynamics and aeroelasticity.

- Research related to the elastic beam model.

3

• Research related to neural network control.

1.2.1   Research Related to Aerodynamics and Aeroelasticity

Aerodynamics plays a very important role in this dissertation research. A version of one aerodynamic model, the so-called unsteady vortex-lattice method (UVLM), has been developed at Virginia Tech over years to solve for the incompressible flow over both lifting and nonlifting bodies. The method utilizes a lattice of discrete vortex lines (bound vortices) distributed over surfaces of the configuration. The circulations around the discrete vortex segments are obtained by imposing the no-penetration condition on the body surfaces. Imposing the unsteady Kutta condition along the edges where separation occurs provides the vorticity (free vortices) shedding rate, and convecting the vorticity in the wake with the local particle velocity renders the wake force-free. The advantages of this method are that it also satisfies the no-slip condition and readily provides the surface velocity and pressure, and it is not restricted by planform, camber, twist, dihedral angle, sink rate, angle of attack, etc., as long as separation occurs only along known lines and vortex bursting does not occur near the configuration.

This version of the unsteady vortex-lattice method deals with inviscid flow where compressibility effects are practically negligible. This means that we may regard the fluid as incompressible besides being inviscid. i.e., an ideal fluid. Naturally, no real fluid is an ideal fluid. However, under many practically interesting situations, the motion of a real fluid may be analyzed to a high degree of accuracy by regarding the fluid as an ideal fluid (Karamcheti (1980)). In addition to incompressibility, we also assume the flow is irrotational. Among the theories behind the UVLM, Helmholtz (1858) theory is an essential one, which states that, *in the motion of an ideal fluid subjected to irrotational body forces, the material rate of change of the circulation around any surface element moving with the fluid is permanently zero, or, equivalently, the circulation around any surface element moving with the fluid remains a constant for all times.* Helmholtz also showed that flows with vorticity can be modeled with vortices of appropriate circulation and infinitely small cross section. It is this result that led to the discretization of the compact

regions of vorticity into an assembly of vortices embedded in an otherwise potential flow. An excellent review of the vortex methods, including the fundamental theories as well as practical applications can be seen in the work by Sarpkaya (1989).

Vortex-lattice methods were first formulated in the late 1930's, and the method was first called "Vortex Lattice" in 1943 by Faulker. In the early 1960's this method was widespread adopted due to its simplicity without lacking the sufficient insight to the flow as well as the calculating capability at that time. Several versions of vortex-lattice code were developed at NASA Langley: by Margason and Lamar (1971); by Lamar and Gloss (1975); and by Lamar (1982) and Herbert (1982). Each new version had considerably more capability than the previous version. The original codes could handle two lifting surfaces, while the "final" development in this series could handle four. Like all the traditional vortex-lattice methods, these codes use horse-shoe type of vortices, and assume the wing wake coming from the trailing edge and wing tips remains flat and aligned with the freestream. This assumption is acceptable for many cases. The effect of the wake on the wing that generates it is small unless the wing is highly loaded. However, the interaction between the wake from an upstream surface and a trailing lifting surface can be influenced by the roll-up and position of the wing-tip vortices. To improve the accuracy of the vortex-lattice method, many variations have been proposed. They either improve in the area of convergence, or the positioning of the wake. Hough (1973) demonstrated that improvement in accuracy could be achieved by using a lattice that was slightly smaller than the true planform area with the assumption of flat wake kept. Basically, he proposed a 1/4 panel width inset from the tips.

The unsteady vortex lattice method developed at Virginia Tech gives the wake position as part of the solution to ease the problem associated with the flat wake assumption. This method has been successfully used to many applications. Among these applications, some coupled the aerodynamic model with the elastic structural model or the dynamic motion of the surface or body. Mook and Maddox (1974) included the effects of leading-edge separation on highly swept wings. Although the leading-edge free vortex sheet was force free, the free vortex sheet from the trailing edge was not. Kandil (1974) and Kandil,

Mook, and Nayfeh (1976) developed an unsteady, nonlinear numerical method to predict the aerodynamic loads on rectangular and delta wings with sharp-edge separations. They found excellent agreement between their simulations and the experimental results of Peckham (1958) for steady flows. Thrasher *et al.* (1977) expressed the problem in a body-fixed coordinate system and allowed the wings to perform arbitrary maneuvers. Thrasher (1979) combined the aerodynamics model with a predictor-corrector method to simultaneously predict the flow field, the motion of a hinged rectangular wing, and to predict the aerodynamic forces under the prescribed motion of a flap. Atta *et al.* (1977) analyzed delta wings and developed a higher order theory for the convection process of the wake. Nayfeh *et al.* (1979) presented a modification of the vortex-lattice method to treat small harmonic oscillations about a delta wing at a nominal 15 deg. angle of attack. The circulations around the wing were calculated and the results were in close agreement with those obtained with a general, and therefore less efficient, unsteady approach. Konstadinopoulos (1984) and Konstadinopoulos *et al.* (1983, 1985) simulated one degree of freedom subsonic wing-rock problem. Wing rock occurs at high angles of attack and low Mach numbers; hence, assuming the flow is incompressible is reasonable. A flat delta wing free to roll around an axis parallel to its mid-span chord was studied. UVLM was used to provide the aerodynamic loads, and the equation of motion was integrated in the time domain along with the aerodynamics. The numerical solutions are in excellent agreement with the experimental results of Nguyen *et al.* (1980, 1981) and Levin and Katz (1982). Elzebda (1987) and Elzebda *et al.* (1989) expanded the method to study the two-degree-of-freedom subsonic wing-rock problem, considering coupled pitching and rolling motion of a slender delta wing. Mracek and Mook (1991) developed a vortex-panel method to calculate aerodynamic forces, and combined this model with the equations of motion as well as the control inputs. The vortex panel method in this work uses triangular panels with linearly varying tangential velocity to model the surface of the body, and a mesh of discrete vortex lines to model the wakes. A thin delta wing free to rotate about the sting attachment point was simulated and the control of the pitch angle of the wing was investigated. Elzebda *et al.* (1985, 1994) extended the general unsteady vortex-lattice

method to model flows over an arbitrary number of lifting surfaces. Each lifting surface can have its own motion independent of the others. A configuration similar to that of the X-29 was analyzed, and the steady solutions excellently agree with the experimental data from AEDC and Grumman. Atta and Nayfeh (1978) used the unsteady vortex-lattice method to calculate the aerodynamic loads on a wing-body configuration. When calculating the pressure on the fuselage by using Bernoulli's equation, the derivative with respect to time of the velocity potential was set to zero. Karkehabadi (1995) analyzed the aerodynamic loads acting on one small wing (a Cessna 750's wing) operating near the wake of another wing (a Boeing 757) by using the unsteady vortex-lattice method. Following the theory developed by Weiselsberger (1922), Nuhait (1988) and Nuhait and Mook (1989) placed an image of the real wing and its wake below the ground plane to simulate steady and unsteady ground effect. The authors found close agreement between their numerical simulations and the limited exact solutions and experimental data.

Kim (1985), Kim and Mook (1986), Mracek (1988a), and Mracek and Mook (1988b) extended the vortex-lattice method to a vorticity-panel method. Instead of using discrete lattices, they used distributed vorticity on triangular panels to imitate the boundary layers on the surface of the body. The small improvements in the results did not justify the complications involved in the programming. Strganac and Mook (1986, 1987a, 1987b, 1990) and Strganac (1987c) used the vortex-lattice method and a predictor-corrector numerical integration algorithm to solve the aeroelastic problems for a rigid wing and an elastic wing. The innovation in these works is to integrate simultaneously and interactively the equations of motion of the structure and the flowfield. Dong (1991) and Mook and Dong (1994) used feedback control to suppress the flutter of a two-dimensional airfoil. More recently, Preidikman (1998) and Preidikman and Mook (2000) investigated the flutter problem for an airplane, Cessna Citation 10. During their research, they coupled the vortex-lattice method with a MSC/NASTRAN finite-element structural model. Limit cycles were found after the onset of flutter and the amplitudes of the limit cycles grow as the speed increases. Instability appeared to be a supercritical Hopf bifurcation. Also, a secondary bifurcation was observed. Hall (1999) and Hall et $al.$ (2001) applied the

vortex-lattice method to a HALE aircraft wing, and suppress the flutter oscillations and the vibrations caused by gusts by employing a novel nonlinear controller which is based on the phenomenon of saturation that may exist in nonlinear systems with two-to-one internal resonances.

Besides the vortex-lattice method used to solve potential flow problem, there are other approaches, such as the panel methods, to name a few, VSAERO and PMARC are two famous codes.

1.2.2   Research Related to Beam Models

We constrain our structural model as a beam model. Previous flutter analyses have used a cantilever wing in bending and torsion about its elastic axis, see Preidikman (1998) and Hall (1999). However, when predicting the flutter of unrestrained aircraft, we often encounter situations where the mass or moment of inertia of some lifting surface is a large fraction of the mass or corresponding moment of inertia of the entire aircraft. It is then very likely that certain rigid-body motions contribute appreciably to the flutter mode. Thus we would like to derive a beam model with rigid body motion included, in particular the rolling motion of the aircraft. Technically it is a problem of an elastic beam attached to a moving base, which, in our case, is a fuselage; or a problem of a flexible beam undergoing overall motions. Research on this area is very broad and is in connection with a number of diverse disciplines, such as rotating shafts, spacecraft with flexible solar panels and antennae, and robots with both rigid and elastic links.

Bisplinghoff and Ashley (1955) derived scalar equations of motion for an unrestrained flexible vehicle. The equations consisted of three inertially decoupled sets, one for the rigid body translations, one for the rigid body rotations, and one for the elastic deformations; the latter was expressed in terms of aircraft structural natural modes. The inertia matrix was assumed to be constant, which implies that the contributions from the elastic deformations to the inertia matrix were ignored.

A more general approach for formulating the equations of motion is the use of the so-called shadow or tracking frame (Baruh (1999)). The elastic deformations of the beam

are observed in the tracking frame. The motion of the tracking frame is referred to as the primary motion, the overall motion; and the motion observed from the frame, i.e., the elastic deformation is referred to as the secondary motion. Using the tracking frame approach, one can easily define the strain-energy function and the kinetic energy although the inertia terms are highly nonlinear and coupled. Many researchers follow this approach, such as Simo and Vu Quoc (1986), Simo (1985), Kane *et al.* (1987), Beberjee *et al.* (1989), and Yoo *et al.* (1995). They either used assumed modes or the finite-element method to discretize the elastic deformations in the space domain. One shortcoming in some of the papers lies in the fact that the inertial coupling of elastic bending and torsion was neglected, which actually is a very important aspect in the flutter analysis for aircraft, or the fact that torsion was simply not considered.

Merirovitch (1966, 1991, 1993, 1995, 1997, 2001, 2002) and his colleagues have done a lot of research in this area. They used a concept of quasi-coordinates to develop the hybrid (ordinary, partial differential and integral) equations of motion coupling rigid-body translations and rotations with elastic deformations. The elastic deformations were measured relative to a set of body axes attached to the undeformed spacecraft or aircraft. The rotational and translational motions were in terms of quasi-coordinates. In Merirovitch *et al.* (2002), they used a perturbation approach to separate the state equations into a set of nonlinear flight dynamics equations for the rigid body variables and a set of linear extended aeroelasticity equations for the elastic variables and perturbations in the rigid-body variables. The aerodynamic forces were involved in the development of equations, and they chose a very simple strip theory to get them; thus, their approach cannot predict the limit-cycle oscillations (LCO).

Discussions on rotary-wing aeroelasticity, where centrifugal effects play an important role, can be found in Dowell *et al.* (1995), Ormiston (1988), Crespo da Silva and Hodges (1986), and Kaza and Kvaternik (1977).

1.2.3 Research Related to Neural Network Control

Inspired by biological nervous systems, neural networks, sometimes also called artificial neural networks, are composed of simple elements, neurons, operating in parallel to perform a certain task. As in nature these neurons are interconnected to each other, and the strength of the interconnections is quantified by means of interconnection weights. By adjusting or training the weights, neural networks can perform tasks such as object and pattern recognition, speech recognition or associative memory, modelling and control, optimization, and financial applications. The field of neural networks has a history of some five decades and has gained a widespread application especially in the past fifteen years. There are some very good books giving the introduction and applications of neural networks, to name a few, Hagan, Demuth and Beale (1995), Haykin (1994), and Suykens *et al.* (1996).

Neural networks are thought to begin with the work of McCulloch and Pitts (1943), who showed that networks of artificial neurons could, in principle, compute any algorithmic or logical function. Rosenblatt (1958) and his colleagues built a perceptron network to perform pattern recognition. Widow and Hoff (1960) introduced a linear network, ADALINE (ADAaptive LInear NEuron), and a learning rule which they called the LMS (Least Mean Square) algorithm. Kohonen (1972) and Anderson (1972) developed neural networks that could act as memories. Hopfiled (1982) showed that neural networks are capable of solving a large number of problems of the traveling salesman type by means of an energy function. Rumelhart (1986) rediscovered the backpropagation training algorithm, which is the key development in the research of neural networks. It solved the training problem for multilayer nonlinear networks.

The characteristics associated with multilayer neural networks make them very suitable in the modelling and control of nonlinear systems. Those features include inherent nonlinearity, parallel distributed processing, generalizing ability with adapting weights. Several types of neural network architecture can be used for identification and control of the system. One type of the architecture operates with static networks associated with output feedback control law, where there is no on-line training or learning for the weights

of the network. The network is trained off-line. Liut *et al.* (1999*a*, 1999*b*) demonstrated this approach to suppress the rolling motion of a ship and the seismic response of buildings by using two new-backpropagation-based training algorithm: a load-matching procedure and an adaptive gradient search, which eliminate the need of overall system identification. The others include Model Predictive Control, Feedback Linearization Control and Model Reference Control, etc. These types of architecture typically require two steps: first, system identification; second, control design. In the system identification stage, one develops a neural network model of the plant. In the control design stage, one uses the neural network plant model to design or train the controller. Because model reference control can apply to a larger class of plant, it sometimes has preference over the other architectures. However the use of dynamic backpropagation algorithm (see Narendra *et al.* (1991)) is very computational expensive. Applying neural network control to suppress flutter oscillation or the aeroelasticity area has gained considerable attention. Bernelli-Zazzera *et al.* (1997, 1999, 2000) used recurrent neural networks to actively suppress flutter exploiting online training. Aerodynamic forces were first solved in the frequency domain then transferred to the time domain through a finite state approximation. Scott and Pado (2000) investigated the use of neural networks for controlling the aeroelastic response of a wind-tunnel model. Three neural-network-based control systems were developed and tested. One system used a neural network to schedule flutter suppression control laws, another employed a neural network in a predictive scheme, and the third employed a neural network in an inverse model control scheme. Natarajan *et al.* (2002) studied adaptable airfoils by using neural network systems. Aerodynamic forces were given by a doublet-panel method.

In the course of this dissertation, we employ a neural network predictive control model to suppress flutter oscillation.

1.3 Contributions of this Work

The main contributions and achievements of this work include the following problems attempted for the first time and those re-visited:

- Development of the elastic beam model coupled with the rigid body motion.

- Modal analysis for the beam model by using the finite element method.

- Modification of the aerodynamic code to facilitate multi-configuration analysis.

- Aerodynamic analysis for the flow past a spherically blunted cylinder-cone configuration.

- Aerodynamic analysis for the flow past a mid-wing/single-fuselage configuration.

- Aerodynamic analysis for the flow past rectangular wings.

- Aerodynamic analysis for an inboard-wing/twin-fuselage configuration.

- Aerodynamic analysis for formation flights.

- Stability analysis for the hitchhiker wing.

- Flutter analysis of a HALE aircraft wing cantilevered from the wall of the wind tunnel.

- Flutter analysis of a HALE aircraft wing mounted on a free-to-roll sting at its mid-span without a center mass.

- Flutter analysis of a HALE aircraft wing mounted on a free-to-roll sting at its mid-span with a center mass.

- System identification with a neural network for the HALE aircraft wing cantilevered from the wall of the wind tunnel.

- Flutter suppression by using neural network predictive control.

1.4 Organization of the Dissertation

In Chapter 2, the structural model is developed. The wing is modeled as an Euler-Bernouli beam which includes an overall rigid body rolling motion. The natural frequencies and free-vibration modes are given for a HALE aircraft wing model. In Chapter 3, the general unsteady vortex-lattice method used to predict unsteady aerodynamic forces is described. Numerical examples for verification of the developed code as well as some applications are presented. Chapter 4 introduces the technique to combine the structural model and aerodynamic model and the integration algorithm. The numerical aeroelastic simulations for the HALE aircraft wing under three cases are presented. In Chapter 5, a neural network predictive control model is introduced and implemented to suppress flutter for the cantilevered HALE aircraft wing model. Finally, the conclusions and further remarks are given in Chapter 6.

The figures related to each chapter are included at the end of the chapter. The references are shown at the end of the dissertation, followed by the authors's vita. The references appear in alphabetical order, and they are also numbered.
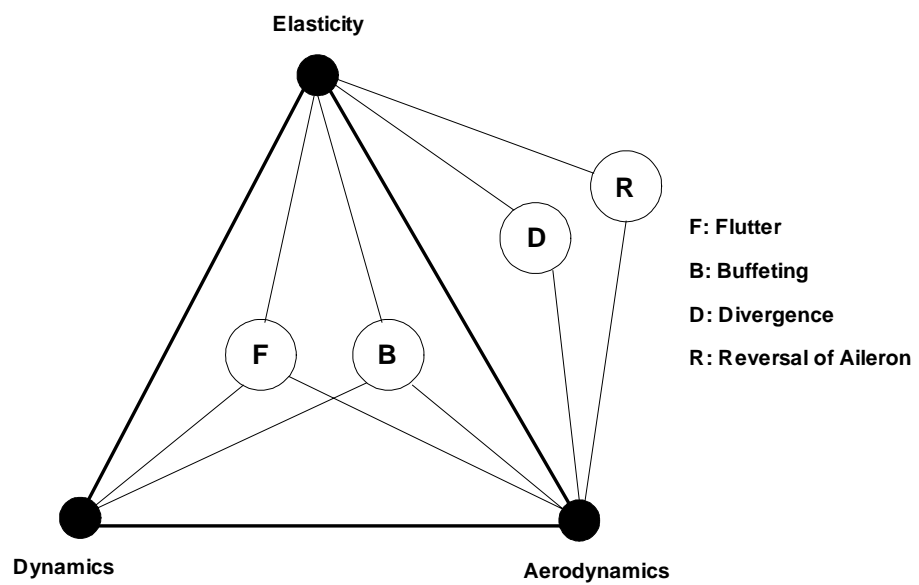
Figure 1-1: The aeroelastic triangle of subjects

Chapter 2

Structural Model

We model the aircraft's wing structurally as an Euler-Bernoulli beam, but not a cantilever one by including an overall rigid-body rolling motion. It will simulate a wind-tunnel experiment in which a wing is mounted on a free-to-roll sting at its mid-span chord.

When both elastic deformation and rigid-body motion are small, one can use linear theory and the principle of superposition for the entire motion. However, there are certain situations, in which the principle of superposition is not appropriate, such as the case of large rigid body motions. We use a more generalized approach, the so-called shadow or tracking frame method, to model a beam undergoing an overall motion.

2.1   Development of the Equations of Motion

The beam to be analyzed, shown in Figure 2-1, consists of a rigid mass attached at F, which represents the fuselage, and the left and right wings attached to the fuselage as cantilever beams. The n-system with base vectors $(\overrightarrow{n_1}, \overrightarrow{n_2}, \overrightarrow{n_3})$ is the inertial coordinate system. The a-system with base vectors $(\overrightarrow{a_1}, \overrightarrow{a_2}, \overrightarrow{a_3})$, in which the wing's elastic deformation is defined, is rigidly attached to the center mass and so undergoes a rolling motion around the $\overrightarrow{a_1}$-axis, which makes an angle of attack with the free stream. Also shown is an expanded view of beam's (wing's) cross section a distance y from F. Following the suggestion of an airframe manufacturer, we assume that all of the cross sections remain

undeformed, and each has a local coordinate system, all of which are called the b-system with base vectors $(\overrightarrow{b_1}, \overrightarrow{b_2}, \overrightarrow{b_3})$ and oriented such that $\overrightarrow{b_2}$ is coincident with the elastic axis of the beam, while $\overrightarrow{b_1}$ and $\overrightarrow{b_3}$ are the principal axes of the cross section. Points B and C are the elastic and the mass centers of the cross section, respectively. When the beam (or the wing) is undeformed, the a-system and all of the b-systems are parallel.

To use the extended Hamilton's principle to develop the governing equations, we need to determine the kinetic and potential energies of the system. We begin with the velocity expression of the mass center C of the cross section at the location y.

The position vector of the centroid C is:

$$\overrightarrow{OC} = \overrightarrow{OF} + \overrightarrow{FB} + \overrightarrow{BC} \tag{2.1}$$

where $\overrightarrow{BC}$ is the eccentricity vector; that is

$$\overrightarrow{BC} = r_x \overrightarrow{b_1} + r_z \overrightarrow{b_3} \tag{2.2}$$

and

$$\overrightarrow{FB} = y \overrightarrow{a_2} + u_1 \overrightarrow{a_1} + u_2 \overrightarrow{a_2} + u_3 \overrightarrow{a_3} \tag{2.3}$$

where u_1, u_2, u_3 are the elastic deformation displacements; among them, u_1 and u_3 represents bending deflections, while u_2 is the extension.

In order to differentiate the position vector to get the velocity, we need the angular velocity of each coordinate system. System a's angular velocity is given by

$$^n\underline{\omega}^a = \frac{d\gamma}{dt}\overrightarrow{a_1} = \overset{\bullet}{\gamma}\overrightarrow{a_1} \tag{2.4}$$

where γ is the rolling angle, and the $\bullet$ represents the derivative with respect to time.

The orientation of System b in System a can be described by a 2-1-3 set of Euler

16

angles θ_2, θ_1, and θ_3:

$$\left\{ \begin{array}{c} \overrightarrow{b_1} \\ \overrightarrow{b_2} \\ \overrightarrow{b_3} \end{array} \right\} = \left[\begin{array}{ccc} c_2c_3 + s_1s_2s_3 & c_1s_3 & -c_3s_2 + c_2s_1s_3 \\ c_3s_1s_2 - c_2s_3 & c_1c_3 & c_2c_3s_1 + s_2s_3 \\ c_1s_2 & -s_1 & c_1c_2 \end{array} \right] \left\{ \begin{array}{c} \overrightarrow{a_1} \\ \overrightarrow{a_2} \\ \overrightarrow{a_3} \end{array} \right\} \tag{2.5}$$

with c_i and s_i defined as

$$c_i = \cos\theta_i, \; s_i = \sin\theta_i \qquad (i = 1, \; 2, \; 3)$$

The Euler angles θ_1 and θ_3 essentially are the partial derivatives of the bending deflections:

$$\theta_1 = \frac{\partial u_3}{\partial y}, \quad \theta_3 = -\frac{\partial u_1}{\partial y} \tag{2.6}$$

while θ_2 is the twist angle.

The previous definitions of θ_1, θ_2, and θ_3 lead to the following expression for the angular velocity of System b with respect to System a.

$$^a\underline{\omega}^b = \left(c_3\dot{\theta}_1 + c_1s_3\dot{\theta}_2 \right) \overrightarrow{b_1} + \left(-s_3\dot{\theta}_1 + c_1c_3\dot{\theta}_2 \right) \overrightarrow{b_2} + \left(-s_1\dot{\theta}_2 + \dot{\theta}_3 \right) \overrightarrow{b_3} \tag{2.7}$$

The angular velocity of System b with respect to System n, found by using the angular velocity addition theorem, is thus given by

$$\begin{aligned} ^n\underline{\omega}^b &= \; ^a\underline{\omega}^b + \; ^n\underline{\omega}^a \tag{2.8} \\ &= \left(c_2c_3\dot{\gamma} + s_1s_2s_3\dot{\gamma} + c_3\dot{\theta}_1 + c_1s_3\dot{\theta}_2 \right) \overrightarrow{b_1} + \left(c_3s_1s_2\dot{\gamma} - c_2s_3\dot{\gamma} - s_3\dot{\theta}_1 + c_1c_3\dot{\theta}_2 \right) \overrightarrow{b_2} \\ &\quad + \left(c_1s_2\dot{\gamma} - s_1\dot{\theta}_2 + \dot{\theta}_3 \right) \overrightarrow{b_3} \end{aligned}$$

With the assumption that the elastic deformations are small and the rolling angle γ

is small too for the time being, the velocity of the centroid C then can be found as

$$
\begin{aligned}
{}^n\underline{v}^C &= \frac{d}{dt}\left(\overrightarrow{OC}\right) \\
&= \frac{d}{dt}\left(\overrightarrow{OF} + \overrightarrow{FB} + \overrightarrow{BC}\right) \\
&= \left(\dot{u}_1\overrightarrow{a_1} + \dot{u}_2\overrightarrow{a_2} + \dot{u}_3\overrightarrow{a_3}\right) + {}^n\underline{\omega}^a \times \left(y\overrightarrow{a_2} + u_1\overrightarrow{a_1} + u_2\overrightarrow{a_2} + u_3\overrightarrow{a_3}\right) \\
&\quad + {}^n\underline{\omega}^b \times \left(r_x\overrightarrow{b_1} + r_z\overrightarrow{b_3}\right) \\
&= \left(\dot{u}_1 + r_z\dot{\theta}_2\right)\overrightarrow{a_1} + \left(-r_z\dot{\gamma} + \dot{u}_2 - r_z\dot{\theta}_1 + r_x\dot{\theta}_3\right)\overrightarrow{a_2} + \left(y\dot{\gamma} + \dot{u}_3 - r_x\dot{\theta}_2\right)\overrightarrow{a_3}
\end{aligned}
\tag{2.9}
$$

Neglecting the rotatory kinetic energy along the $\overrightarrow{b_1}$ and $\overrightarrow{b_3}$ axes leads to the following expression for the kinetic energy of the system:

$$
T = \frac{1}{2}\int_{-L}^{L}\left[\rho A\left({}^n\underline{v}^C \cdot {}^n\underline{v}^C\right) + I_{22}\dot{\theta}_2^2\right]dy + \frac{1}{2}I_F\dot{\gamma}^2
\tag{2.10}
$$

where ρA is the mass per unit length of the beam, I_{22} is the mass moment of inertia about the $\overrightarrow{b_2}$-axis per unit length of the beam, and I_F is the mass moment of inertia about the $\overrightarrow{a_1}$-axis of the fuselage.

The potential energy contributed by the elastic bending, torsion and extension can be expressed as:

$$
V = \frac{1}{2}\int_{-L}^{L}\left[EA\left(\frac{\partial u_2}{\partial y}\right)^2 + EI_{xx}\left(\frac{\partial^2 u_3}{\partial y^2}\right)^2 + EI_{zz}\left(\frac{\partial^2 u_1}{\partial y^2}\right)^2 + GJ\left(\frac{\partial \theta_2}{\partial y}\right)^2\right]dy
\tag{2.11}
$$

where EA, EI_{xx}, EI_{zz}, GJ are the extensional rigidity, the flexural rigidity about the $\overrightarrow{b_1}$-axis, the flexural rigidity about the $\overrightarrow{b_3}$-axis, and the torsional rigidity, respectively.

With the kinetic and potential energies of the system identified, we use the extended Hamilton's principle

$$
\int_{t_1}^{t_2}\left(\delta T - \delta V + \delta W_{NC}\right)dt = 0
\tag{2.12}
$$

18

where δW_{NC} is the virtual work done by the nonconservative forces. We neglect the effects of the extension on the bending and the twist. Finally we obtain the following equations of motion $\left(\text{by using } \mathbf{Mathematica}^{\circledR} \right)$:

$$I_F \ddot{\gamma} + \int_{-L}^{L} \rho A \left(y^2 \ddot{\gamma} + y \ddot{u}_3 - r_x y \ddot{\theta}_2 \right) dy = M_{rolling}$$

$$(EI_{zz} u_1'')'' + \rho A \ddot{u}_1 + \rho A r_z \ddot{\theta}_2 = f_{u_1}$$

$$- (EA u_2')' + \rho A \ddot{u}_2 = f_{u_2} \tag{2.13}$$

$$(EI_{xx} u_3'')'' + \rho A \ddot{u}_3 + \rho A y \ddot{\gamma} - \rho A r_x \ddot{\theta}_2 = f_{u_3}$$

$$- (GJ \theta_2')' + I_{22} \ddot{\theta}_2 + \rho A r_z \ddot{u}_1 - \rho A r_x \ddot{u}_3 - \rho A r_x y \ddot{\gamma} = m_{\theta_2}$$

where the $'$ represents the derivative with respect to y, $M_{rolling}$ is the total rolling moment about $\overrightarrow{a_1}$ axis, and f_{u_1}, f_{u_2}, f_{u_3}, and m_{θ_2} are the corresponding forces or moment per unit length, respectively.

Comparing to the case of elastic deformation only, we have introduced an extra variable γ, the rolling angle. We have to apply constraints to make the problem well-defined. Here, it is natural to choose the following:

$$u_1 = u_2 = u_3 = u_1' = u_3' = \theta_2 = 0 \quad \text{at } y = 0 \tag{2.14}$$

At free ends, $y = -L$ and $y = L$, we have the natural boundary conditions (B.C.):

$$u_1'' = u_1''' = u_2' = u_3'' = u_3''' = \theta_2' = 0 \tag{2.15}$$

When there is no rolling motion (the case when the semi-span wing is mounted to the wall of the wind tunnel), the equations reduce to the governing equations for the typical

cantilever beam with inertial coupling between torsion and bending:

$$
\begin{aligned}
(EI_{zz}u_1'')'' + \rho A\ddot{u}_1 + \rho A r_z\ddot{\theta}_2 &= f_{u_1} \\
-(EAu_2')' + \rho A\ddot{u}_2 &= f_{u_2} \\
(EI_{xx}u_3'')'' + \rho A\ddot{u}_3 - \rho A r_x\ddot{\theta}_2 &= f_{u_3} \\
-(GJ\theta_2')' + I_{22}\ddot{\theta}_2 + \rho A r_z\ddot{u}_1 - \rho A r_x\ddot{u}_3 &= m_{\theta_2}
\end{aligned}
\tag{2.16}
$$

with geometric or essential boundary conditions:

$$
u_1 = u_2 = u_3 = u_1' = u_3' = \theta_2 = 0 \qquad \text{at } y = 0
\tag{2.17}
$$

and natural boundary conditions:

$$
u_1'' = u_1''' = u_2' = u_3'' = u_3''' = \theta_2' = 0 \quad \text{at } y = L
\tag{2.18}
$$

Equation (2.16) is same as the one developed in Rao (1992), where a less rigorous approach is used.

2.2 Finite-Element Discretization

In the section above, we have developed the equations governing the wing's motion, which are hybrid ordinary-partial-differential and integral equations. In practice we usually need to transform partial differential equations (PDE) into ordinary differential equations (ODE) by discretizing in the space coordinates.

We choose the finite-element method to discretize the equations. The reason behind this choice is that, generally, wing structures are so complicated that finite-element methods are used almost exclusively to develop the governing equations. Moreover, the finite-element method is fully compatible with the aerodynamic model which is introduced in the next chapter, and so it is easy for the two models to communicate.

2.2.1 Galerkin Formulation of the Problem

To transform PDE's to ODE's, we use a generalized Galerkin approach to formulize the governing equations in integral forms. First of all, we consider the equation for the bending deflection u_3 in Equations (2.13). We set test function $\phi : [-L, \, L] \to R$ be a smooth function such that $\phi(0) = 0$, and $\frac{\partial \phi(0)}{\partial y} = 0$. Multiplying both sides of equations by ϕ and integrating the resulting equations over the domain $(-L, \, L)$, we obtain

$$\int_{-L}^{L} \phi \left[(EI_{xx} u_3'')'' + \rho A \ddot{u}_3 + \rho A y \ddot{\gamma} - \rho A r_x \ddot{\theta}_2 \right] dy = \int_{-L}^{L} \phi f_{u_3} dy$$

$$\phi \frac{\partial}{\partial y}(EI_{xx}\frac{\partial^2 u_3}{\partial y^2})|_{-L}^{L} - \int_{-L}^{L} \frac{\partial \phi}{\partial y}\frac{\partial}{\partial y}[EI_{xx}\frac{\partial^2 u_3}{\partial y^2}]dy + \int_{-L}^{L} \rho A \phi \frac{\partial^2 u_3}{\partial t^2}dy + \int_{-L}^{L} \rho A y \phi \frac{\partial^2 \gamma}{\partial t^2}dy$$
$$- \int_{-L}^{L} \rho A r_x \phi \frac{\partial^2 \theta_2}{\partial t^2}dy = \int_{-L}^{L} \phi f_{u_3} dy$$

$$- \frac{\partial \phi}{\partial y}EI_{xx}\frac{\partial^2 u_3}{\partial y^2}|_{-L}^{L} + \int_{-L}^{L} EI_{xx}\frac{\partial^2 \phi}{\partial y^2}\frac{\partial^2 u_3}{\partial y^2}dy + \int_{-L}^{L} \rho A \phi \frac{\partial^2 u_3}{\partial t^2}dy + \int_{-L}^{L} \rho A y \phi \frac{\partial^2 \gamma}{\partial t^2}dy$$
$$- \int_{-L}^{L} \rho A r_x \phi \frac{\partial^2 \theta_2}{\partial t^2}dy = \int_{-L}^{L} \phi f_{u_3} dy$$

$$\int_{-L}^{L} EI_{xx}\frac{\partial^2 \phi}{\partial y^2}\frac{\partial^2 u_3}{\partial y^2}dy + \int_{-L}^{L} \rho A \phi \frac{\partial^2 u_3}{\partial t^2}dy + \frac{\partial^2 \gamma}{\partial t^2}\int_{-L}^{L} \rho A y \phi dy - \int_{-L}^{L} \rho A r_x \phi \frac{\partial^2 \theta_2}{\partial t^2}dy = \int_{-L}^{L} \phi f_{u_3} dy$$

$$(2.19)$$

Here we have integrated twice by parts to obtain the same-order derivatives with respect to y on ϕ and u_3, and have substituted for the natural boundary conditions prescribed at the ends $y = -L$ and $y = L$.

Similarly,

$$\int\limits_{-L}^{L} EI_{zz}\frac{\partial^2 \phi}{\partial y^2}\frac{\partial^2 u_1}{\partial y^2}dy + \int\limits_{-L}^{L} \rho A\phi\frac{\partial^2 u_1}{\partial t^2}dy + \int\limits_{-L}^{L} \rho A r_z\phi\frac{\partial^2 \theta_2}{\partial t^2}dy = \int\limits_{-L}^{L} \phi f_{u_1}dy \qquad (2.20)$$

We assume that $\psi : [-L,\, L] \rightarrow R$ is another test function such that $\psi(0) = 0$. Multiplying both sides of the equation about θ_2 in Equations (2.13) by ψ and then integrating over the domain $(-L,\, L)$ yields

$$-\int\limits_{-L}^{L} \psi\frac{\partial}{\partial y}[GJ\frac{\partial\theta_2}{\partial y}]dy + \int\limits_{-L}^{L} \psi I_{22}\frac{\partial^2\theta_2}{\partial t^2}dy + \int\limits_{-L}^{L} \rho A\psi(r_z\ddot{u}_1 - r_x\ddot{u}_3 - r_x y\ddot{\gamma})dy = \int\limits_{-L}^{L} \psi m_{\theta_2}dy$$

$$-\psi GJ\frac{\partial\theta_2}{\partial y}|_{-L}^{L} + \int\limits_{-L}^{L} GJ\frac{\partial\psi}{\partial y}\frac{\partial\theta_2}{\partial y}dy + \int\limits_{-L}^{L} \psi I_{22}\frac{\partial^2\theta_2}{\partial t^2}dy + \int\limits_{-L}^{L} \rho A\psi(r_z\frac{\partial^2 u_1}{\partial t^2} - r_x\frac{\partial^2 u_3}{\partial t^2} - r_x y\frac{\partial^2\gamma}{\partial t^2})dy$$

$$= \int\limits_{-L}^{L} \psi m_{\theta_2}dy$$

With the application of boundary conditions, the above equation becomes

$$\int\limits_{-L}^{L} GJ\frac{\partial\psi}{\partial y}\frac{\partial\theta_2}{\partial y}dy + \int\limits_{-L}^{L} \psi I_{22}\frac{\partial^2\theta_2}{\partial t^2}dy + \int\limits_{-L}^{L} \rho A\psi(r_z\frac{\partial^2 u_1}{\partial t^2} - r_x\frac{\partial^2 u_3}{\partial t^2} - r_x y\frac{\partial^2\gamma}{\partial t^2})dy = \int\limits_{-L}^{L} \psi m_{\theta_2}dy$$

$$(2.21)$$

Similarly, for the equation governing extension u_2, we have

$$\int\limits_{-L}^{L} EA\frac{\partial\psi}{\partial y}\frac{\partial u_2}{\partial y}dy + \int\limits_{-L}^{L} \psi\rho A\frac{\partial^2 u_2}{\partial t^2}dy = \int\limits_{-L}^{L} \psi f_{u_2}dy \qquad (2.22)$$

The weak formation of the problem defined by Equations (2.13) and B.C.'s can be stated as follows:

Find u_1, u_2, u_3, θ_2 such that equations (2.19), (2.20), (2.21) and (2.22) hold

for every ϕ, ψ.

The natural boundary conditions are embedded into the weak formulation of the problem and the essential boundary conditions are to be explicitly satisfied.

2.2.2 Finite Element Formation

The finite element method comes into the picture when choosing the basis functions. The first step is to divide the beam into a finite number of elements. The end points of each element are called nodes. The collection of finite elements and nodes is called a finite element mesh. The basis functions chosen in the finite element method are generated by simple functions defined piecewise—element by element—over the finite element mesh. The applications of basis functions to an element are called shape functions.

The governing equations about deflections u_1 and u_3 are fourth-order differential equations with respect to the space coordinate y. A typical basis function choice is the Hermitian basis functions. We let Φ_1^0, Φ_1^1, Φ_2^0, Φ_2^1, $\cdots$, Φ_n^0, Φ_n^1 be the Hermitian basis functions for test function ϕ, and the deflections u_1, u_3. The corresponding Hermitian shape function in an element with nodes y_i, y_j are denoted as N_i^0, N_i^1, N_j^0, N_j^1. The plots of them are shown in Figure 2-2. In terms of the local coordinate

$$s = \frac{2y - (y_i + y_j)}{h_e} \tag{2.23}$$

where $h_e = y_j - y_i$, is the element length, the shape functions are given by

$$
\begin{aligned}
N_i^0 &= \tfrac{1}{4}\left(2 - 3s + s^3\right) \\
N_i^1 &= \tfrac{h_e}{8}\left(1 - s - s^2 + s^3\right) \\
N_j^0 &= \tfrac{1}{4}\left(2 + 3s - s^3\right) \\
N_j^1 &= \tfrac{h_e}{8}\left(-1 - s + s^2 + s^3\right)
\end{aligned}
\tag{2.24}
$$

23

With Hermitian basis functions, we express that

$$\phi = \sum_{i=1}^{n} [C_i^0 \Phi_i^0(y) + C_i^1 \Phi_i^1(y)]$$

$$u_1 = \sum_{i=1}^{n} [u_{1i} \Phi_i^0(y) + u_{1i}' \Phi_i^1(y)] \qquad (2.25)$$

$$u_3 = \sum_{i=1}^{n} [u_{3i} \Phi_i^0(y) + u_{3i}' \Phi_i^1(y)]$$

where u_{1i}, u_{3i} $(i = 1, \cdots n)$ are the nodal displacements of u_1 and u_3 respectively, u_{1i}' and u_{3i}' $(i = 1, \cdots n)$ are the the first order derivatives with respect to the y coordinate, and n is the total number of finite element nodes.

We let Ψ_1, Ψ_2, $\cdots$, Ψ_n be the linear Lagrangian basis functions for ψ, θ_2, and u_2. The corresponding shape functions are denoted as N_i, N_j. They are also shown in Figure 2-2. Their expressions in terms of the above defined local coordinate are as the follows:

$$N_i = \tfrac{1}{2}(1 - s)$$

$$N_j = \tfrac{1}{2}(1 + s) \qquad (2.26)$$

Then

$$\psi = \sum_{i=1}^{n} D_i \Psi_i(y)$$

$$u_2 = \sum_{i=1}^{n} u_{2i} \Psi_i(y) \qquad (2.27)$$

$$\theta_2 = \sum_{i=1}^{n} \theta_{2i}(t) \Psi_i(y)$$

where u_{2i}, θ_{2i} $(i = 1, \cdots n)$ are the nodes' u_2 displacement, θ_2 twist, respectively.

The finite element basis functions constructed with the shape functions are plotted in Figure 2-3.

By denoting the following in matrix notation,

$$
\{U_1\} = \left\{ \begin{array}{c} u_{11} \\ u'_{11} \\ u_{12} \\ u'_{12} \\ \vdots \\ u_{1n} \\ u'_{1n} \end{array} \right\}, \{U_2\} = \left\{ \begin{array}{c} u_{21} \\ u_{22} \\ \vdots \\ u_{2n} \end{array} \right\}, \{U_3\} = \left\{ \begin{array}{c} u_{31} \\ u'_{31} \\ u_{32} \\ u'_{32} \\ \vdots \\ u_{3n} \\ u'_{3n} \end{array} \right\}, \{\Theta_2\} = \left\{ \begin{array}{c} \theta_{21} \\ \theta_{22} \\ \vdots \\ \theta_{2n} \end{array} \right\} \qquad (2.28)
$$

we have

$$
\phi = \left(\begin{array}{cccccc} \Phi_1^0 & \Phi_1^1 & \Phi_2^0 & \Phi_2^1 & \cdots & \Phi_n^0 & \Phi_n^1 \end{array} \right) \left\{ \begin{array}{c} C_1^0 \\ C_1^1 \\ C_2^0 \\ C_2^1 \\ \vdots \\ C_n^0 \\ C_n^1 \end{array} \right\} \qquad (2.29)
$$

$$
u_1 = \left(\begin{array}{cccccc} \Phi_1^0 & \Phi_1^1 & \Phi_2^0 & \Phi_2^1 & \cdots & \Phi_n^0 & \Phi_n^1 \end{array} \right) \{U_1\} \qquad (2.30)
$$

$$
u_3 = \left(\begin{array}{cccccc} \Phi_1^0 & \Phi_1^1 & \Phi_2^0 & \Phi_2^1 & \cdots & \Phi_n^0 & \Phi_n^1 \end{array} \right) \{U_3\} \qquad (2.31)
$$

$$
\psi = \left(\begin{array}{cccc} \Psi_1 & \Psi_2 & \cdots & \Psi_n \end{array} \right) \left\{ \begin{array}{c} D_1 \\ D_2 \\ \vdots \\ D_n \end{array} \right\} \qquad (2.32)
$$

$$
u_2 = \left(\begin{array}{cccc} \Psi_1 & \Psi_2 & \cdots & \Psi_n \end{array} \right) \{U_2\} \qquad (2.33)
$$

$$
\theta = \left(\begin{array}{cccc} \Psi_1 & \Psi_2 & \cdots & \Psi_n \end{array} \right) \{\Theta_2\} \qquad (2.34)
$$

Substituting the above expressions into Equation (2.19) and expressing the result in matrix form, we have

$$
\begin{pmatrix} C_1^0 & C_1^1 & C_2^0 & C_2^1 & \cdots & C_n^0 & C_n^1 \end{pmatrix} ([K_{u_3}]_{2n \times 2n} \{U_3\} + [M_{u_3}]_{2n \times 2n} \{\ddot{U}_3\}
$$
$$
+ \{Q_{u_3}^\gamma\} \ddot{\gamma} + [M_{u_3}^{\theta_2}]_{2n \times n} \{\ddot{\Theta}_2\}) = \begin{pmatrix} C_1^0 & C_1^1 & C_2^0 & C_2^1 & \cdots & C_n^0 & C_n^1 \end{pmatrix} \{F_3\} \quad (2.35)
$$

where

$$
[M_{u_3}]_{2n \times 2n} = \int_{-L}^{L} \rho A \begin{Bmatrix} \Phi_1^0 \\ \Phi_1^1 \\ \Phi_2^0 \\ \Phi_2^1 \\ \vdots \\ \Phi_n^0 \\ \Phi_n^1 \end{Bmatrix} \begin{pmatrix} \Phi_1^0 & \Phi_1^1 & \Phi_2^0 & \Phi_2^1 & \cdots & \Phi_n^0 & \Phi_n^1 \end{pmatrix} dy \quad (2.36)
$$

$$
[M_{u_3}^{\theta_2}]_{2n \times n} = -\int_{-L}^{L} r_x \rho A \begin{Bmatrix} \Phi_1^0 \\ \Phi_1^1 \\ \Phi_2^0 \\ \Phi_2^1 \\ \vdots \\ \Phi_n^0 \\ \Phi_n^1 \end{Bmatrix} \begin{pmatrix} \Psi_1 & \Psi_2 & \cdots & \Psi_n \end{pmatrix} dy \quad (2.37)
$$

$$[K_{u_3}]_{2n \times 2n} = \int\limits_{-L}^{L} EI_{xx} \left\{ \begin{array}{c} \frac{\partial^2 \Phi_1^0}{\partial y^2} \\ \frac{\partial^2 \Phi_1^1}{\partial y^2} \\ \frac{\partial^2 \Phi_2^0}{\partial y^2} \\ \frac{\partial^2 \Phi_2^1}{\partial y^2} \\ \vdots \\ \frac{\partial^2 \Phi_n^0}{\partial y^2} \\ \frac{\partial^2 \Phi_n^1}{\partial y^2} \end{array} \right\} \left(\begin{array}{ccccccc} \frac{\partial^2 \Phi_1^0}{\partial y^2} & \frac{\partial^2 \Phi_1^1}{\partial y^2} & \frac{\partial^2 \Phi_2^0}{\partial y^2} & \frac{\partial^2 \Phi_2^1}{\partial y^2} & \cdots & \frac{\partial^2 \Phi_n^0}{\partial y^2} & \frac{\partial^2 \Phi_n^1}{\partial y^2} \end{array} \right) dy$$

$$(2.38)$$

$$\{Q_{u_3}^\gamma\} = \int\limits_{-L}^{L} \rho A y \left\{ \begin{array}{c} \Phi_1^0 \\ \Phi_1^1 \\ \Phi_2^0 \\ \Phi_2^1 \\ \vdots \\ \Phi_n^0 \\ \Phi_n^1 \end{array} \right\} dy \qquad (2.39)$$

$$\{F_3\} = \int\limits_{-L}^{L} f_{u_3} \left\{ \begin{array}{c} \Phi_1^0 \\ \Phi_1^1 \\ \Phi_2^0 \\ \Phi_2^1 \\ \vdots \\ \Phi_n^0 \\ \Phi_n^1 \end{array} \right\} dy \qquad (2.40)$$

Different choices of C_i^0 and C_i^1 will yield different functions ϕ in Equation (2.35), but this equation should hold for all choices of constants C_1^0, C_1^1, $\cdots$, C_n^1. Eventually we get

$$[M_{u_3}] \left\{ \ddot{U}_3 \right\} + [M_{u_3}^{\theta_2}] \left\{ \ddot{\Theta}_2 \right\} + \{Q_{u_3}^\gamma\} \ddot{\gamma} + [K_{u_3}] \{U_3\} = \{F_3\} \qquad (2.41)$$

Similarly,

$$[M_{u_1}] \left\{ \ddot{U}_1 \right\} + [M_{u_1}^{\theta_2}]_{2n \times n} \left\{ \ddot{\Theta}_2 \right\} + [K_{u_1}] \{U_1\} = \{F_1\} \qquad (2.42)$$

$$[M_{u_2}] \left\{ \ddot{U}_2 \right\} + [K_{u_2}] \left\{ U_2 \right\} = \{F_2\} \tag{2.43}$$

$$[M_{\theta_2}] \left\{ \ddot{\Theta}_2 \right\} + \left[M_{\theta_2}^{u_1} \right] \left\{ \ddot{U}_1 \right\} + \left[M_{\theta_2}^{u_3} \right] \left\{ \ddot{U}_3 \right\} + [K_{\theta_2}] \{\Theta\} + \left\{ Q_{\theta_2}^\gamma \right\} \ddot{\gamma} = \{F_{\theta_2}\} \tag{2.44}$$

where, with the superscript T denoting the transpose of matrixes,

$$[M_{u_3}] = [M_{u_1}] \tag{2.45}$$

$$\left[M_{u_1}^{\theta_2} \right] = \int_{-L}^{L} r_z \rho A \left\{ \begin{array}{c} \Phi_1^0 \\ \Phi_1^1 \\ \Phi_2^0 \\ \Phi_2^1 \\ \vdots \\ \Phi_n^0 \\ \Phi_n^1 \end{array} \right\} \left(\begin{array}{cccc} \Psi_1 & \Psi_2 & \cdots & \Psi_n \end{array} \right) dy \tag{2.46}$$

$$[M_{u_2}] = \int_{-L}^{L} \rho A \left\{ \begin{array}{c} \Psi_1 \\ \Psi_2 \\ \vdots \\ \Psi_n \end{array} \right\} \left(\begin{array}{cccc} \Psi_1 & \Psi_2 & \cdots & \Psi_n \end{array} \right) dy \tag{2.47}$$

$$[M_{\theta_2}] = \int_{-L}^{L} I_{22} \left\{ \begin{array}{c} \Psi_1 \\ \Psi_2 \\ \vdots \\ \Psi_n \end{array} \right\} \left(\begin{array}{cccc} \Psi_1 & \Psi_2 & \cdots & \Psi_n \end{array} \right) dy \tag{2.48}$$

$$\left[M_{\theta_2}^{u_1} \right] = \left[M_{u_1}^{\theta_2} \right]^T \tag{2.49}$$

$$\left[M_{\theta_2}^{u_3} \right] = \left[M_{u_3}^{\theta_2} \right]^T \tag{2.50}$$

28

$$[K_{u_1}] = \int\limits_{-L}^{L} EI_{zz} \left\{ \begin{array}{c} \frac{\partial^2 \Phi_1^0}{\partial y^2} \\ \frac{\partial^2 \Phi_1^1}{\partial y^2} \\ \frac{\partial^2 \Phi_2^0}{\partial y^2} \\ \frac{\partial^2 \Phi_2^1}{\partial y^2} \\ \vdots \\ \frac{\partial^2 \Phi_n^0}{\partial y^2} \\ \frac{\partial^2 \Phi_n^1}{\partial y^2} \end{array} \right\} \left(\begin{array}{cccccccc} \frac{\partial^2 \Phi_1^0}{\partial y^2} & \frac{\partial^2 \Phi_1^1}{\partial y^2} & \frac{\partial^2 \Phi_2^0}{\partial y^2} & \frac{\partial^2 \Phi_2^1}{\partial y^2} & \ldots & \frac{\partial^2 \Phi_n^0}{\partial y^2} & \frac{\partial^2 \Phi_n^1}{\partial y^2} \end{array} \right) dy \qquad (2.51)$$

$$[K_{u_2}] = \int\limits_{-L}^{L} EA \left\{ \begin{array}{c} \frac{\partial \Psi_1}{\partial y} \\ \frac{\partial \Psi_2}{\partial y} \\ \vdots \\ \frac{\partial \Psi_n}{\partial y} \end{array} \right\} \left(\begin{array}{cccc} \frac{\partial \Psi_1}{\partial y} & \frac{\partial \Psi_2}{\partial y} & \ldots & \frac{\partial \Psi_n}{\partial y} \end{array} \right) dy \qquad (2.52)$$

$$[K_{\theta}] = \int\limits_{-L}^{L} GJ \left\{ \begin{array}{c} \frac{\partial \Psi_1}{\partial y} \\ \frac{\partial \Psi_2}{\partial y} \\ \vdots \\ \frac{\partial \Psi_n}{\partial y} \end{array} \right\} \left(\begin{array}{cccc} \frac{\partial \Psi_1}{\partial y} & \frac{\partial \Psi_2}{\partial y} & \ldots & \frac{\partial \Psi_n}{\partial y} \end{array} \right) dy \qquad (2.53)$$

$$\{Q_{\theta_2}^{\gamma}\} = - \int\limits_{-L}^{L} \rho A r_x y \left\{ \begin{array}{c} \Psi_1 \\ \Psi_2 \\ \vdots \\ \Psi_n \end{array} \right\} dy \qquad (2.54)$$

$$\{F_1\} = \int\limits_{-L}^{L} f_{u_1} \left\{ \begin{array}{c} \Phi_1^0 \\ \Phi_1^1 \\ \Phi_2^0 \\ \Phi_2^1 \\ \vdots \\ \Phi_n^0 \\ \Phi_n^1 \end{array} \right\} dy \qquad (2.55)$$

$$\{F_2\} = \int_{-L}^{L} f_{u_2} \left\{ \begin{array}{c} \Psi_1 \\ \Psi_2 \\ \vdots \\ \Psi_n \end{array} \right\} dy \tag{2.56}$$

$$\{F_{\theta_2}\} = \int_{-L}^{L} m_{\theta_2} \left\{ \begin{array}{c} \Psi_1 \\ \Psi_2 \\ \vdots \\ \Psi_n \end{array} \right\} dy \tag{2.57}$$

Combining the four equations (2.41), (2.42), (2.43) and (2.44), we get

$$[M_E] \left\{ \begin{array}{c} \ddot{U}_1 \\ \ddot{U}_2 \\ \ddot{U}_3 \\ \ddot{\Theta}_2 \end{array} \right\} + [K_E] \left\{ \begin{array}{c} U_1 \\ U_2 \\ U_3 \\ \Theta \end{array} \right\} + \ddot{\gamma} \{Q_\gamma\} = \left\{ \begin{array}{c} F_1 \\ F_2 \\ F_3 \\ F_{\theta_2} \end{array} \right\} \tag{2.58}$$

where

$$[M_E] = \begin{bmatrix} M_{u_1} & 0 & 0 & M_{u_1}^{\theta_2} \\ 0 & M_{u_2} & 0 & 0 \\ 0 & 0 & M_{u_3} & M_{u_3}^{\theta_2} \\ M_{\theta_2}^{u_1} & 0 & M_{\theta_2}^{u_3} & M_{\theta_2} \end{bmatrix}, [K_E] = \begin{bmatrix} K_{u_1} & 0 & 0 & 0 \\ 0 & K_{u_2} & 0 & 0 \\ 0 & 0 & K_{u_3} & 0 \\ 0 & 0 & 0 & K_{\theta_2} \end{bmatrix}, \{Q_\gamma\} = \left\{ \begin{array}{c} 0 \\ 0 \\ Q_{u_3}^\gamma \\ Q_{\theta_2}^\gamma \end{array} \right\} \tag{2.59}$$

When there is no rolling motion ($\gamma = 0$), i.e., the beam is considered to be a cantilever beam, and Equation (2.58) becomes

$$[M_E] \left\{ \begin{array}{c} \ddot{U}_1 \\ \ddot{U}_2 \\ \ddot{U}_3 \\ \ddot{\Theta}_2 \end{array} \right\} + [K_E] \left\{ \begin{array}{c} \ddot{U}_1 \\ \ddot{U}_2 \\ \ddot{U}_3 \\ \ddot{\Theta}_2 \end{array} \right\} = \left\{ \begin{array}{c} F_1 \\ F_2 \\ F_3 \\ F_{\theta_2} \end{array} \right\} \tag{2.60}$$

The equation for rigid-body rolling motion γ becomes

$$I_F\ddot{\gamma} + \ddot{\gamma}\int_{-L}^{L}\rho A y^2 dy + \int_{-L}^{L}\rho A y \left(\begin{array}{cccccccc} \Phi_1^0 & \Phi_1^1 & \Phi_2^0 & \Phi_2^1 & \cdots & \Phi_n^0 & \Phi_n^1 \end{array} \right) \left\{ \begin{array}{c} \ddot{u}_{31} \\ \ddot{u}'_{31} \\ \ddot{u}_{32} \\ \ddot{u}'_{32} \\ \vdots \\ \ddot{u}_{3n} \\ \ddot{u}'_{3n} \end{array} \right\} dy$$

$$- \int_{-L}^{L}\rho A r_x y \left(\begin{array}{cccc} \Psi_1 & \Psi_2 & \cdots & \Psi_n \end{array} \right) \left\{ \begin{array}{c} \ddot{\theta}_1 \\ \ddot{\theta}_2 \\ \vdots \\ \ddot{\theta}_n \end{array} \right\} dy = M_{rolling}$$

$$(I_F + \frac{2}{3}\rho A L^3)\ddot{\gamma} + [Q_\gamma^{u3}]\{\ddot{U}_3\} + [Q_\gamma^{\theta_2}]\{\ddot{\Theta}_2\} = M_{rolling} \qquad (2.61)$$

where

$$[Q_\gamma^{u3}] = \int_{-L}^{L}\rho A y \left(\begin{array}{cccccccc} \Phi_1^0 & \Phi_1^1 & \Phi_2^0 & \Phi_2^1 & \cdots & \Phi_n^0 & \Phi_n^1 \end{array} \right) dy = \left\{ Q_{u_3}^\gamma \right\}^T \qquad (2.62)$$

$$[Q_\gamma^{\theta_2}] = - \int_{-L}^{L}\rho A r_x y \left(\begin{array}{cccc} \Psi_1 & \Psi_2 & \cdots & \Psi_n \end{array} \right) dy = \left\{ Q_{\theta_2}^\gamma \right\}^T \qquad (2.63)$$

Combining all the elastic-deformation and rigid-body-motion equations, we have

$$
\begin{bmatrix}
(I_F + \frac{2}{3}\rho A L^3) & 0 & 0 & Q_\gamma^{u_3} & Q_\gamma^{\theta_2} \\
0 & M_{u_1} & 0 & 0 & M_{u_1}^{\theta_2} \\
0 & 0 & M_{u_2} & 0 & 0 \\
Q_{u_3}^\gamma & 0 & 0 & M_{u_3} & M_{u_3}^{\theta_2} \\
Q_{\theta_2}^\gamma & M_{\theta_2}^{u_1} & 0 & M_{\theta_2}^{u_3} & M_{\theta_2}
\end{bmatrix}
\begin{Bmatrix}
\ddot{\gamma} \\
\ddot{U}_1 \\
\ddot{U}_2 \\
\ddot{U}_3 \\
\ddot{\Theta}_2
\end{Bmatrix}
$$

$$
+
\begin{bmatrix}
0 & 0 & 0 & 0 & 0 \\
0 & K_{u_1} & 0 & 0 & 0 \\
0 & 0 & K_{u_2} & 0 & 0 \\
0 & 0 & 0 & K_{u_3} & 0 \\
0 & 0 & 0 & 0 & K_{\theta_2}
\end{bmatrix}
\begin{Bmatrix}
\gamma \\
U_1 \\
U_2 \\
U_3 \\
\Theta_2
\end{Bmatrix}
=
\begin{Bmatrix}
M_{rolling} \\
F_1 \\
F_2 \\
F_3 \\
F_{\theta_2}
\end{Bmatrix}
\qquad (2.64)
$$

By denoting that

$$
[M_t] =
\begin{bmatrix}
(I_F + \frac{2}{3}\rho A L^3) & 0 & 0 & Q_\gamma^{u_3} & Q_\gamma^{\theta_2} \\
0 & M_{u_1} & 0 & 0 & M_{u_1}^{\theta_2} \\
0 & 0 & M_{u_2} & 0 & 0 \\
Q_{u_3}^\gamma & 0 & 0 & M_{u_3} & M_{u_3}^{\theta_2} \\
Q_{\theta_2}^\gamma & M_{\theta_2}^{u_1} & 0 & M_{\theta_2}^{u_3} & M_{\theta_2}
\end{bmatrix}
, \;
[K_t] =
\begin{bmatrix}
0 & 0 & 0 & 0 & 0 \\
0 & K_{u_1} & 0 & 0 & 0 \\
0 & 0 & K_{u_2} & 0 & 0 \\
0 & 0 & 0 & K_{u_3} & 0 \\
0 & 0 & 0 & 0 & K_{\theta_2}
\end{bmatrix}
$$
$$(2.65)$$

Equation (2.64) becomes

$$
[M_t]
\begin{Bmatrix}
\ddot{\gamma} \\
\ddot{U}_1 \\
\ddot{U}_2 \\
\ddot{U}_3 \\
\ddot{\Theta}
\end{Bmatrix}
+ [K_t]
\begin{Bmatrix}
\gamma \\
U_1 \\
U_2 \\
U_3 \\
\Theta
\end{Bmatrix}
=
\begin{Bmatrix}
M_{rolling} \\
F_1 \\
F_2 \\
F_3 \\
F_{\theta_2}
\end{Bmatrix}
\qquad (2.66)
$$

It is clear that $[M_t]$ is symmetric and positive definite, $[K_t]$ is also symmetric but semi-positive definite, because obviously the determinant of $[K_t]$ is zero. Also evident is

the fact that there is the inertial coupling among 3-direction deflection, twist and rolling, which are represented by nonzero terms such as $\left[Q_\gamma^{u_3}\right]$, $\left[Q_\gamma^{\theta_2}\right]$, $\left[M_{u_1}^{\theta_2}\right]$, $\left\{Q_{u_3}^\gamma\right\}$, $\left[M_{u_3}^{\theta_2}\right]$, $\left\{Q_{\theta_2}^\gamma\right\}$, $\left[M_{\theta_2}^{u_1}\right]$, and $\left[M_{\theta_2}^{u_3}\right]$.

It is convenient and common practice to write the above equation as:

$$[M_t]\{U\} + [K_t]\{U\} = \{F\} \tag{2.67}$$

where we have rearranged the displacement vector $\{U\}$ as the following, and correspondingly the mass matrix $[M_t]$, the stiffness matrix $[K_t]$ and the generalized force vector $\{F\}$:

$$\{U\} = \left[\begin{array}{cccc} \gamma & D_1 & \cdots & D_n \end{array}\right]^T \tag{2.68}$$

where D_i is the generalized displacement vector of each node, which consist of three lineal components and three rotations and are given by

$$[D_i] = \left[\begin{array}{cccccc} u_{1i} & u_{2i} & u_{3i} & u'_{3i} & \theta_{2i} & u'_{1i} \end{array}\right] \tag{2.69}$$

2.2.3   Natural Frequencies and Mode Shapes

With the finite element discretization at hand, we would like to find the natural frequencies and mode shapes first, because later we will use those natural modes to conduct the aeroelastic analysis.

The free-vibration problem of Equation (2.67) gives us the corresponding eigenvalue problem:

$$[M_t]\{\varphi\} = \omega^2 [K_t]\{\varphi\} \tag{2.70}$$

where ω is the natural frequency and $\{\varphi\}$ is the corresponding eigenvector, i.e., the free-vibration mode. We normalize the eigenvector such that

$$\{\varphi\}^T [M_t]\{\varphi\} = 1 \tag{2.71}$$

The displacement $\{U\}$ is approximated as an expansion in the first m free-vibration

modes:

$$\{U\} = \begin{bmatrix} \varphi_1 & \varphi_2 & \cdots & \varphi_m \end{bmatrix} \begin{Bmatrix} q_1 \\ q_2 \\ \vdots \\ q_m \end{Bmatrix} = [\varphi]\{q\} \qquad (2.72)$$

where the q_i are the generalized coordinates for the entire dynamic system, and they are only functions of time. The behavior of these generalized coordinates determines the state of the entire dynamic system. Substituting Equation (2.72) into Equation (2.67), multiplying both sides by $[\varphi]^T$ and using Equation (2.71) lead to the equation governing q:

$$\left\{ \ddot{q} \right\} + [\Lambda]\{q\} = [\varphi]^T \{F\} \qquad (2.73)$$

where

$$[\Lambda] = \begin{bmatrix} \omega_1^2 & 0 & \cdots & 0 \\ 0 & \omega_2^2 & \cdots & 0 \\ \vdots & \vdots & \ddots & \vdots \\ 0 & 0 & \cdots & \omega_m^2 \end{bmatrix} \qquad (2.74)$$

2.3   Numerical Examples

As a numerical example, we analyze a high-aspect-ratio wing with a tapered planform of the type found on a HALE aircraft (see Hall (1999)). The semi-span planform of the HALE aircraft wing is shown in Figure 2-4. The aspect ratio of the semi-span wing is about 10. The airfoil is chosen to be the high-performance Wortmann FX 60-126 airfoil, and it is shown in Figure 2-5. The airfoil was designed in 1960's and has a 12.6% maximum thickness. Also shown in Figure 2-5 is the camber line as the dotted line, which is the mean line of the upper and lower surface. In the aerodynamic model, we use the surface consisting of the camber lines, which is commonly called the lifting surface, to represent the wing.

In the structural beam model of the wing, the elastic axis is chosen to be one-quarter of the chord length from the leading edge of the wing. A manufacturer of airframes

intended for use as weather-observation platforms provided the approximate structural properties given in Table 2-1. The table includes the stiffness constants as well as the offset of the mass center away from the elastic center, r_x and r_z. With the given EI_{xx}, a uniformly distributed load equal to 125% of the take off weight $10,000\ N$ would produce a deflection at the wing tips equal to 10% of the semi-wing span for a cantilever beam model.

$L = 10.8m$	$I_F = 500Kg\text{-}m^2$
$r_x = 0.15m$	$r_z = 0$
$EI_{xx} = 10^6 Nm^2$	$EI_{zz} = 50 \cdot EI_{xx}$
$GJ = 1.5 \cdot EI_{xx}$	$EA = 20 \times 10^6 N$
$\rho A = 10.0Kg/m$	$I_{22} = 1.5 \cdot \rho A$

Table 2.1: Propereties of the high-aspect-ratio wing used in the numerical example

Using these properties we can determine the natural frequencies and the free-vibration modes. Figure 2-6 shows the projection of finite element modes 1 through 6 onto the aerodynamic mesh with the rolling motion included, while Figure 2-7 shows the modes without the rolling motion. We will elaborate on how we project the mode shape onto aerodynamic mesh in Chapter 4. The first mode shown in Figure 2-6 is primarily the rolling motion. As a result of the inclusion of the overall rolling motion, asymmetric free-vibration modes appear. The symmetric modes and the asymmetric modes appear in turn as the natural frequencies increase. These asymmetric modes contain non-zero rolling motion. The symmetric modes do not have the rolling motion component and are not affected by the inclusion of the overall rolling motion; they have the same natural frequencies as the cantilever-beam model. This is clearly seen by comparing Figure 2-6 and Figure 2-7.

For the cantilever beam model, the first mode appears to be the first bending mode; it is mostly bending with a little torsion. The second mode is mostly the torsion with a little bending; it resembles what could be called the first torsion mode. The third mode resembles the second bending mode with a little torsion resembling the first torsion mode.

The fourth mode is purely the first in-plane fore and aft bending mode. The higher modes are expected to have few effects on the flutter analysis, since they have higher frequencies, which are harder to get excited. To accurately capture the higher frequencies, the time step size has to be sufficiently small. As we will demonstrate later, the time step size is related to the aerodynamic mesh used in the aerodynamic model. Smaller time steps require smaller aerodynamic-element size for the sake of accuracy.
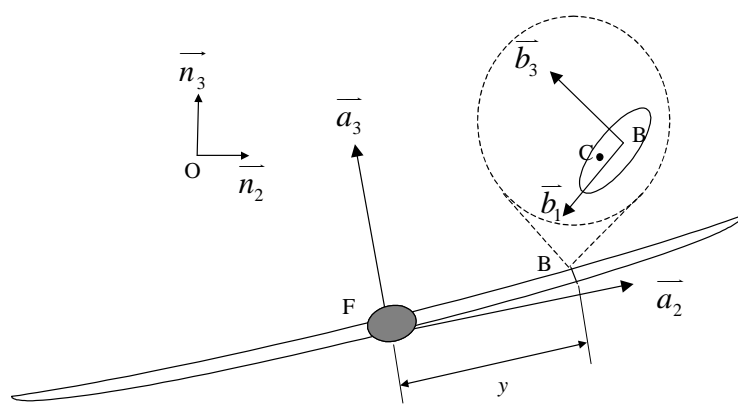
Figure 2-1: A schematic representation of the wing-mass configuration

$N_i^0:$

$N_i^1:$

$N_j^0:$

$N_j^1:$

$N_i:$

$N_j:$
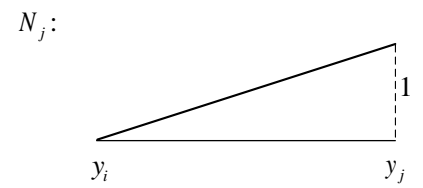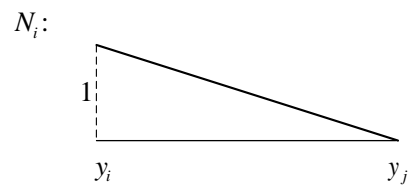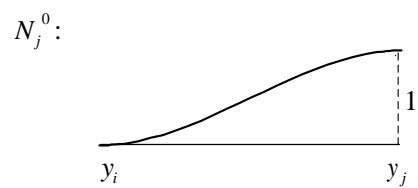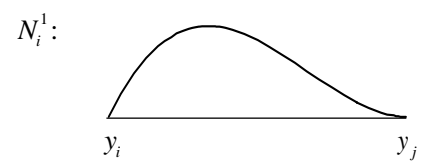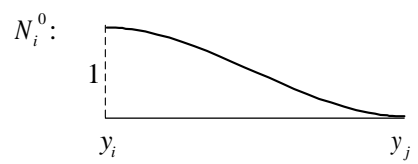
Figure 2-2: Finite element shape functions
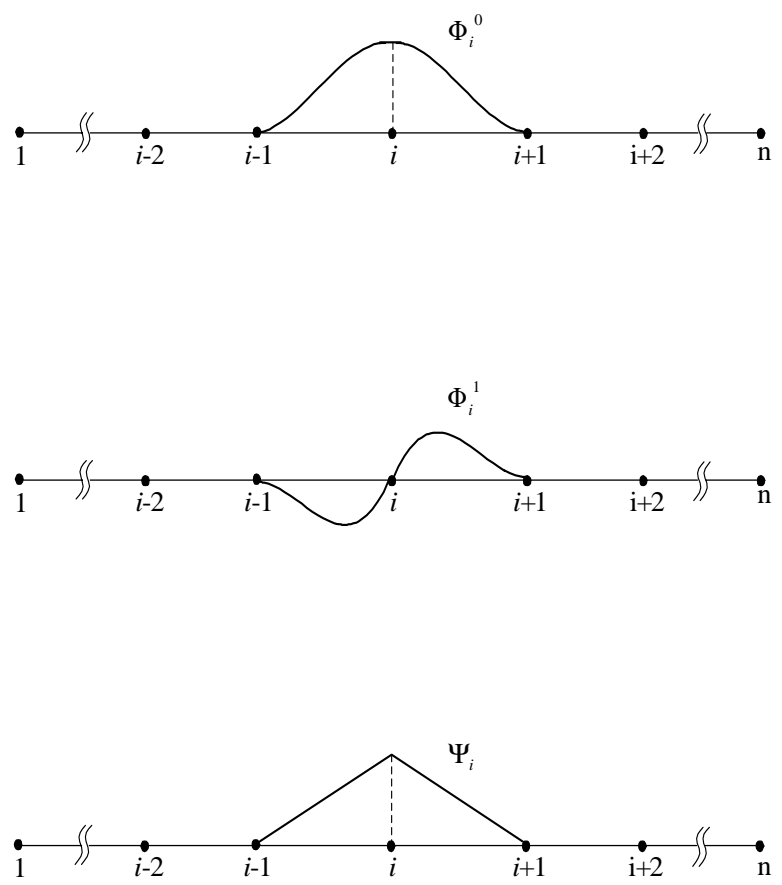
Figure 2-3: Finite element basis functions
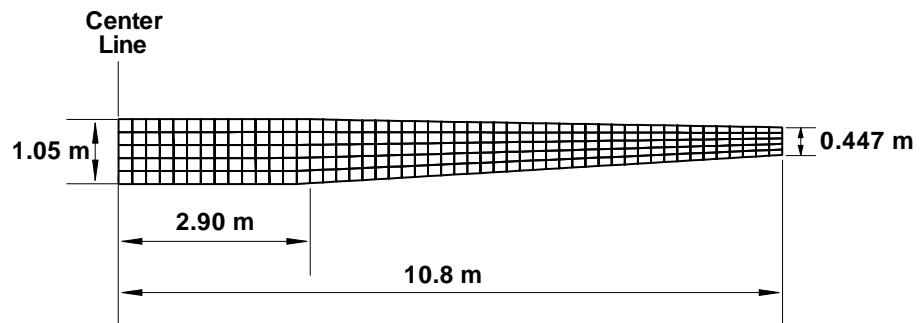
Figure 2-4: Semi-span HALE aircraft wing planform
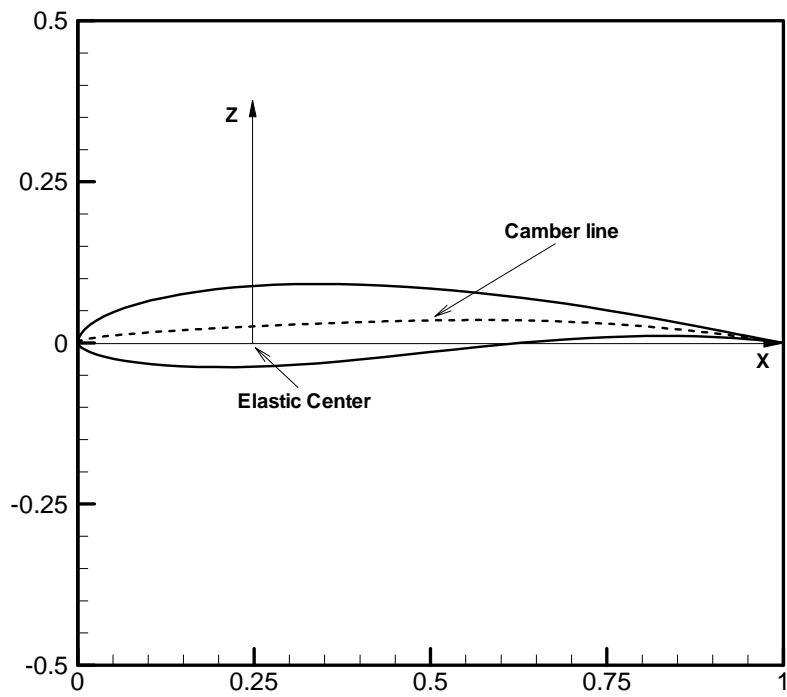
Figure 2-5: The Wortmann FX 60-126 airfoil

40
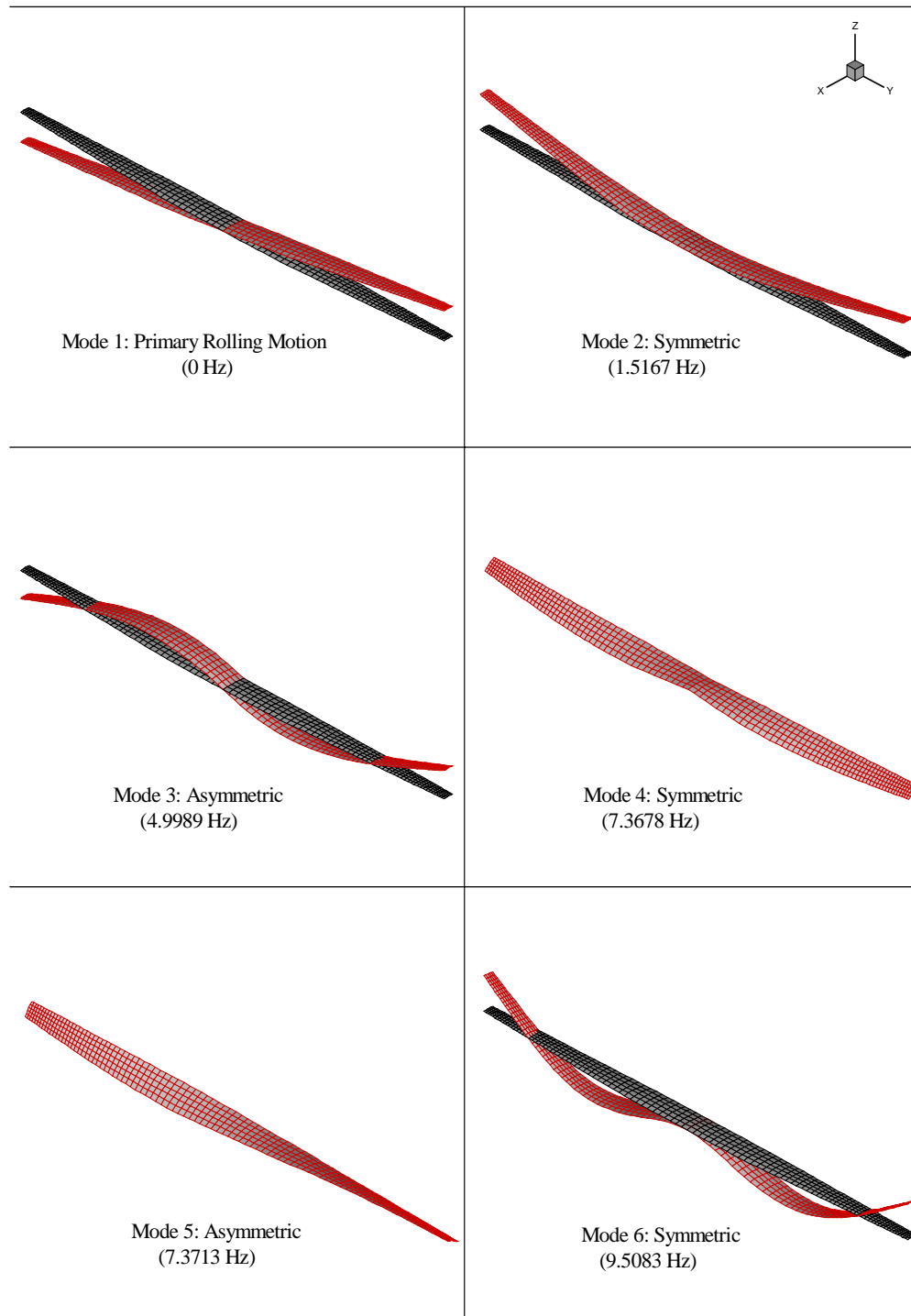
Figure 2-6: Projection of finite-element modes 1 through 6 onto the aerodynamic mesh with the rolling motion included (the dark shape represents the undeformed wing)

41
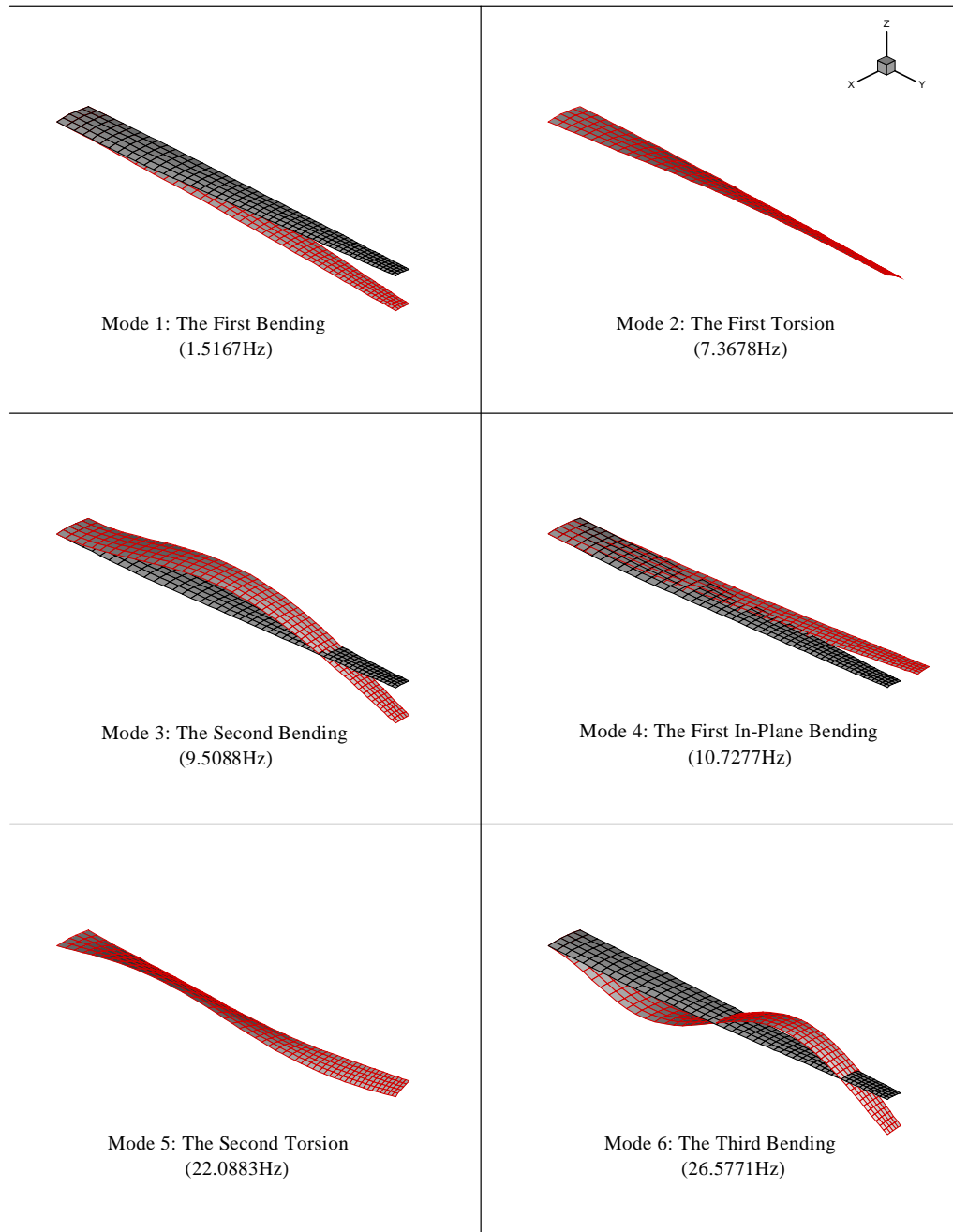
Figure 2-7: Projection of finite-element modes 1 through 6 onto the aerodynamic mesh without the rolling motion (the dark shape represents the undeformed wing)

Chapter 3

Aerodynamic Model

In this chapter, we describe the general unsteady vortex-lattice aerodynamic model used in this dissertation for analysis of both aerodynamic configurations and aeroelastic simulations.

The ultimate aerodynamic model would be based on the Navier-Stokes equations; a model in between that can account for compressibility is based on Euler equations. However, the complexity involved with this approach sometimes is intimidating, e.g., the entire flowfield must be gridded. In the case of the interaction between aerodynamics and structural deformations, the flowfield needs to be re-gridded at different time steps. The demands on computer resources and the time-cost are overwhelming. At the same time, for not complicated topologies and in the subsonic domain, the vortex-lattice method is much more efficient in terms of solution accuracy, memory requirement, and speed, which makes it more suitable to attack aeroelastic problems.

We first give a description of the model, and then present some numerical examples to verify and demonstrate the capability of the model.

3.1   Description of the Vortex Lattice Method

The velocity field $\overrightarrow{V_F}$ can be expressed as the sum of two velocities:

$$\overrightarrow{V_F} = \overrightarrow{V_\infty} + \overrightarrow{V_D} \tag{3.1}$$

where $\overrightarrow{V_\infty}$ is the velocity in the oncoming stream, $\overrightarrow{V_D}$ is the disturbance velocity due to the presence of the body or the wing. The key component in the general unsteady vortex lattice method is how to describe this disturbance velocity.

When a fluid flows past a body, because of the effect of viscosity, a boundary layer near the surface of the body is formed. The fluid in contact with the surface adheres to the surface, which is usually called the no-slip condition. Away from the surface the fluid is in motion. At large Reynolds numbers (usually the case for aero- and hydro-dynamics), the boundary layer becomes very thin. Inside the boundary layers, viscous effects and rotational effects are important; outside the thin boundary layers, the velocity gradients are small and the viscous forces are negligible. The fluid outside the boundary layer may be regarded, with a higher degree of accuracy, as an inviscid fluid.

The thin boundary layer at infinite-Reynolds-number approximation results in a discontinuity in the tangential velocity. This velocity discontinuity essentially creates the vorticity, thus the boundary layer can be treated as a vortex sheet bound to the body. In addition, the viscosity of the fluid (no matter how small it might be) causes vorticity to be shed from the sharp edges of the wings, e.g., the wing tips and the trailing edge, to form the wake. Inside the wake, viscous effects are still dominant just as in the boundary layer. The vorticity associated with the wake is called free vortex sheet.

3.1.1 Velocity Field Due to Vortex Distribution

There is a kinematic relationship between the vorticity and the velocity. To obtain the velocity $\overrightarrow{V}$ in terms of the vorticity $\overrightarrow{\Omega}$ we need to invert the definition of the vorticity:

$$\overrightarrow{\Omega} = curl\ \overrightarrow{V} = \nabla \times \overrightarrow{V} \tag{3.2}$$

Considering an incompressible fluid, we have

$$div \ \vec{V} = \nabla \cdot \vec{V} = 0 \tag{3.3}$$

Equation (3.3) gives the continuity equation. From this equation, we may express $\vec{V}$ as the curl of some other vector field, say of $\vec{\chi}$. Hence we set

$$\vec{V} = curl \ \vec{\chi} \tag{3.4}$$

Since the curl of any gradient vector is zero, the vector $\vec{\chi}$ is indeterminate to the extent of the gradient of a scalar function of position and time. To make it determinate, we assume that

$$div \ \vec{\chi} = 0 \tag{3.5}$$

From Equation (3.4) it follows that

$$\begin{aligned} curl \ \vec{V} &= curl \ (curl \ \vec{\chi}) = grad \ (div \ \vec{\chi}) - \nabla^2 \vec{\chi} \\ &= -\nabla^2 \vec{\chi} \end{aligned} \tag{3.6}$$

Combining Equation (3.2) and (3.6) yields

$$\nabla^2 \ \vec{\chi} = -\vec{\Omega} \tag{3.7}$$

This is Poisson's equation for $\vec{\chi}$. We call $\vec{\chi}$ a vector potential. Once $\vec{\chi}$ is determined as a solution of Equation (3.7), the velocity field than can be found from Equation (3.4).

The solution of Equation (3.7) is expressed as (details can be found in Karamcheti (1980)):

$$\vec{\chi}(\vec{r}, t) = \frac{1}{4\pi} \iiint\limits_{R} \frac{\vec{\Omega}(\vec{s}, t)}{|\vec{r} - \vec{s}|} d\tau \tag{3.8}$$

where $\vec{\Omega}(\vec{s}, t)d\tau$ is an element of the vorticity distribution situated at the point $\vec{s}$, R is the region in which the vorticity is distributed, and $|\cdot|$ denotes the magnitude of a vector

45

(see Figure 3-1). The velocity field is then given by

$$\overrightarrow{V} = curl\ \overrightarrow{\chi} = \frac{1}{4\pi}\ curl\ \iiint\limits_R \frac{\overrightarrow{\Omega}\left(\overrightarrow{s},t\right)}{\left|\overrightarrow{r}-\overrightarrow{s}\right|}d\tau \tag{3.9}$$

3.1.2 Biot-Savart Law

In the real flowfield, the body is covered with a boundary layer, which we approximate as a sheet of vorticity. In order to expedite the calculation of the velocity associated with the vortex sheets, they are replaced with lattices of short, straight discrete vortex lines. When the vorticity is concentrated in a straight discrete vortex segment, as in the lattice, the relationship giving the velocity in terms of the vorticity (or circulation around the segment) becomes the well-known Biot-Savart law.

Some terminologies are used through the description of the model. The definitions of them are given here first. The field lines of vorticity are called vortex lines. Just as the field lines of velocity, at any point in the flow field, the direction of the vorticity vector is given by the direction, at that point, of the vortex line passing through that point. If we consider a closed curve and draw all the vortex lines passing through it, a vortex tube is formed. A vortex tube of infinitesimal cross-sectional area is known as a vortex filament.

Figure 3-2 shows a vortex filament with circulation strength Γ. The differential volume element $d\tau$ of this filament is chosen to be the cylinder formed by a cross-sectional surface $\overrightarrow{n}\,dS$ and an element of length $d\overrightarrow{l}$ along the filament. The contribution to the vector potential $\overrightarrow{\chi}$ at a field point $\overrightarrow{r}$, from the vortex element at $\overrightarrow{s}$ is given by

$$d\overrightarrow{\chi}\left(\overrightarrow{r}\right) = \frac{1}{4\pi}\frac{\overrightarrow{\Omega}\left(\overrightarrow{s}\right)}{\left|\overrightarrow{r}-\overrightarrow{s}\right|}\left(\overrightarrow{n}\,dS \cdot d\overrightarrow{l}\right) \tag{3.10}$$

Considering

$$d\overrightarrow{l} = \frac{\overrightarrow{\Omega}}{\Omega}dl \tag{3.11}$$

and

$$\overrightarrow{\Omega} \cdot \overrightarrow{n}\,dS = \Gamma \tag{3.12}$$

46

Equation (3.10) can be rewritten as

$$d\vec{\chi}\left(\vec{r}\right) = \frac{\Gamma}{4\pi} \frac{d\vec{l}}{|\vec{r} - \vec{s}|} \qquad (3.13)$$

Then the velocity at position $\vec{r}$ associated with the differential vortex filament is given by

$$
\begin{aligned}
d\vec{V}\left(\vec{r}\right) &= curl_r \left(\frac{\Gamma}{4\pi} \frac{d\vec{l}}{|\vec{r} - \vec{s}|} \right) \\
&= \frac{\Gamma}{4\pi} \frac{d\vec{l} \times (\vec{r} - \vec{s})}{|\vec{r} - \vec{s}|^3}
\end{aligned}
\qquad (3.14)
$$

This is known as the Biot-Savart law. The velocity at $\vec{r}$ due to the whole vortex filament is obtained by integration of the expression (3.14) over the length of the filament. We thus have

$$\vec{V}\left(\vec{r}\right) = \frac{\Gamma}{4\pi} \int \frac{d\vec{l} \times (\vec{r} - \vec{s})}{|\vec{r} - \vec{s}|^3} \qquad (3.15)$$

Since Γ is the strength of the filament, it is a constant and hence appears outside the integral.

In some cases, the integral in Equation (3.15) can be simplified. The first example is an infinitely long straight vortex filament of strength Γ shown in Figure 3-3. To calculate the velocity field we choose the origin of the coordinate system at some point on the filament. Then according to Equation (3.15), the velocity at a field point is given by

$$\vec{V}\left(\vec{r}\right) = \frac{\Gamma}{4\pi} \int_{-\infty}^{\infty} \frac{d\vec{s} \times (\vec{r} - \vec{s})}{|\vec{r} - \vec{s}|^3} \qquad (3.16)$$

where $d\vec{s}$ is an element of the filament at $\vec{s}$. By denoting $\vec{r} - \vec{s}$ by $\vec{r_1}$, the direction of $d\vec{s} \times \vec{r_1}$ by unit vector $\vec{e}$, and the angle measured from $d\vec{s}$ to $\vec{r}$ by θ (such that $0 \leq \theta \leq \pi$), we have

$$d\vec{s} \times (\vec{r} - \vec{s}) = d\vec{s} \times \vec{r_1} = \vec{e}\, r_1 \sin\theta\ ds \qquad (3.17)$$

47

and the above expression for the velocity becomes

$$
\vec{V}\left(\vec{r}\right) \;=\; \vec{e}\,\frac{\Gamma}{4\pi}\int_{-\infty}^{\infty}\frac{\sin\theta}{r_1^2}ds = \vec{e}\,\frac{\Gamma}{4\pi h}\int_{0}^{\pi}\sin\theta\;d\theta \qquad (3.18)
$$

$$
=\; \frac{\Gamma}{2\pi h}\,\vec{e}
$$

where h defines the normal distance from the field point to the filament.

We can conclude from Equation (3.18) that the flow field associated with an infinite long vortex filament is irrotational everywhere except along the filament where $h = 0$, and that it is essential two-dimensional flow or point vortical flow. The plane of motion is normal to the vortex filament.

The second case involves a semi-infinite straight vortex filament extending from 0 to ∞ (see Figure 3-4). The velocity field is given by

$$
\vec{V}\left(\vec{r}\right) \;=\; \vec{e}\,\frac{\Gamma}{4\pi}\int_{0}^{\infty}\frac{\sin\theta}{r_1^2}ds = \vec{e}\,\frac{\Gamma}{4\pi h}\int_{\theta_0}^{\pi}\sin\theta\;d\theta \qquad (3.19)
$$

$$
=\; \vec{e}\,\frac{\Gamma}{4\pi h}\left(1+\cos\theta_0\right)
$$

Thus, if the field point is located in the plane $\theta_0 = \pi/2$, the magnitude of the velocity is $\Gamma/\left(4\pi h\right)$. If the field point is located in a plane situated far away from the origin of the vortex filament, the angle θ_0 tends to be zero, and the magnitude of the velocity tends to $\Gamma/\left(2\pi h\right)$, the value for an infinite vortex filament.

The velocity field due to a finite segment of a straight vortex filament is given by

$$
\vec{V}\left(\vec{r}\right) \;=\; \vec{e}\,\frac{\Gamma}{4\pi}\int_{\theta_1}^{\theta_2}\frac{\sin\theta}{r_1^2}ds = \vec{e}\,\frac{\Gamma}{4\pi h}\int_{\theta_1}^{\theta_2}\sin\theta\;d\theta \qquad (3.20)
$$

$$
=\; \vec{e}\,\frac{\Gamma}{4\pi h}\left(\cos\theta_1 - \cos\theta_2\right)
$$

This formula is the most used and intensively evaluated in the vortex-lattice method in this dissertation. For the sake of convenience in programing, we rewrite Equation

(3.20) in terms of vector manipulations.

From Figure 3-5, we can see that

$$\overrightarrow{AB} \times \overrightarrow{AP} = \left|\overrightarrow{AB}\right| \left|\overrightarrow{AP}\right| \sin\theta_1 \; \overrightarrow{e} \tag{3.21}$$

$$\left|\overrightarrow{AB} \times \overrightarrow{AP}\right| = \left|\overrightarrow{AB}\right| \left|\overrightarrow{AP}\right| \sin\theta_1 = \left|\overrightarrow{AB}\right| \; h \tag{3.22}$$

$$h = \frac{\left|\overrightarrow{AB} \times \overrightarrow{AP}\right|}{\left|\overrightarrow{AB}\right|} \tag{3.23}$$

$$\overrightarrow{e} = \frac{\overrightarrow{AB} \times \overrightarrow{AP}}{\left|\overrightarrow{AB} \times \overrightarrow{AP}\right|} \tag{3.24}$$

$$\overrightarrow{AB} \cdot \overrightarrow{AP} = \left|\overrightarrow{AB}\right| \left|\overrightarrow{AP}\right| \cos\theta_1, \quad \overrightarrow{AB} \cdot \overrightarrow{BP} = \left|\overrightarrow{AB}\right| \left|\overrightarrow{BP}\right| \cos\theta_2 \tag{3.25}$$

$$\cos\theta_1 = \frac{\overrightarrow{AB} \cdot \overrightarrow{AP}}{\left|\overrightarrow{AB}\right| \left|\overrightarrow{AP}\right|}, \quad \cos\theta_2 = \frac{\overrightarrow{AB} \cdot \overrightarrow{BP}}{\left|\overrightarrow{AB}\right| \left|\overrightarrow{BP}\right|} \tag{3.26}$$

Substituting the expressions for $\overrightarrow{e}$, h, $\cos\theta_1$, and $\cos\theta_2$ into Equation (3.20), we obtain

$$
\begin{aligned}
\overrightarrow{V}(\overrightarrow{r}) &= \overrightarrow{e} \frac{\Gamma}{4\pi h} \left(\cos\theta_1 - \cos\theta_2\right) \\
&= \frac{\Gamma}{4\pi} \frac{1}{\frac{\left|\overrightarrow{AB} \times \overrightarrow{AP}\right|}{\left|\overrightarrow{AB}\right|}} \frac{\overrightarrow{AB} \times \overrightarrow{AP}}{\left|\overrightarrow{AB} \times \overrightarrow{AP}\right|} \left(\frac{\overrightarrow{AB} \cdot \overrightarrow{AP}}{\left|\overrightarrow{AB}\right| \left|\overrightarrow{AP}\right|} - \frac{\overrightarrow{AB} \cdot \overrightarrow{BP}}{\left|\overrightarrow{AB}\right| \left|\overrightarrow{BP}\right|}\right) \\
&= \frac{\Gamma}{4\pi} \frac{\overrightarrow{AB} \times \overrightarrow{AP}}{\left|\overrightarrow{AB} \times \overrightarrow{AP}\right|^2} \left(\frac{\overrightarrow{AB} \cdot \overrightarrow{AP}}{\left|\overrightarrow{AP}\right|} - \frac{\overrightarrow{AB} \cdot \overrightarrow{BP}}{\left|\overrightarrow{BP}\right|}\right)
\end{aligned}
\tag{3.27}
$$

3.1.3   Spatial Conservation of Vorticity

For vortex-lattice methods several important theorems have to be mentioned: the theorem of spatial conservation of vorticity, and the theorems of Helmholtz and Kelvin. We first discuss the spatial conservation of vorticity.

Consider, at any instant, a vortex tube drawn in the flow field. Denote by R the

region of space enclosed between the wall of the tube and any two surfaces S_1 and S_2 which cut the tube (see Figure 3-6). Because the divergence of the curl of any vector is equal to zero, we have

$$div \ \overrightarrow{\Omega} = div \ \left(curl \ \overrightarrow{V}\right) = 0 \tag{3.28}$$

According to Green's theorem, we have

$$\iint_{S_1} \overrightarrow{\Omega} \cdot \overrightarrow{n} \ dS + \iint_{S_2} \overrightarrow{\Omega} \cdot \overrightarrow{n} \ dS + \iint_{S_w} \overrightarrow{\Omega} \cdot \overrightarrow{n} \ dS = \iint_{S} \overrightarrow{\Omega} \cdot \overrightarrow{n} \ dS = \iiint_{R} div \ \overrightarrow{\Omega} = 0 \tag{3.29}$$

where S_w denotes the surface of the wall of the tube in the portion under consideration. On the wall of the tube, $\overrightarrow{\Omega}$ lies in the surface S_w. Hence the integral over S_w vanishes, i.e.,

$$\iint_{S_w} \overrightarrow{\Omega} \cdot \overrightarrow{n} \ dS = 0 \tag{3.30}$$

Consequently,

$$\iint_{S_1} \overrightarrow{\Omega} \cdot \overrightarrow{n} \ dS + \iint_{S_2} \overrightarrow{\Omega} \cdot \overrightarrow{n} \ dS = 0 \tag{3.31}$$

In the above equation, $\overrightarrow{n}$ represents the outward normal with reference to the region R. If we draw the normals on the surfaces S_1 and S_2 in the same sense and denote them by $\overrightarrow{n_1}$ and $\overrightarrow{n_2}$, respectively, Equation (3.31) can be rewritten as

$$\iint_{S_1} \overrightarrow{\Omega} \cdot \overrightarrow{n_1} \ dS = \iint_{S_2} \overrightarrow{\Omega} \cdot \overrightarrow{n_2} \ dS \tag{3.32}$$

This states that the flow of vorticity through any cross-sectional surface of a vortex tube is equal to the flow of vorticity through any other cross-section surface of the tube. This is true at every instant of time. Thus at any cross surface of the vortex tube, S, we have

$$\Gamma = \iint_{S} \overrightarrow{\Omega} \cdot \overrightarrow{n} \ dS = \text{ constant} \tag{3.33}$$

Equation (3.33) illustrates that the circulation around a vortex tube remains constant

all along the tube. An important consequence of the spatial conservation of vorticity is that a vortex tube and also a vortex filament or a vortex line, cannot begin or end abruptly in a fluid. It should either form a close ring or end at infinity or at a solid or free surface.

3.1.4 Theorems of Helmholtz and Kelvin

Helmholtz's theorem deals with the rate of change of vorticity. It states that: *In the motion of an ideal fluid subjected to irrotational body forces, the material rate change of the outflow of vorticity through any surface element moving with the fluid is permanently zero, or, equivalently, the outflow of vorticity through any surface element moving with the fluid remains a constant for all times. In this sense vorticity is convected with the fluid.*

Kelvin's theorem is also called the theorem of temporal conservation of circulation: *In the motion of an inviscid fluid, the rate of change of circulation around any fluid curve is permanently zero if the body forces are irrotational and if there is a single-valued pressure-density relation, or, equivalently under these conditions, the circulation around a fluid curve remains a constant for all times as the curve moves with the fluid.*

According to these two theorems, for an ideal fluid under the action of potential body forces, we have

$$\frac{D}{Dt}\Gamma_{\mathbb{C}} = \frac{D}{Dt}\iint_S \overrightarrow{\Omega}\cdot\overrightarrow{n}\,dS = 0 \tag{3.34}$$

where S is any surface bounded by a fluid curve $\mathbb{C}$, $\frac{D}{Dt}$ represents the substantial time derivative.

To see the implication of the theorems of Helmholtz and Kelvin, we consider an infinitesimal surface element $\overrightarrow{n}\,dS$ which is surrounded by curve c on a vortex sheet. From Equation (3.34), we have

$$\frac{D}{Dt}\Gamma_c = \frac{D}{Dt}\left(\overrightarrow{\Omega}\cdot\overrightarrow{n}\,dS\right) = 0 \tag{3.35}$$

We can conclude from Equation (3.35) that because at one instant $\overrightarrow{\Omega} \cdot \overrightarrow{n}$ is equal to zero by the definition of vortex sheet, it remains zero at all times for that surface element. Therefore a surface which is a vortex sheet at one instant remains a vortex sheet for all times. In other words, the fluid particles that are part of a vortex sheet at some instant are part of it for all times. Furthermore, it follows that fluid particles which belong to a vortex tube, or vortex filament, or a vortex line always remain so.

Another observation from the theorems of Helmholtz and Kelvin is that the circulation strength of a vortex tube or a vortex filament remains constant for all times as the tube or filament floats along, regardless of the changes experienced by the vortex tube or filament.

The theorems of Helmholtz and Kelvin along with the spatial conservation of vorticity provide the theoretical bases for the vortex-lattice approximation of the bound vortex sheet and wake formation in our vortex-lattice method.

3.1.5 Vortex Sheet Discretization and No-penetration Boundary Condition

In the present simulations, the wing section is represented by the surface consisting of camber lines, the so-called lifting surface. The lifting surface and the closed-body surfaces representing the fuselages (if there are any) are approximated by an arbitrary number of non-planar quadrilateral elements, which form the aerodynamic grid. Each element is encircled by a closed loop of discrete vortex segments lying along its edges. The result is a net or lattice of discrete-vortex lines that covers the surfaces. Taking the circulations around all the individual vortex segments of a given loop to be the same automatically satisfies the requirement of spatial conservation of circulation.

Experience with the vortex-lattice method suggests that rectangular elements work much better than other shapes of elements. Consequently, we use rectangular elements as much as possible except in those places where we are forced to use triangular elements, e.g., at the nose of the aircraft's fuselage, the inlet of the engines, etc.

For element number i (see Figure 3-7), the value of this loop circulation is G_i. The circulation in a given segment is obtained by taking all the adjoining loops into account all of which have the given segment in common. For example, in Figure 3-7, the circulation around segment j of the loop that encircles element i is given by

$$\Gamma_{ij} = G_k - G_i \tag{3.36}$$

where i and $k = 1, 2, \cdots, N$, and $j = 1, 2, 3, 4$, and N is the number of elements.

In the real flow, the velocity associated with the vorticity in the boundary layers and wakes interacts with the oncoming stream in such a way that the no-slip and no-penetration boundary conditions are satisfied on the surfaces of the configuration. Imitating the real situation, we obtain the G_i's by imposing the no-penetration conditions at only one point in each element, the so-called control point, which can be expressed as follows:

$$\left(\overrightarrow{V_\infty} + \overrightarrow{V_D} - \overrightarrow{V_B} \right) \cdot \overrightarrow{n} = 0 \tag{3.37}$$

where the disturbance velocity $\overrightarrow{V_D}$ is generated not only by the lifting surface and body surface bounded vortices, but also by the wake vortices, $\overrightarrow{V_B}$ is the velocity of the lifting surface or body surface at the control point, and $\overrightarrow{n}$ is the unit vector normal to the surfaces. The control points are usually the centroids of the elements.

The approximation comes from two sources: (1) The Reynolds number is assumed to be infinite so that the boundary layer is simply a discontinuity in the tangential component of the velocity and so the thickening of the boundary layers near the trailing edges of the wing and bodies cannot be taken into account. (2) The line of separation is assumed to be known. It cannot be determined; the user must provide it.

$\overrightarrow{V_D}$ is computed by repeated applications of the Biot-Savart law. Consequently, the velocity field satisfies the continuity equation and decays as the distance from the vortex segment increases. The portion of the velocity associated with the vorticity bound on the surface of the configuration can be expressed in terms of an influence matrix. An

53

element of the influence matrix, A_{ij}, is the normal component of velocity at the control point of element i generated by unit circulation around the vortex segments enclosing element j. The no-penetration condition becomes

$$\sum_{j=1}^{N} A_{ij} G_j = - \left(\overrightarrow{V_\infty} + \overrightarrow{V_{wi}} - \overrightarrow{V_{Bi}} \right) \cdot \overrightarrow{n_i} \qquad \text{for } i = 1, 2, \cdots N \qquad (3.38)$$

where $\overrightarrow{V_{wi}}$ is the velocity associated with the vorticity in the wake at the control point of element i, and N is the total number of the elements. How to calculate the velocity $\overrightarrow{V_{wi}}$ remains to be discussed.

The unit normal vector $\overrightarrow{n_i}$ is obtained from the cross products of the diagonals:

$$\overrightarrow{n_i} = \frac{\overrightarrow{CA} \times \overrightarrow{DB}}{\left| \overrightarrow{CA} \times \overrightarrow{DB} \right|} \qquad (3.39)$$

where A, B, C, D are the four vertices of element i, see Figure 3-7.

3.1.6 Kutta Condition and Vorticity Shedding

The Kutta condition is imposed by shedding vorticity from the lines of separation into the wake, and the wake is formed by convecting the vortex segments there with the local particle velocity while holding the circulations around them constant. When the viscous effects are small, this procedure eliminates discontinuities in the pressure field and, therefore, renders the wakes force-free. The shedding-convecting process generates the vortex lattice that represents the wake as part of the solution. It might help to take a look at a fairly simple example, which will illustrate this shedding-convecting process.

Figure 3-8 shows a 3×4 lattice which simulates half a wing. The flow is symmetric about the center chord (at which Nodes 1, 6, 11, and 16 are located) plane of the wing. The vorticity is shed from the right wing tip and the trailing edge. At $t = 0$, there is no wake vorticity yet. We solve the algebraic equation (3.38) and obtain the circulation for each element, $G_i(0)$.

At $t = \Delta t$, the vorticity begins to shed from the wing tip and the trailing edge. The

local velocity $\overrightarrow{V_F}$ at each aerodynamic node along the trailing edge (Nodes 16, 17, 18, 19) and wing tip (Nodes 5, 10, 15) is calculated through Biot-Savart law with $G_i(0)$, $(i = 1, 2, \cdots N)$ plus the free stream velocity. The displacements of the fluid particles at those nodes are determined by

$$\Delta \overrightarrow{r} = \int_{0}^{\Delta t} \overrightarrow{V_F} \, dt \qquad (3.40)$$

Equation (3.40) is usually approximated by

$$\Delta \overrightarrow{r} = \overrightarrow{V_F} \, \Delta t \qquad (3.41)$$

This approximation is proved to be efficient and successful. With $\Delta \overrightarrow{r}$, the fluid particles at Nodes 16, 17, 18, 19, 15, 10 and 5 move to the new position; we denote them by Points 16', 17', 18', 19', 15', 10' and 5', respectively, see Figure 3-9. Here the first row of the wake is formed. Each element in the first row of the wake has a circulation same as its adjoining bound vortex element, i.e., the circulation in wake element formed by 16, 17, 17', and 16' is $G_9(0)$, the circulation in wake element formed by 17, 18, 18', and 17' is $G_{10}(0)$, and so forth. Thus when we solve Equation (3.38), there will be the contributions from this first row of wake vortices, $\overrightarrow{V_w}$'s in the right hand side of the equation. Note that the wake element encircled by Nodes 19, 20, 15, 15', 19' is different from other elements; it has five vortex segments instead which contribute to the velocity field. We call it as the corner wake element. The results of circulations are denoted by $G_i(\Delta t)$.

In Figure 3-10, the situation for $t = 2\Delta t$ is presented. Same as for the procedure at $t = \Delta t$, the displacements of the fluid particles at Nodes 16, 17, 18, 19, 15, 10 and 5, and also Points 16', 17', 18', 19', 15', 10' and 5' in Figure 3-9 are computed using $G_i(\Delta t)$. For simplicity, we still denote the new position for the fluid particles at Nodes 16, 17, 18, 19, 15, 10 and 5 by Points 16', 17', 18', 19', 15', 10' and 5', respectively. While the new positions of Point 16', 17', 18', 19', 15', 10' and 5' at $t = \Delta t$ are denoted by Points 16", 17", 18", 19", 15", 10' and 5", respectively. The starting vortices such as the element formed by 16', 17', 17", and 16", the element formed by 17', 18', 18", and 17", etc.,

remain their circulation strength. The new shed vortices like the element formed by 16, 17, 17', and 16', the element formed by 17, 18, 18', and 17', have the same circulation as their adjoining bound vortex elements had at time $t = \Delta t$. For example, the element formed by 16, 17, 17', and 16' has the circulation of $G_9\left(\Delta t\right)$; the element formed by 17, 18, 18', and 17' has the circulation of $G_{10}\left(\Delta t\right)$.

Now the $\overrightarrow{V_w}$'s in the right hand side of Equation (3.38) are computed with this newly formed wake with two-rows of elements. The solution of Equation (3.38) is denoted by $G_i\left(2\Delta t\right)$.

The procedure described above can be continued for any desired number of steps. At each time step, new vortices are formed, shed and convected away from the edges to form the wake. From the way the wake is formed, it is clear that the wake stores the history of the circulation strength in those vortex elements where the wake is shed. We say that the wake is the historian of the flow. From the Biot-Savart law, the velocity is inversely proportional to the distance of the field point away from the vortex filament, so the wake vortices which are far from the wing or the body have negligible effects on the wing or the body. In numerical applications, we can safely cut off those wake vortices. In practice we give a fixed maximum number for the rows of the wake. Those wake vortices that are far down stream are neglected.

When steady-state solution is desired, the body is given an impulsive start and then have it move with constant velocity until the steady state develops.

3.1.7   Aerodynamic Loads

Aerodynamic loads are computed using Bernoulli's equation for unsteady flows:

$$\frac{\partial \Phi\left(\overrightarrow{r},t\right)}{\partial t} + \frac{1}{2}\nabla\Phi\left(\overrightarrow{r},t\right)\cdot\nabla\Phi\left(\overrightarrow{r},t\right) + \frac{p\left(\overrightarrow{r},t\right)}{\rho} = H\left(t\right) \tag{3.42}$$

where Φ is total velocity potential, i.e.,

$$\nabla\Phi\left(\overrightarrow{r},t\right) = \overrightarrow{V_\infty} + \overrightarrow{V_D} = \overrightarrow{V_F} \tag{3.43}$$

p is the pressure, ρ is the constant density of the fluid, $\frac{\partial \Phi(\overrightarrow{r},t)}{\partial t}$ is evaluated at a point fixed in the inertial reference frame, and $H(t)$ is specified by evaluating the conditions at infinity, so that

$$H(t) = \frac{1}{2}V_\infty^2 + \frac{p_\infty}{\rho_\infty} \tag{3.44}$$

and it is actually independent of time. In the aeroelastic analysis in this dissertation, ρ_∞ is chosen to be $1.020\ Kg/m^3$ unless otherwise specified.

Equation (3.42) can be rewritten as

$$\begin{aligned}
\frac{p}{\rho} - \frac{p_\infty}{\rho} &= \frac{1}{2}V_\infty^2 - \frac{1}{2}\overrightarrow{V_F} \cdot \overrightarrow{V_F} - \frac{\partial \Phi(\overrightarrow{r},t)}{\partial t} \tag{3.45} \\
&= \frac{1}{2}V_\infty^2 \left[1 - \left(\frac{V_F}{V_\infty}\right)^2 - \frac{2}{V_\infty^2}\frac{\partial \Phi(\overrightarrow{r},t)}{\partial t} \right]
\end{aligned}$$

$$\frac{p - p_\infty}{\rho} = \frac{1}{2}V_\infty^2 \left[1 - \left(\frac{V_F}{V_\infty}\right)^2 - \frac{2}{V_\infty^2}\frac{\partial \Phi(\overrightarrow{r},t)}{\partial t} \right] \tag{3.46}$$

$$C_p = \frac{p - p_\infty}{\frac{1}{2}\rho V_\infty^2} = 1 - \left(\frac{V_F}{V_\infty}\right)^2 - \frac{2}{V_\infty^2}\frac{\partial \Phi(\overrightarrow{r},t)}{\partial t} \tag{3.47}$$

where C_p is usually called as the coefficient of pressure.

By introducing nondimensional variables with the characteristic length and velocity, we can nondimensionalize Equation (3.47):

$$V^* = \frac{V_F}{V_C}, \quad \Phi^* = \frac{\Phi}{V_C L_C}, \quad t^* = \frac{t}{T_C} = \frac{t}{L_C/V_C} \tag{3.48}$$

where the superscript $*$ denotes nondimensional variables, and V_C, L_C, and T_C are characteristic speed, length and time respectively. It is common to choose the characteristic velocity to be the freestream speed or a speed characterizing the forward motion of the wing or the body. L_C is usually about the size of one typical element of the aerodynamic mesh.

For convenience, we choose

$$V_C = V_\infty \tag{3.49}$$

In the case when the body is moving in the still air, the speed characterizing the forward motion of the wing or the body can be regarded as the characteristic speed. Experiences show that it is much better for the wake elements to have the similar size as the bound vortex sheet elements, therefore, the nondimensional time step size is chosen around 1. Usually we just set it to be 1.

Equation (3.47) becomes

$$C_p = 1 - V^{*2} - 2\frac{\partial \Phi^*}{\partial t^*} \tag{3.50}$$

Just as when we applied the no-penetration condition, we evaluate the aerodynamic loads at the control points of the aerodynamic mesh. The pressure difference across the lifting surface at a control point is defined as the pressure below the vortex sheet (denoted by subscript L) minus the pressure above the vortex sheet (denoted by subscript U), i.e.,

$$
\begin{align}
\Delta C_p &= (C_p)_L - (C_p)_U \tag{3.51} \\
&= (V_U^*)^2 - (V_L^*)^2 + 2\left(\frac{\partial \Phi^*}{\partial t^*}|_U - \frac{\partial \Phi^*}{\partial t^*}|_L\right) \tag{3.52} \\
&= \overrightarrow{V_U^*} \cdot \overrightarrow{V_U^*} - \overrightarrow{V_L^*} \cdot \overrightarrow{V_L^*} + 2\left(\frac{\partial \Phi^*}{\partial t^*}|_U - \frac{\partial \Phi^*}{\partial t^*}|_L\right) \tag{3.53}
\end{align}
$$

where $\frac{\partial \Phi^*}{\partial t^*}|_U$ means that $\frac{\partial \Phi^*}{\partial t^*}$ is evaluated at the control points' upper surface, while $\frac{\partial \Phi^*}{\partial t^*}|_L$ means that $\frac{\partial \Phi^*}{\partial t^*}$ is evaluated at the control points' lower surface.

Evaluation of $\overrightarrow{V_U^*} \cdot \overrightarrow{V_U^*} - \overrightarrow{V_L^*} \cdot \overrightarrow{V_L^*}$

The velocities at the upper and lower surface of the vortex sheet may be rewritten as

$$\overrightarrow{V_U^*} = \overrightarrow{V_m^*} + \frac{\Delta \overrightarrow{V^*}}{2} \tag{3.54}$$

$$\overrightarrow{V_L^*} = \overrightarrow{V_m^*} - \frac{\Delta \overrightarrow{V^*}}{2} \tag{3.55}$$

where $\overrightarrow{V_m^*}$ represents the mean velocity which does not recognize the presence of the local vorticity, $\Delta \overrightarrow{V^*}$ denotes the jump in the tangential flow velocity across the vortex sheet.

Using Equations (3.54) and (3.55), we have

$$\vec{V_U^*} \cdot \vec{V_U^*} - \vec{V_L^*} \cdot \vec{V_L^*} = \left(\vec{V_U^*} + \vec{V_L^*}\right) \cdot \left(\vec{V_U^*} - \vec{V_L^*}\right) \tag{3.56}$$

$$= 2\vec{V_m^*} \cdot \Delta\vec{V^*}$$

Evaluation of $\vec{V_m^*}$ and $\Delta\vec{V^*}$

The mean velocity $\vec{V_m^*}$ is found by adding all the nondimensional velocities at the control point associated with the bound vortices and the wake vortices through the Biot-Savart law and the free stream velocity.

The jump in the tangential component of the flow velocity across a vortex sheet is equal to the strength of the sheet. Consider a typical element of the aerodynamic mesh shown in Figure 3-11. We define the vector $\vec{\Gamma^*}$ as

$$\vec{\Gamma^*} = \frac{1}{2}\left(\Gamma_1^* \vec{L_1^*} + \Gamma_2^* \vec{L_2^*} + \Gamma_3^* \vec{L_3^*} + \Gamma_4^* \vec{L_4^*}\right) \tag{3.57}$$

where Γ_1^*, Γ_2^*, Γ_3^*, and Γ_4^* are the nondimensional circulation strengths along the four segments of the element, respectively, and

$$\vec{L_1^*} = \frac{\vec{DA}}{L_C}, \quad \vec{L_2^*} = \frac{\vec{AB}}{L_C} \tag{3.58}$$

$$\vec{L_3^*} = \frac{\vec{DC}}{L_C}, \quad \vec{L_4^*} = \frac{\vec{CB}}{L_C} \tag{3.59}$$

The nondimensional area of the element can be approximated as

$$Area^* = \frac{1}{2}\left|\vec{L_1^*} \times \vec{L_3^*}\right| + \frac{1}{2}\left|\vec{L_2^*} \times \vec{L_4^*}\right| \tag{3.60}$$

Then

$$\Delta\vec{V^*} = -\frac{\vec{n} \times \vec{\Gamma^*}}{Area^*} \tag{3.61}$$

Evaluation of $\left(\frac{\partial \Phi^*}{\partial t^*} \big|_U - \frac{\partial \Phi^*}{\partial t^*} \big|_L \right)$

To evaluate $\left(\frac{\partial \Phi^*}{\partial t^*} \big|_U - \frac{\partial \Phi^*}{\partial t^*} \big|_L \right)$, we first consider the time derivative of the velocity potential Φ, $\frac{\partial \Phi}{\partial t}$. By definition,

$$\frac{\partial \Phi\left(\overrightarrow{r}, t\right)}{\partial t} = \lim_{\Delta t \to 0} \frac{\Phi\left(\overrightarrow{r}, t + \Delta t\right) - \Phi\left(\overrightarrow{r}, t\right)}{\Delta t} \tag{3.62}$$

where $\overrightarrow{r}$ is a position vector in the inertial coordinate system. It is difficult to evaluate $\frac{\partial \Phi\left(\overrightarrow{r}, t\right)}{\partial t}$ directly, because, in our application, the velocity potential is easily described in the wing or body fixed coordinate system. We approximately evaluate $\frac{\partial \Phi\left(\overrightarrow{r}, t\right)}{\partial t}$ as follows.

As shown in Figure 3-12, at time t, one control point denoted by Point P is located at position $\overrightarrow{r}\,(t)$, and at time $t + \Delta t$ it moves to Point P' with position vector $\overrightarrow{r}\,(t + \Delta t)$. The distance between P and P' is $\Delta \overrightarrow{r}$, i.e.,

$$\Delta \overrightarrow{r} = \overrightarrow{r}\,(t + \Delta t) - \overrightarrow{r}\,(t) \tag{3.63}$$

Using a Taylor series expansion, we have

$$\Phi\left(\overrightarrow{r} + \Delta \overrightarrow{r}, t + \Delta t\right) = \Phi\left(\overrightarrow{r}, t + \Delta t\right) + \nabla \Phi\left(\overrightarrow{r}, t + \Delta t\right) \cdot \Delta \overrightarrow{r} + \cdots \tag{3.64}$$

$$\Phi\left(\overrightarrow{r}, t + \Delta t\right) \approx \Phi\left(\overrightarrow{r} + \Delta \overrightarrow{r}, t + \Delta t\right) - \nabla \Phi\left(\overrightarrow{r}, t + \Delta t\right) \cdot \Delta \overrightarrow{r} \tag{3.65}$$

We rewrite 3.62 as

$$\begin{aligned}
\frac{\partial \Phi\left(\overrightarrow{r}, t\right)}{\partial t} &= \lim_{\Delta t \to 0} \frac{\Phi\left(\overrightarrow{r} + \Delta \overrightarrow{r}, t + \Delta t\right) - \Phi\left(\overrightarrow{r}, t\right) - \nabla \Phi\left(\overrightarrow{r}, t + \Delta t\right) \cdot \Delta \overrightarrow{r}}{\Delta t} \\
&= \lim_{\Delta t \to 0} \frac{\Phi\left(\overrightarrow{r} + \Delta \overrightarrow{r}, t + \Delta t\right) - \Phi\left(\overrightarrow{r}, t\right)}{\Delta t} - \lim_{\Delta t \to 0} \nabla \Phi\left(\overrightarrow{r}, t + \Delta t\right) \cdot \frac{\Delta \overrightarrow{r}}{\Delta t}
\end{aligned} \tag{3.66}$$

It is clear that $\lim_{\Delta t \to 0} \frac{\Delta \overrightarrow{r}}{\Delta t}$ gives the body velocity of Point P fixed at the vortex

lattice $\overrightarrow{V_{BP}}$. Thus

$$
\begin{aligned}
\frac{\partial \Phi\left(\overrightarrow{r}, t\right)}{\partial t} &= \lim_{\Delta t \to 0} \frac{\Phi\left(\overrightarrow{r} + \Delta \overrightarrow{r}, t + \Delta t\right) - \Phi\left(\overrightarrow{r}, t\right)}{\Delta t} - \nabla \Phi\left(\overrightarrow{r}, t\right) \cdot \overrightarrow{V_{BP}} \quad (3.67) \\
&= \frac{\text{Ð}\Phi}{\text{Ð}t}|_P - \nabla \Phi\left(\overrightarrow{r}, t\right) \cdot \overrightarrow{V_{BP}}
\end{aligned}
$$

where $\frac{\text{Ð}\Phi}{\text{Ð}t}$ is the "substantial derivative" of $\Phi\left(\overrightarrow{r}, t\right)$ following a point fixed to the moving lattice (but not a fluid particle as in the usual use of this term). With the previously defined characteristic variables, it is easy to nondimensionalize Equation (3.67):

$$
\frac{\partial\left(\Phi^* V_C L_C\right)}{\partial\left(t^* T_C\right)} = \frac{\text{Ð}\left(\Phi^* V_C L_C\right)}{\text{Ð}\left(t^* T_C\right)} - \frac{1}{L_C} \nabla^*\left(\Phi^* V_C L_C\right) \cdot \left(V_C \overrightarrow{V_{BP}^*}\right)
$$

$$
\begin{aligned}
\frac{\partial \Phi^*}{\partial t^*} &= \frac{\text{Ð}\Phi^*}{\text{Ð}t^*} - \frac{T_C}{V_C L_C} V_C^2 \, \nabla^*\left(\Phi^*\right) \cdot \overrightarrow{V_{BP}^*} \quad (3.68) \\
&= \frac{\text{Ð}\Phi^*}{\text{Ð}t^*} - \nabla^*\left(\Phi^*\right) \cdot \overrightarrow{V_{BP}^*}
\end{aligned}
$$

Now we can make use of Equation (3.68) to compute $\left(\frac{\partial \Phi^*}{\partial t^*}|_U - \frac{\partial \Phi^*}{\partial t^*}|_L\right)$ as follows:

$$
\frac{\partial \Phi^*}{\partial t^*}|_U - \frac{\partial \Phi^*}{\partial t^*}|_L = \frac{\text{Ð}}{\text{Ð}t^*}\left[\Phi^*\left(\overrightarrow{r_U}, t\right) - \Phi^*\left(\overrightarrow{r_L}, t\right)\right] - \left[\nabla^*\left(\Phi^*\left(\overrightarrow{r_U}, t\right)\right) - \nabla^*\left(\Phi^*\left(\overrightarrow{r_L}, t\right)\right)\right] \cdot \overrightarrow{V_{BP}^*}
$$

$$(3.69)$$

but

$$
\nabla^*\left(\Phi^*\left(\overrightarrow{r_U}, t\right)\right) = \overrightarrow{V_U^*} = \overrightarrow{V_m^*} + \frac{\Delta \overrightarrow{V^*}}{2} \quad (3.70)
$$

$$
\nabla^*\left(\Phi^*\left(\overrightarrow{r_L}, t\right)\right) = \overrightarrow{V_L^*} = \overrightarrow{V_m^*} - \frac{\Delta \overrightarrow{V^*}}{2} \quad (3.71)
$$

so that

$$
\nabla^*\left(\Phi^*\left(\overrightarrow{r_U}, t\right)\right) - \nabla^*\left(\Phi^*\left(\overrightarrow{r_L}, t\right)\right) = \Delta \overrightarrow{V^*} \quad (3.72)
$$

Moreover, it follows from Figure 3-12 that $\Phi^*\left(\overrightarrow{r_U}, t\right) - \Phi^*\left(\overrightarrow{r_L}, t\right)$ can be computed as

$$
\Phi^*\left(\overrightarrow{r_U}, t\right) - \Phi^*\left(\overrightarrow{r_L}, t\right) = \oint_{C(t)} \overrightarrow{V_F^*} \cdot d\overrightarrow{r^*} = \Gamma^*\left(t\right) \quad (3.73)
$$

61

where $C(t)$ is a path that goes from the point on the lower side of the vortex sheet around the leading edge to the same point on the upper side of the surface, and shown as the dotted line in the figure. It follows from Stokes' theorem that $\Gamma^*(t)$ has the same value as the circulation $G^*(t)$ for the loop that encloses the control point. Take control point i as an example, the "substantial" derivative $\frac{\mathrm{D}G_i^*}{\mathrm{D}t^*}$ is approximated by a first order finite-difference:

$$\frac{\mathrm{D}G_i^*(t)}{\mathrm{D}t^*} = \frac{G_i^*(t) - G_i^*(t - \Delta t)}{\Delta t} \tag{3.74}$$

After calculating ΔC_p, we can express the aerodynamic load vector $\left\{F_a^{CP}\right\}$ in terms of all the element force vectors at the control points:

$$\left\{F_a^{CP}\right\} = \frac{1}{2}\rho V_C^2 L_C^2 \left\{ \begin{array}{c} \Delta C_{p1}\left(A_1^*\right)^2 \overrightarrow{n_1} \\ \Delta C_{p2}\left(A_2^*\right)^2 \overrightarrow{n_2} \\ \vdots \\ \Delta C_{pn}\left(A_n^*\right)^2 \overrightarrow{n_N} \end{array} \right\} \tag{3.75}$$

where ΔC_{pi}, A_i^*, $\overrightarrow{n_i}$ $(i = 1, 2, \cdots N)$ are the differential pressure coefficients, the nondimensional element areas, and the unit normal vectors at control points, respectively, and N is the total number of control points.

3.1.8 Programming Concerns

As we have mentioned earlier, one challenge in the unsteady vortex-lattice method is that we have to provide the line of flow separation, from which the vorticity is shed to form the wake. For a one-wing configuration, we could provide the number of the row or the column of the aerodynamic grid where the trailing edge and the wing tip are located, by which the line of separation is provided. However, for compound configurations, e.g., formation flight, or the cases when control surfaces such as flaps or ailerons are considered, multiple separation lines exist; it can be difficult or very tedious to provide the information for separation lines. We need find a way to address this problem.

On the other hand, the flow field sometimes can be treated to be symmetric about

the mid-span plane, and it saves computing time to take advantage of this symmetry, while sometimes this symmetry does not exist. One example without this symmetry is when we take into account the rolling motion of the aircraft. We want that the program could handle both situations. In addition, as we know, there are a lot of commercial software that can be used to generate finite element meshes, such as MSC/PATRAN and ANSYS. It will be very helpful if we can take advantage of these software to generate the aerodynamic grid. To facilitate the use of these software, we utilize a location connection matrix or array to connect the node number with the element number, which is similar to the finite-element method. We call this location connection array LM, which has the dimension of $6 \times NP$, where NP is the total number of elements in the aerodynamic grid. LM also includes extra information such as that for symmetry. $LM\,(1:4,\ j)$ for $j = 1, 2, \cdots, NP$ gives the number of the four nodes for each element. $LM\,(5,\ j)$ for $j = 1, 2, \cdots, NP$ determines if there is any symmetry about the mid-span plane. If $LM\,(5,\ j) = 0$, there is no symmetry considered. If $LM\,(5,\ j) = 1$, a mirror image of the element with respect to the mid-span plane is considered. $LM\,(6,\ j)$ for $j = 1, 2, \cdots, NP$ determines if the element belongs to the lifting surface or a non-lifting surface (for example, the fuselage). If $LM\,(6,\ j) = 0$, it means that the element belongs to a non-lifting surface. If $LM\,(6,\ j) = 1$, the element is on the lifting surface. The difference between lifting surfaces and non-lifting surface lies in how to calculate the partial time derivative of the velocity potential Φ. For the lifting surface, this derivative is calculated according to Equation (3.67), while for non-lifting surfaces, it is assumed to be zero.

We still take the aerodynamic grid shown in Figure 3-8 as an example. For the first element, $LM\,(i,\ 1)$ for $i = 1, 2, \cdots, 6$ would be 1, 2, 7, 6, 1, and 1 respectively. Note that the node number is given clockwise. For the last element, $LM\,(i,\ 12)$ for $i = 1, 2, \cdots, 6$ would be 14, 15, 20, 19, 1, and 1 respectively.

As for the information for separation lines, instead of providing the number of the row or column of the grid, we give the information for the segments so that it is easy to provide such information for any situation, either single-wing configurations or multi-

wing configurations. Recalling from the previous discussion about the shedding and convecting of the wake that the wake elements adjacent to the bound vortex sheet have the same circulations as their adjoining bound vortex elements, and that there is a slight difference between the first corner wake element and the other wake elements, we use two variables $NCWAKEC$ and $NCWAKE$ to denote the number of the corner wake elements and the number of wake elements other than the corner wake elements at time $t = \Delta t$, respectively. In other words, $NCWAKEC$ and $NCWAKE$ represent the number of columns of the wake. Two arrays, $IPWAKEC$ and $INWAKEC$, for the corner wake, are used to provide the adjoining bound vortex element number and the corresponding node number of the segments. $IPWAKEC$ and $INWAKEC$ have a dimension of $NCWAKEC$ and $3 \times NCWAKEC$, respectively. Similarly, two arrays, $IPWAKE$ and $INWAKE$, are used to provide the adjoining bound vortex element number and the corresponding node number of the segments for the wake elements other than the corner wake. $IPWAKE$ and $INWAKE$ have a dimension of $NCWAKE$ and $2 \times NCWAKEC$, respectively.

For our simple example, $NCWAKEC = 1$ and $NCWAKE = 5$. The arrays for the wake are as follows:

$IPWAKEC(1) = 12$. $INWAKEC(i, 1)$ for $i = 1, 2, 3$ would be 19, 15, and 20. The corner node is listed as the third array element. $IPWAKE(i)$ for $i = 1, 2, \cdots NCWAKE$ are 9, 10, 11, 8, and 4. $INWAKE(i, 1)$ for $i = 1, 2$ are 16 and 17; $INWAKE(i, 2)$ for $i = 1, 2$ are 17 and 18; $INWAKE(i, 3)$ for $i = 1, 2$ are 18 and 19; $INWAKE(i, 4)$ for $i = 1, 2$ are 15 and 10; $INWAKE(i, 5)$ for $i = 1, 2$ are 10 and 5.

When we begin to shed vorticity, we only need to calculate the local fluid particle velocities at the nodes 16, 17, 18, 19, 15, 10, and 5. Since those node numbers are repeated in the arrays $INWAKEC$ and $INWAKE$. We could sort the repeated node number out by searching through the arrays $INWAKEC$ and $INWAKE$ before shedding and convecting the wake to avoid redundancy of computing the velocity. This only needs to be done once in the program. The new positions related to the nodes 16, 17, 18, 19, 15, 10, and 5 and their consequent nodes (such as Nodes 16', 17', 18', 19', 15', 10', and

5' in Figure 3-9) during the shedding and convecting process are mapped onto the wake through the information provided by the arrays $IPWAKEC$, $INWAKEC$, $IPWAKE$, and $INWAKE$.

Another important characteristic of the programming is the use of OpenMP directives for parallel processing. OpenMP is a specification for a set of compiler directives, library routines, and environment variables that can be used to specify shared memory parallelism in Fortran or C/C++ programs. The directive sentinels are structured so that the directives are treated as Fortran comments unless a command line option, which activates and allows interpretation of all OpenMP compiler directives, is used when compiling the code. The detailed information can be found at the web site: http://www.openmp.org. By using the OpenMP directives, we could run the simulation code written in Fortran 90 simultaneously on multiple processors, which significantly reduces the running time.

3.2   Numerical Examples

In order to justify the use of UVLM to simulate the flow around bodies, several examples are analyzed first, and numerical and experimental results from the literature are compared. Then several applications are analyzed.

3.2.1   Flow past a Spherically Blunted Cylinder-Cone Configuration

The first example considers a closed three-dimensional body of revolution. The body is a cone-cylinder having a semi-vertex angle of 15°, which has been blunted by a spherical cap whose radius is equal to one half the radius of the cylindrical afterbody. This body and the numerical grid are shown in Figure 3-13. Johnson (1963) compared pressure distributions computed by a source-based numerical simulation with experimental data for the cone-cylinder at zero angle of attack and at ±20° angle of attack. The pressure distributions along the top of the body obtained by UVLM and Johnson's experimental

data are compared in Figure 3-14, where the pressure coefficient C_p is defined as

$$C_p = \frac{Pressure}{\frac{1}{2}\rho_\infty V_\infty^2} \qquad (3.76)$$

The agreement is very good over the nose section of the body and a little less satisfactory over the afterbody. The reason for the less satisfactory on the afterbody is because the numerical solution actually corresponds to an infinite long afterbody. On the forward portion of the afterbody, the effect of flow separation around the sharp shoulder is important; while on the aft portion of the afterbody, the effect of the finite length of the body becomes important.

3.2.2 Flow past a Mid-Wing/Single-Fuselage Configuration

The configuration being analyzed in this section is shown in Figure 3-15. The fuselage is an ellipsoid of revolution whose axes are in the ratio of 1:7. The planform of the wing is rectangular, the aspect ratio is five, and the cross section is a NACA 23012 profile. We do not model the thickness of the wing; instead, we place the vortex lattice on its camber surface. We fully account for the aerodynamic interference between the wing and fuselage in the numerical simulation.

The aerodynamic coefficients of the major components of the airplane — wing and fuselage — are quite well established through theory and systematic measurements. However, when these individual parts are assembled into a complete airplane, their interaction (interference) may play an important role in the formation of aerodynamic forces. The physical processes behind the aerodynamics of the interaction are harder to conceive than those of the aerodynamics of the individual parts. In the present method (UVLM), the interaction between the wing and fuselages are simulated by the mutual influence of their bound vortex sheets, and the interaction of their individual wakes, i.e., the wakes deform freely under their interaction.

It is advantageous and generally customary to express the aerodynamic forces in terms of dimensionless coefficients, such as the coefficients of lift, drag, and pitching moment.

In this dissertation, the coefficient of lift is of great interest, which is defined as follows:

$$C_L = \frac{Lift}{\frac{1}{2}\rho_\infty V_\infty^2 S_{ref}} \qquad (3.77)$$

where, ρ_∞ is the flow mass density, V_∞ is characteristic velocity (here, free stream velocity), S_{ref} is the reference area. Usually the reference area is selected to be the plan area of the wing. When the aerodynamic coefficients are applied to the wing-fuselage system, it is better to use the same reference area as that for the original wing (wing-alone) because a different reference area will change not only the values of the coefficients but also the slope of the line of aerodynamic coefficients vs. angle of attack.

The experimental results for the fuselage-wing system show that, "In the range of moderate angles of attack, the fuselage does not noticeably affect the trend of curve. The coefficient of maximum lift, however, is markedly reduced by the fuselage" (Schlicting and Trukenbodt (1979)). The numerical solution for this configuration cannot predict the maximum lift, but below the maximum, the present numerical simulation reached the same conclusion. The comparison is shown in Figure 3-16. The angle of attack is measured with respect to the chord line of the wing. If not explicitly mentioned otherwise, the same definition for the angle of attack is used. From the figure, we can see that the numerical solution is very close to the experimental results for angles of attack below ten degrees.

3.2.3 Flow past Rectangular Wings

Lift Coefficients for Wings with NACA 23012 Airfoil

In this section, rectangular wings with various aspect ratios, 1, 1.7, 2, 3, 5, 10, and 20 are analyzed, and the two-dimensional problem that corresponds to a wing with an infinite aspect ratio is calculated as well. The cross section of the wings is NACA 23012 profile. The lifting surface formed by the camber lines is used to represent the wing and is replaced by the aerodynamic grid. Figure 3-17 presents the lift coefficient as a function of the angle of attack for various aspect ratios. It is clear that, as the aspect

ratio increases, so do the lift coefficient and the lift curve slope. We plot the lift curve slope vs. the aspect ratio in Figure 3-18. It is expected that the lift curve slope would approach the two-dimensional value as the aspect ratio approaches infinity, so that the two-dimensional value is plotted as the dotted horizontal line in the figure.

In Figures 3-19, 3-20 and 3-21, the lift coefficient is plotted as a function of the aspect ratio at angles of attack of, 0 deg., 3 deg., and 5 deg., respectively. The experimental data (Miley (1982)) for the two-dimensional case is given as a range in the figures, because the experiments were conducted at different wind-tunnels and various experimental conditions. Some of the ranges are pretty large, for example, the one at 0 deg. angle of attack. The numerical two-dimensional solutions of the lift coefficient fall in between the experimental range, and the trends of the lift coefficients are consistent with the experimental, i.e., the numerical lift coefficient asymptotically reaches the two-dimensional value.

Span-wise Distribution of Normal Force along A Flat Plate

The normal force distribution along the span of a flat plate is investigated. The plate has an aspect ratio of 1. The local or sectional normal force coefficient is defined as

$$C_n = \frac{1}{c\left(y\right)} \int\limits_0^{c(y)} \Delta C_p\left(x\right) dx \qquad (3.78)$$

where $c\left(y\right)$ is the local chord length of the wing at location y. For small angles of attack, the local normal force coefficient can be set equal to the local lift coefficient C_l:

$$C_l = \frac{1}{\frac{1}{2}\rho_\infty V_\infty^2 c\left(y\right)} \frac{dL}{dy} \qquad (3.79)$$

where L is the lift force. Note that, to distinguish between the coefficients of the total forces, the indices of which are always expressed in capital letters, lower case letters are used for the indices of the coefficients of local or sectional forces.

The numerical solutions of the normal force span-wise distribution at angles of attack

of, 9.7 deg. and 19.4 deg. are presented in Figure 3-22. Also shown in the figure are the experimental results obtained by Scholz (1949). As we can see from the figure, the numerical solution is in good agreement with the experimental results. Both numerical solutions and experimental results observe a slight hump or rise in the local normal force near the wing tip. This hump is the result of the wing-tip vortex system rising above the wing.

3.2.4   An Inboard-Wing/Twin-Fuselage Configuration

One application to which we apply our UVLM is an innovative inboard-wing/twin-fuselage configuration.

The aviation industry has been urged to develop faster and/or bigger airplanes and to fly them closer together as part of a large effort to meet the needs of an ever-increasing air transportation system. One of the ideas for a large airplane comes from the NASA Langley Research Center. Spearman and Feigh (1998) suggested a configuration that differs from a conventional wing-body-tail design. Instead of one fuselage located in the center of the configuration, twin fuselages are placed at the tips of an inboard wing. The intent is "to provide an increase in payload capacity without an increase in overall length and width when compared to current designs and to achieve two-dimensional flow on the wing by eliminating free wing tips so that the wing tip flow that produces an induced drag and a hazardous trailing vortex would not exist.

One aerodynamic model has been tested in Virginia Tech's Stability Wind tunnel to study this inboard-wing, twin-fuselage concept (Orr, *et al.* (2001) and Magill (2000)). The configuration is represented schematically in Figure 3-23. The wing airfoil is NACA 23012, and tail airfoils are NACA 0012. We will present the numerical solutions by UVLM and some experimental data as well as the comparisons between them. The work has been published in Wang *et al.* (2001).

The grid for this configuration is shown in Figure 3-24. The total number of elements used varies from 450 in the wing alone to 2300 in the wing-body combination to 2636 for the complete wing-body-tail configuration. When the flow is considered to be symmetric

as it is here, the number of elements is one half of these values.

In Figure 3-25, the experimental results of Spearman and Feigh (1998) and numerical results with UVLM are shown, giving C_L (the lift coefficient) as a function of the angle of attack α for the wing alone and for the wing-body combinations. The span of the wing alone extends from the centerline of one fuselage to the centerline of the other; thus, the addition of the fuselages makes the span of the combination greater than the span of the wing alone by one fuselage diameter. For these results, the aspect ratio of the wing alone is 1.7. If the wing alone had had the same span as the combination, its aspect ratio would have been 2. All of the coefficients represented in this figure are based on the span of the wing alone with an aspect ratio of 1.7. The numerical results obtained from UVLM are lower than the experimental results; the trends, however, are somewhat similar. We expect the lift for the combination to be higher than that for the wing alone because the addition of the fuselages has increased the span of the configuration. We do not have a ready explanation for why the trend is reversed in the experimental data below 2.5 degrees, nor do we have an explanation for the disagreement between the two sets of results, except the reference for the angle of attack may have been different.

In Figure 3-26, the experimental results obtained at Virginia Tech are compared with the numerical results obtained with UVLM. Here the aspect ratio of the wing alone is two, and, unlike the model used for the Figure 3-25, the addition of the two fuselages did not make the span of the combination larger than the span of the wing alone. The wing-body combination was the same as that used to obtain the results in Figure 3-25, but the wing alone had an aspect ratio of two instead of 1.7. All of the coefficients here are based on an aspect ratio of two. The numerical results for the wing alone were obtained with PMARC as well as UVLM. The results obtained with UVLM agree with the experimental results at low angles of attack, but over-predict the lift for high angles of attack.

A possible explanation for the difference at high angles of attack is that UVLM accounts for the wing-tip vortex system, and the version of PMARC that was used does not. At high angles of attack on wings of small aspect ratio, the wing-tip vortex systems

noticeably raise the lift above the predictions of aerodynamic models that do not take them into account. If the flow is starting to separate near the trailing edge of the wing when the angle of attack exceeds five degrees, the accompanying loss of lift could be about equal to the gain produced by the wing-tip vortex system, and the two effects would more or less cancel.

For this case in which the span of the configuration is the same as the span of the wing alone, the lift predicted by UVLM is substantially below the experimentally obtained lift although the slopes of experimental and numerical results for the combination are nearly the same. When the lift for the wing-body combination in Figure 3-26 is adjusted to conform with a reference area based on a wing of aspect ratio 1.7, as in Figure 3-25, then we see that the lift observed in the Virginia Tech tunnel is substantially higher than what Spearman and Feigh observed in their experiment. After many checks and reviews, we have no explanation for this difference.

In Figure 3-27, the experimental results of Spearman and Feigh (1998) and the numerical results obtained with UVLM are shown for various wing-body-tail combinations. Again the results are based on an aspect ratio of 1.7. In the legend, **WB** denotes the wing-body combination only, **WBV** denotes the wing-body combination with vertical tails, and **WBVH** denotes the wing-body combination with vertical tails and a horizontal stabilizer mounted at the top of the vertical tails. As before, the numerical results under-predict the lift. The experimental results show that the lift of the wing-body combination decrease slightly when the vertical tails are added and then increases noticeably above its original value when the horizontal tail is added. This is the lift on the entire configuration, which includes the horizontal tail. The numerical results predict that the vertical tails have practically no effect on the lift and the horizontal tail raises it slightly.

In Figure 3-28, the flowfield predicted by UVLM is represented with plots of the vortex lattices containing the vorticity in the wake. In part (a), the wake lattice is plotted for the wing alone; in part (b), it is plotted for the wing-body combination. Figure 3-29 shows the calculated wake for the full configuration — wing, body, vertical tails and horizontal stabilizer. To obtain these results, we had to assume a separation line near

the tail ends of the fuselages. We used several circles with their centers on the axis of the fuselage, and found that the lift was not sensitive to our choice. The wake shed from these artificially chosen separation lines is essentially the wing-tip vortex, and the figures clearly show the wake rolling up similar to the wake for the wing alone.

In figure 3-30, the computed flow in a Trefftz plane at the mid-chord position clearly shows a pattern consistent with the presence of streamwise vorticity, which is in the lattice that represents the boundary layer on the fuselage. The effect of this vortical flow is to produce a significant downwash on the wing near the fuselage, which in turn has a negative influence on the spanwise distribution of lift. The computed flow in a Trefftz plane four chord-lengths behind the configuration is shown Figure 3-31. The numerically predicted strong vortical flow in the wake is not consistent with the observations of Spearman and Feigh (1998), but it is qualitatively consistent with the observations made in the wind tunnel at Virginia Tech.

3.2.5   Formation Flights

There is renewed interest in studying close-formation flying (see Wagner *et al.* (2001), Gingras *et al.* (2001), and Blake *et al.* (2001)). The benefits of flying in close formation arise from the disturbance-velocity associated with the vorticity shed primarily from the wing tips. Here we refer to the wing receiving the most benefit as the hitchhiker. When the hitchhiker is in the right position, the disturbance created by the other wing or wings increases the upwash, or the angle of attack, non-uniformly along the span of the hitchhiker. So in order to maintain the lift needed to balance the weight, the angle of attack of the hitchhiker relative to the free stream of the multi-wing configuration must be reduced. This reduction in angle of attack leads to a reduction in the drag, which is the primary benefit to the hitchhiker. The non-uniform distribution of the upwash can result in a roll moment acting on the hitchhiker, and so to balance the moments in these cases, the ailerons must be deflected. Here we assume that the hitchhiker is equipped so that its ailerons may be deflected independently.

To capture the essence of wings flying in close formation, one must be able to model

vorticity-dominated flow fields. As we will show latter, UVLM turns out to be a good candidate for modeling close-formation flights. The work is published in Wang *et al.* (2003*a*).

Two-Wing Case

We represent two wings with identical planar rectangular lifting surfaces of aspect ratio four as shown schematically in Figure 3-32. Both surfaces lie in the same plane and, hence, have the same angle of attack, α, at all times. We chose this configuration for convenience, but as we mentioned above UVLM is not restricted to such simple planforms. We vary α and the gap between the lifting surfaces.

In Figure 3-33, the total lift coefficient, C_L, is plotted as a function of α for several different gaps. The sectional-lift coefficient for the wing on the left-hand side, C_l, is plotted as a function of position along the span for α of one and six degrees in Parts (a) and (b) of Figure 3-34, respectively. From the results in Part (a) it is clear that the total lift, which is proportional to the area under these curves, increases as the gap decreases. The increase is especially strong after the gap is below 0.5 chord, and the maximum lift occurs when then the two wings are joined, which is not surprising because joining the wings doubles the aspect ratio. Comparing the results in Parts (a) and (b), we observe that increasing α increases the total lift as well as the increment derived from formation flying. These conclusions are substantiated by the results shown in Figure 3-33. The lack of symmetry in the lift distributions when the wings fly in close proximity indicates that there is a roll moment about the mid-span axis.

The results for the wing alone show the sectional-lift near the wing tips to be less than that near the center of the span. This is the result of the concentration of vorticity that is very near the wing tip, the so-called wing-tip vortex system, which is associated with a local downwash (decrease in the angle of attack). The wing-tip vortex system is often modeled as actually lying along the wing tip. Although that was not done here, the present results when α is one are in virtually perfect agreement with those obtained by making this simplification. However, that is not the case when α is six degrees. Near

the left wing tip there is a slight hump or rise in the sectional lift, which is the result of the wing-tip vortex system rising above the wing. This hump, which increases with α, is observed in experiments (see, e.g., Schlicting and Truckenbodt (1979)). When the wing-tip vortex is above the wing the associated velocity increases the cross flow across the upper surface and thereby increases the lift in that region. The simplified models do not predict this.

An example of the calculated wakes with the deflected outboard ailerons is represented in Figure 3-35 when α is 4.6 degrees and the gap is 0.125 chord. Here the segments in the vortex lattices that model the wing and its wake are plotted. The calculated cross flows associated with similar vortex segments shown in Figure 3-35, but without aileron deflection, are shown in two Trefftz planes in Figure 3-36. In Part (a) the flow is associated with the combined vorticity shed from the two inboard wing tips, and in Part (b) the flow is associated with the right-hand outboard wing tip. Due to the competing effects of the two wing-tip vortex systems of opposite sign, there appears to be significantly less disturbance in the wake behind the center (where the two wing tips are in close proximity) than behind the outboard wing-tip, where all the vorticity has the same sign. A reduction in the disturbance corresponds to a reduction in the drag, which is discussed below, but not necessarily to a reduction in the lift.

Let us assume that the wings fly at α_0 angle of attack to balance the weight of the aircraft when flying alone. When the two wings fly in close formation, the lift increases and a non-zero roll moment develops, as indicated in Figure 3-34; thus we decrease the angle of attack and deflect only the outboard aileron in order to maintain the lift and, at the same time, reduce the roll moment due to the interference between the two wings to zero. Decreasing the angle of attack leads to a reduction in the induced drag. This process is depicted schematically in Figure 3-37, where F represents the force normal to the wing, which is what the numerical model predicts directly. The component of F perpendicular to the free stream agrees with the experimentally obtained lift. The component parallel to the free stream over-predicts the drag considerably for large aspect ratios, but for small aspect ratios it agrees with experimental data.

We can use the predicted lift to estimate the reduction in drag as follows:

$$\Delta C_D = C_N \sin\left(\alpha_0\right) - C_N' \sin\left(\alpha_0 - \Delta\alpha\right) \tag{3.80}$$

where C_D is the drag coefficient and C_N is the normal-force coefficient defined as follows:

$$C_N = \frac{F}{\frac{1}{2}\rho_\infty V_\infty^2 Area} \tag{3.81}$$

Because the lift C_L does not change,

$$C_L = C_N \cos\left(\alpha_0\right) = C_N' \cos\left(\alpha_0 - \Delta\alpha\right) \tag{3.82}$$

and it follows that

$$\frac{\Delta C_D}{C_N} = \sin\left(\alpha_0\right) - \frac{\cos\left(\alpha_0\right)\sin\left(\alpha_0 - \Delta\alpha\right)}{\cos\left(\alpha_0 - \Delta\alpha\right)} = \sin\left(\alpha_0\right) - \cos\left(\alpha_0\right)\tan\left(\alpha_0 - \Delta\alpha\right) \tag{3.83}$$

then

$$\frac{\Delta C_D}{C_L} = \tan\left(\alpha_0\right) - \tan\left(\alpha_0 - \Delta\alpha\right) \tag{3.84}$$

As an example, we let the $gap = 0.125c$ (chord) and $\alpha_0 = 6\,\text{deg}$. At this angle of attack, $C_L = 0.4$ when each of the wings flies alone, and $C_L = 0.47$ when they fly in formation. For this example, we choose the size of the aileron to be $0.25c \times 0.25s\,(span)$. Using Figure 3-38, we find that by deflecting the aileron $4.5 \sim 4.6\,\text{deg}$. and decreasing the angle of attack to 4.6 deg. We can reduce the roll moment to virtually zero and maintain $C_L = 0.4$. Then it follows that $\frac{\Delta C_D}{C_L} = 0.025$; thus, in this example there is about a 2.5% reduction in the ratio of drag to lift.

Figure 3-38 shows how the deflection of the aileron affects the sectional lift coefficient for the right-hand wing when the angle of attack is $4.6\,\text{deg}$. The lift distributions are not symmetric, and generally the roll moment is zero only when the aileron deflection is about $4.5\,\text{deg}$.

Three-Wing Case

As a second example of formation flights, we consider three wings. Two large wings having the same rectangular planform with an aspect ratio of four are placed apart from each other by one chord length. A small wing one-fourth of the size of the large wings is located above the large wings (see Figure 3-40). We investigated the effects of different heights between the small wing and the two large wings. Because the whole configuration is symmetric about the center xz-plane of the small wing, we only need to analyze one half of the whole configuration by imposing symmetry at the center plane. The calculations were made for all three wings at the same angle of attack, but such a simplification is not necessary.

The small wing benefits from the two large wings, because the upwash from their wing-tip vortex systems essentially increases its angle of attack. However, the increase in the angle of attack varies along the span. The drag reduction, as calculated above, accounts for the nonuniform angle of attack. The results given in Figure 3-41 show how the small wing benefits from its proximity to the larger wings. In Figure 3-41, we see that the closer the small wing flies to the large wings, the greater the increase in its lift. According to our previous discussion, more lift means more reduction in induced drag. In addition, since the influence of the two large wings on the small wing is symmetric, there is no need for the small wing to adjust its ailerons to balance an incurred roll moment as in the previous two-wing case. On the other hand, the small wing has a small influence on the lift distribution of the large wings, and they will require an aileron deflection to balance the roll moments on them.

Docking vs. Formation

In the last example of formation flight, we use a swept wing to represent a typical cargo aircraft and a rectangular wing to represent a hitchhiker aircraft. The sweep angle for the cargo wing is 15 degrees. The rectangular wing has an aspect ratio of four. The swept wing's chord is twice the hitchhiker wing's chord c. Symmetric flows about the xz-plane are considered, which means there are two hitchhiker wings, one flying on each

side of the full swept wing. Four configurations were analyzed: (1) the swept wing and the hitchhiker wing aligned at the leading edge, (2) the swept wing and the hitchhiker wing aligned at the trailing edge, (3) the hitchhiker wing $0.5c$ behind the swept wing, and (4) the hitchhiker wing $2.5c$ behind the swept wing. These configurations were used in a water-tunnel experiment at Virginia Tech. In the experiments the swept wing was mounted at the wall, which essentially has the effect of a mirror on the flow field. The objective of this analysis is to assess the difference in flow field between formation flight and docking flights.

Because 12 deg. angle of attack was used in the water-tunnel experiments, the numerical simulation was conducted at this angle of attack. The numerical solution for the swept wing alone case was analyzed as a reference. Both the calculated wake pattern and the cross flow in a Trefftz plane are presented in Figure 3-42. The Trefftz plane is located four chord lengths of the hitchhiker wing behind the downstream corner at the wing tip of the swept wing. (The same location of Trefftz planes is used for all the other cases.) Due to symmetry, only a half of the whole configuration is shown. Evident in this figure is the twisting of wing tip vortices.

In Figure 3-43, the numerical simulation for the case of the swept wing and hitchhiker wing aligned at leading edge is shown. The vortex lattices in the wake are viewed from the top. The cross flow in a Trefftz plane behind the junction between the swept wing and the hitchhiker is not as strong as that behind the swept wing alone.

Figures 3-44 and 3-45 present the solution for the swept wing and hitchhiker wing aligned at the trailing edge, and the hitchhiker wing 0.5c behind the swept wing. Cross flows were calculated in Trefftz planes for these two cases. The flow field for the case of the hitchhiker wing 2.5c behind the swept wing is similar to that for the case of the hitchhiker wing 0.5c behind the swept wing; it is not shown here. All the calculated results agreed qualitatively with the water-tunnel experiment.

We also give the lift distribution along the span-wise direction for both the swept wing and the hitchhiker wing in Figure 3-46. Either formation flight or docking flight achieves a lift increase for the swept wing and the hitchhiker, compared to when they

fly alone. The hitchhiker wing gets more benefit from docking or formation flight than the swept wing. Among the alignments considered here, the highest gain in lift appears when they dock with their leading edges aligned.
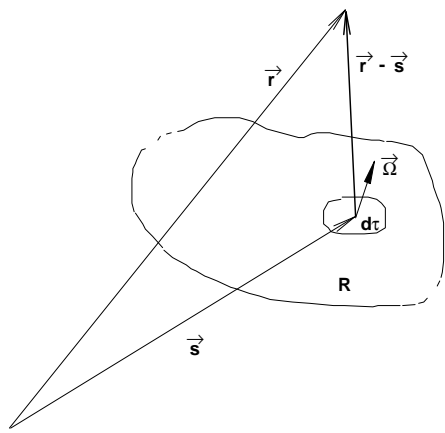
Figure 3-1: Velocity field associated with a vortex distribution
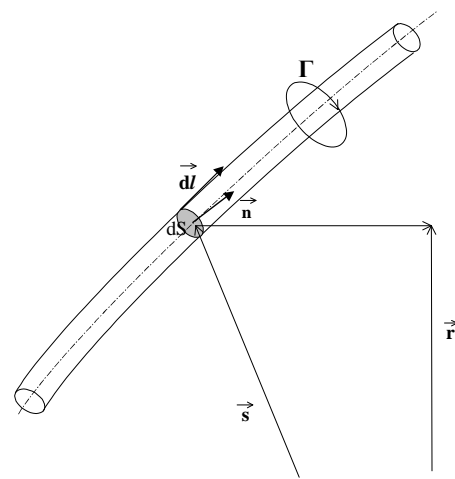
Figure 3-2: Vortex Filament
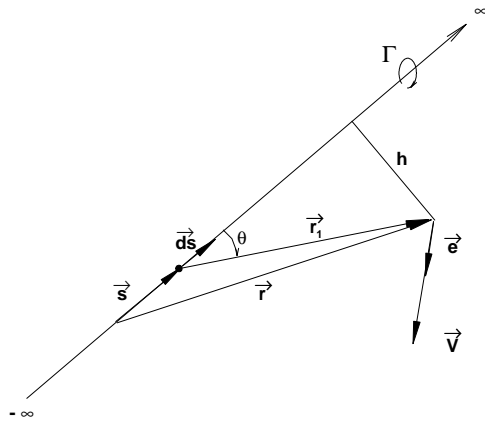
Figure 3-3: Velocity field associated with an infinite straight vortex filament
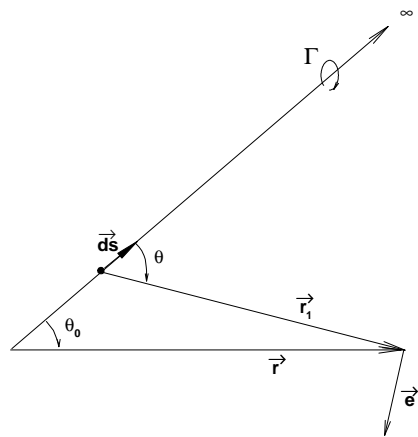
Figure 3-4: Velocity field associated with a semi-infinite straight vortex filament
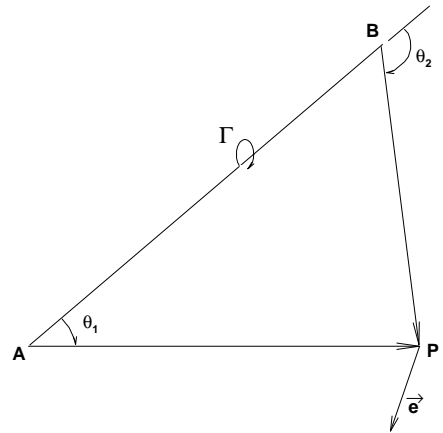
Figure 3-5: Velocity field due to a finite segment of a straight vortex filament
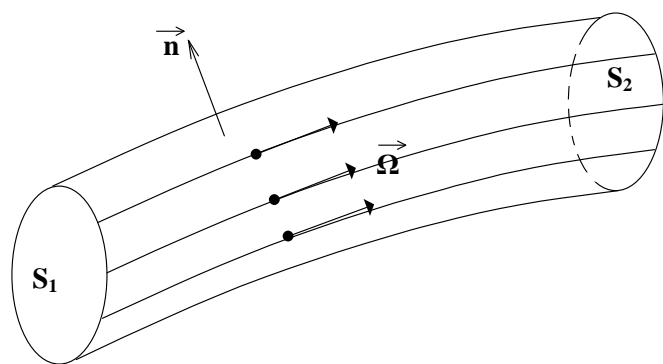
Figure 3-6: Vortex tube
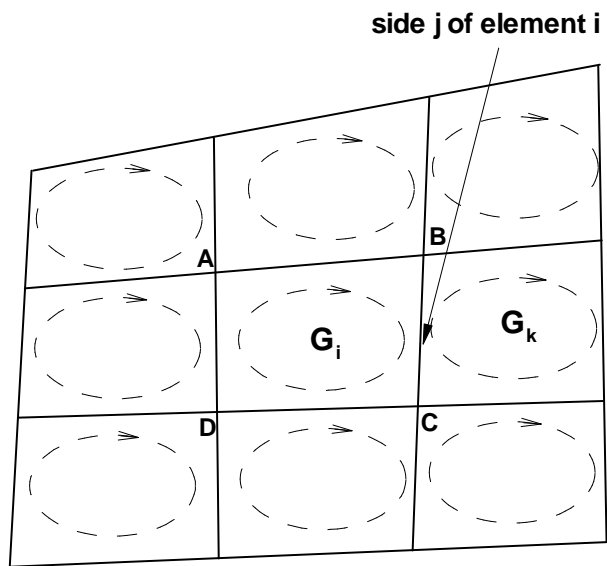
Figure 3-7: Vortex lattice
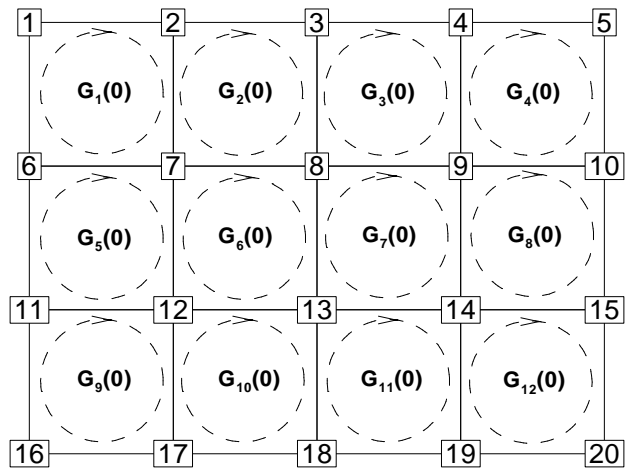
Figure 3-8: A 3×4 vortex lattice of a semi-wing and the soultion at $t = 0$
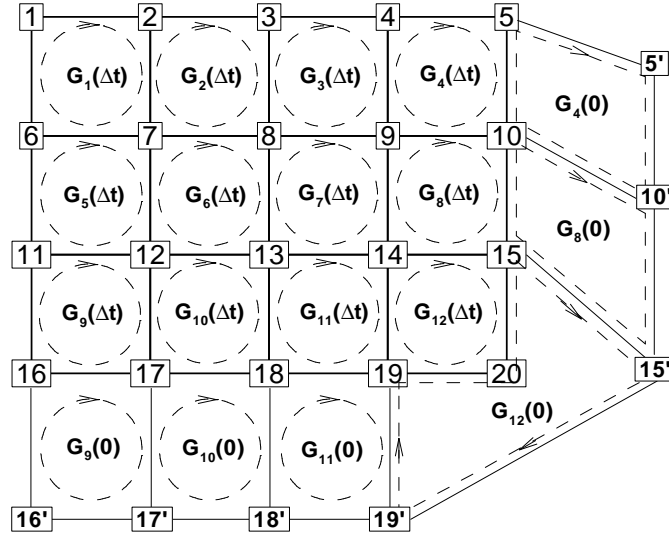
Figure 3-9: The solution for the 3×4 vortex lattice model of the wing at $t = \Delta t$
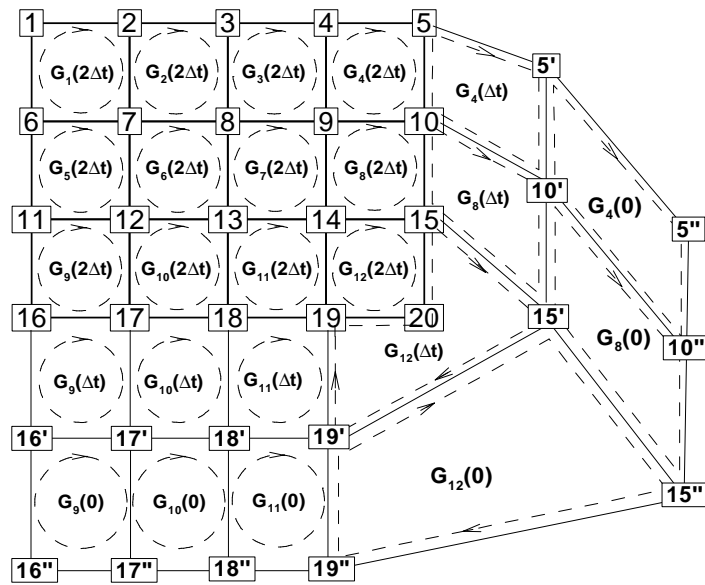
Figure 3-10: The soultion for the 3×4 vortex lattice model of the wing at $t = 2\Delta t$
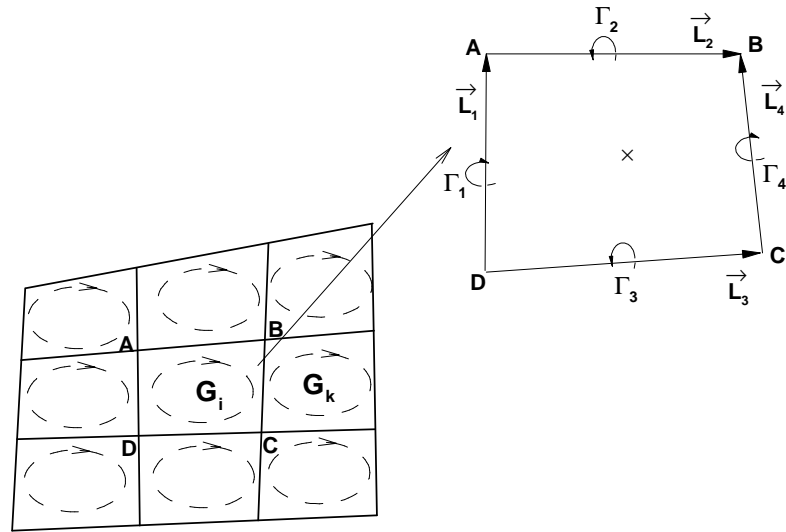
Figure 3-11: A typical vortex element in an aerodynamic grid
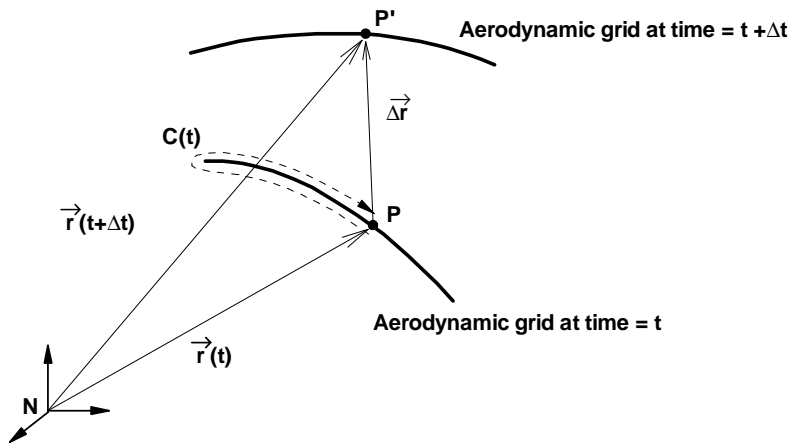
Figure 3-12: Illustration for computing $\frac{\partial \Phi}{\partial t}$
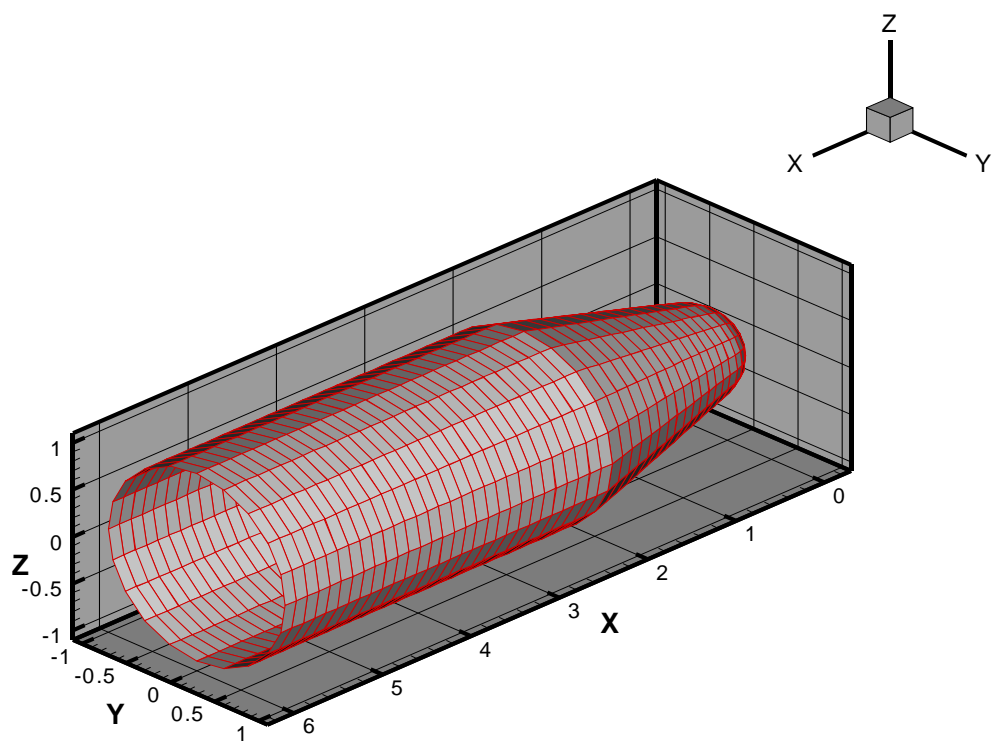
Figure 3-13: The aerodynamic grid of the spherically blunted cylinder-cone configuration
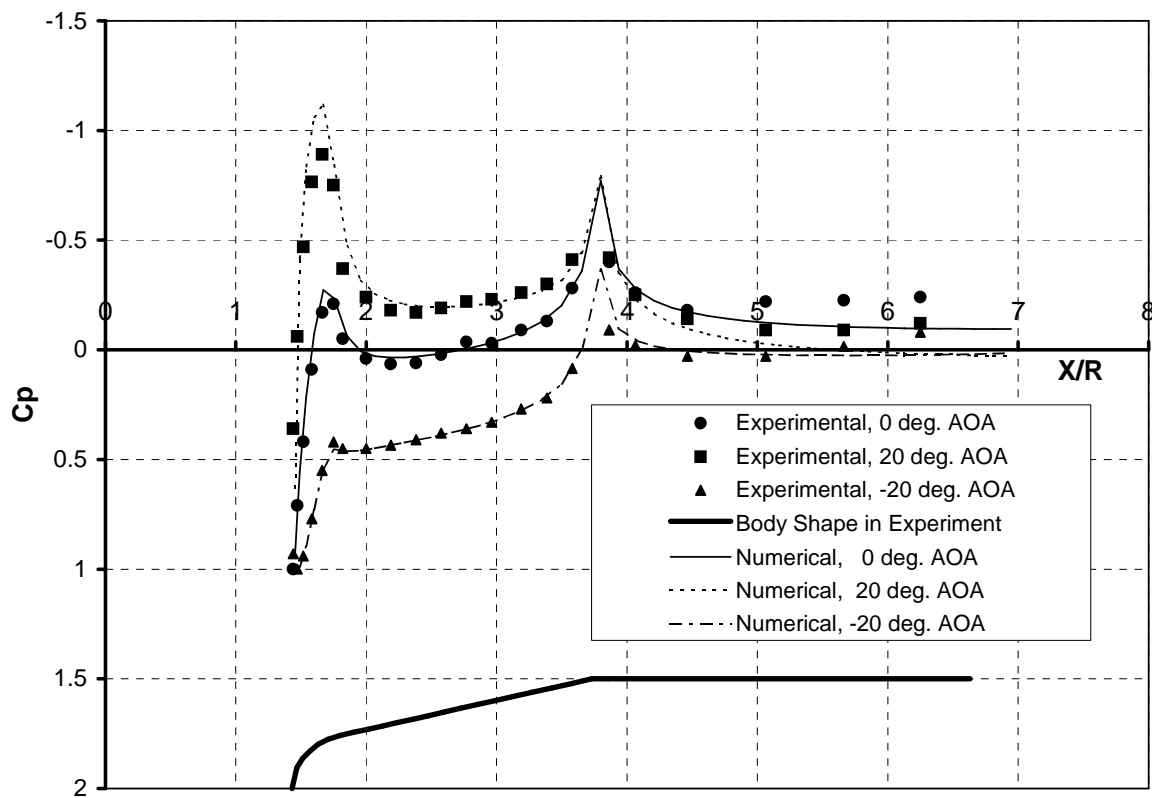
Figure 3-14: Comparison of the calculated and experimental pressure distributions on the blunted cylinder-cone
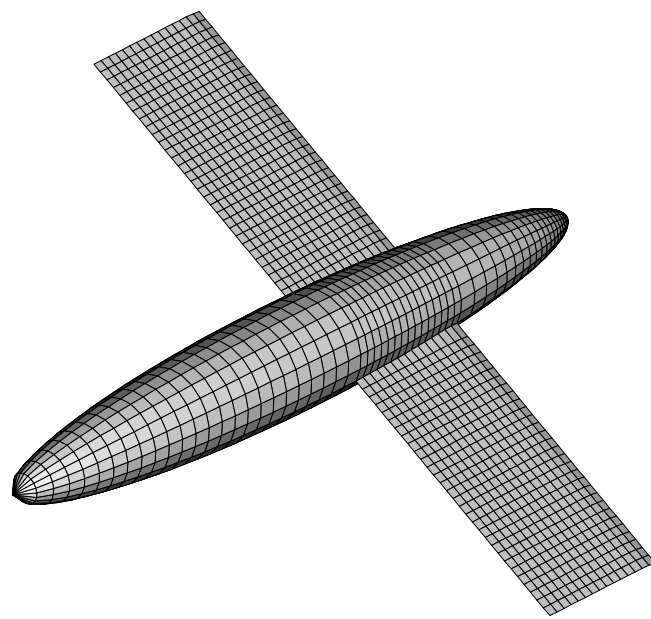
Figure 3-15: The aerodynamic grid of a mid-wing/one-fuselage system
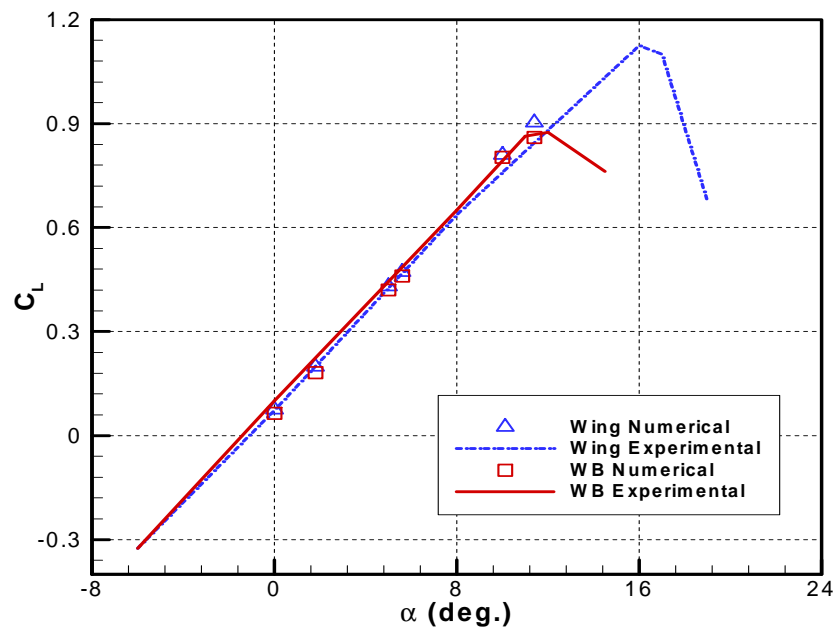
Figure 3-16: Comparison of numerical solutions and experimental results for one fuselage system
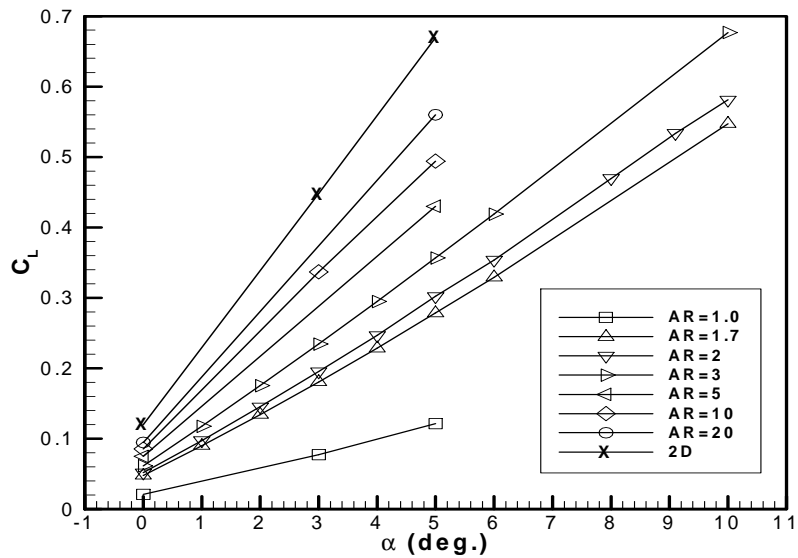
Figure 3-17: The lift coefficient curve for various wing aspect ratios
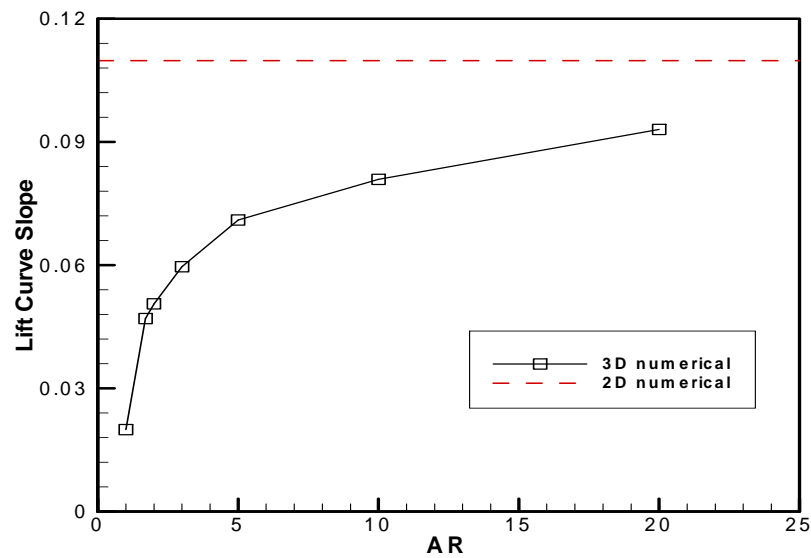
Figure 3-18: The change of lift curve slope with the wing aspect ratio
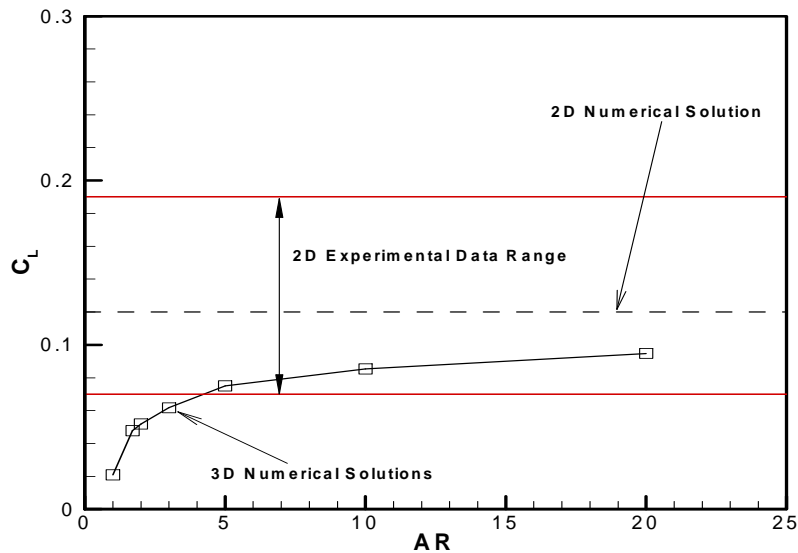
Figure 3-19: The lift coefficients at 0 deg . angle of attack
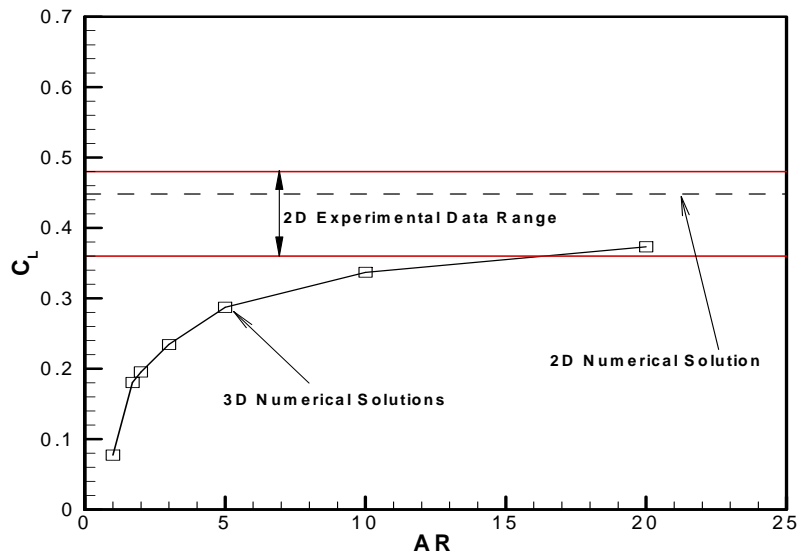
Figure 3-20: The lift coefficients at 3 deg . angle of attack
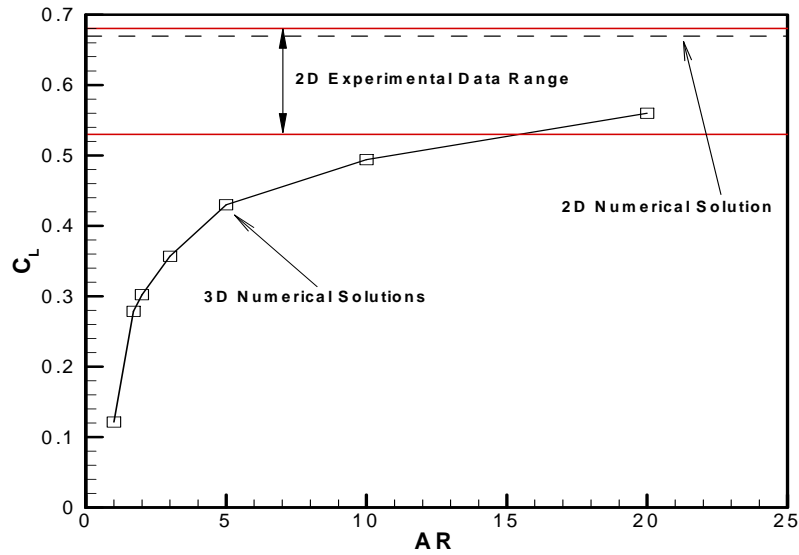
Figure 3-21: The lift coefficients at 5 deg. angle of attack
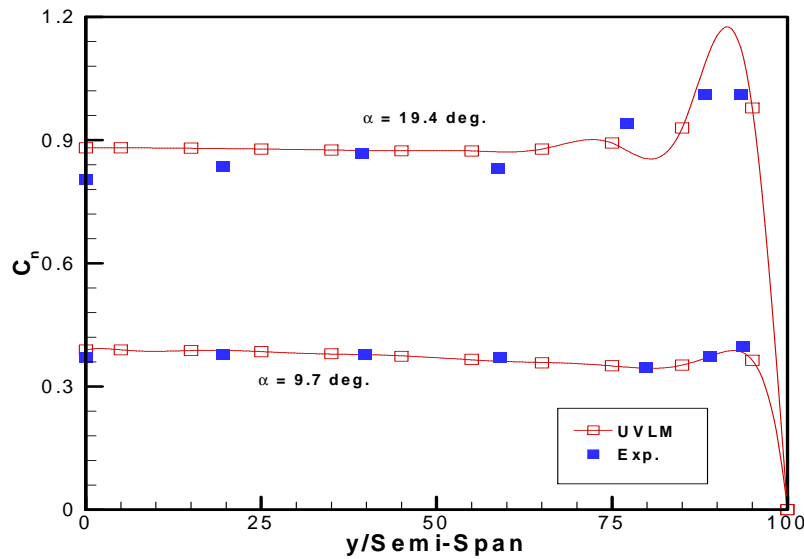
Figure 3-22: Spanwise variation of the local normal-force coefficient for different angles of attack on a flat plate with aspect ratio of 1

Twin Fuselage   Wind
Tunnel Model (Large)
General Arrangement

All Dimensions in Inches
Tail Airfoils: NACA 0012
Wing Airfoil: NACA 23012
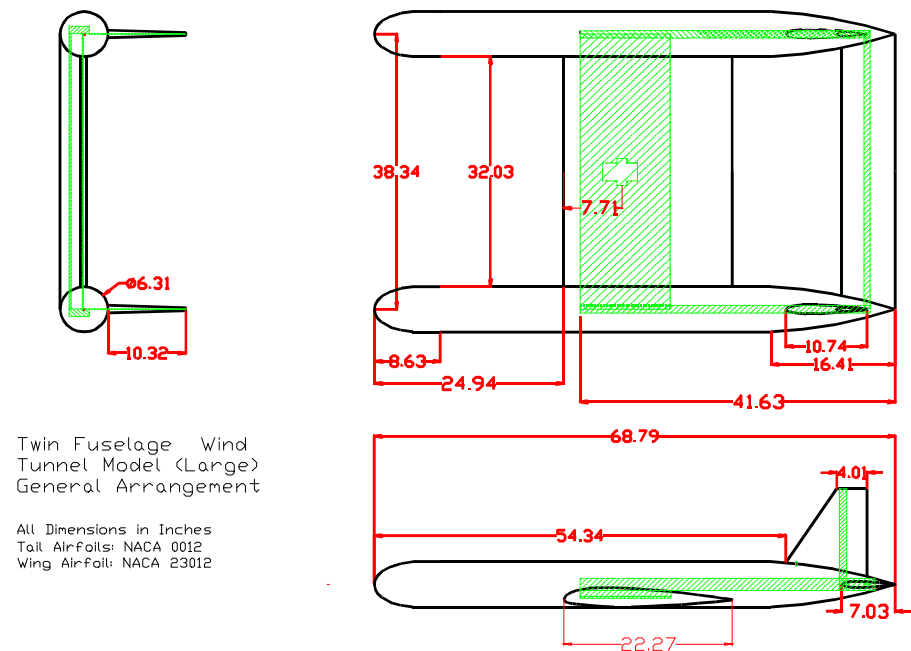
Figure 3-23: Model of an inborad-wing/twin-fuselage configuration
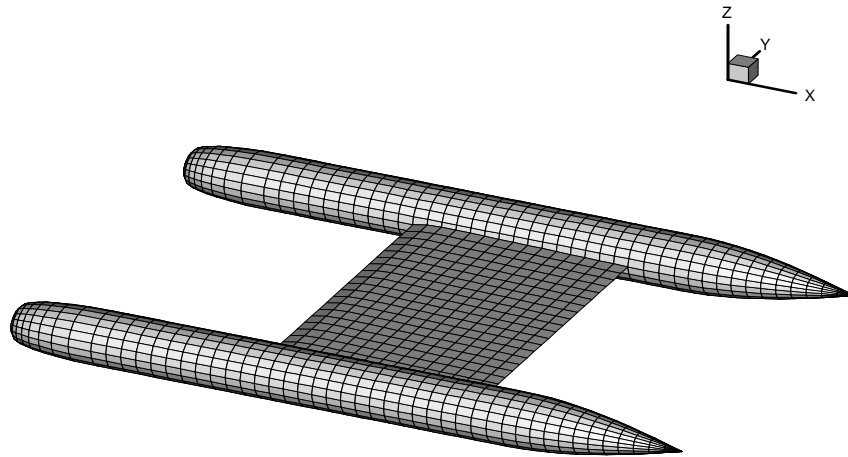
Figure 3-24: The aerodynamic grid of the inboard-wing/twin-fuselage configuration
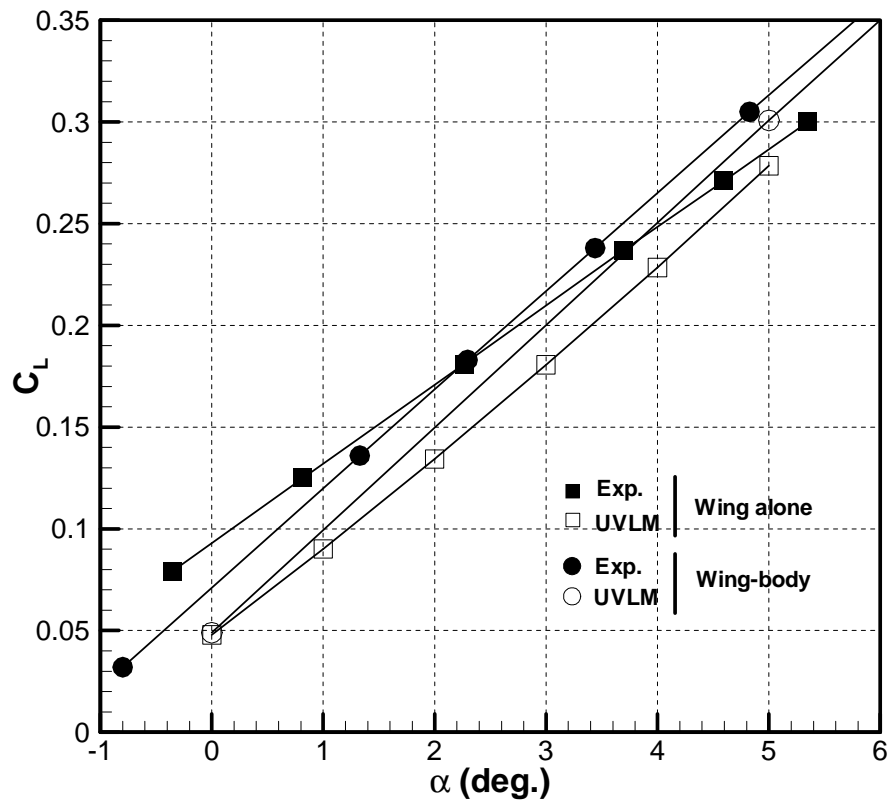
Figure 3-25: Experimental (Spearman *et al.* (1998)) and numerical obtained lift coefficient, C_L, as functions of the angle of attack, α, for the wing and the wing-body combination
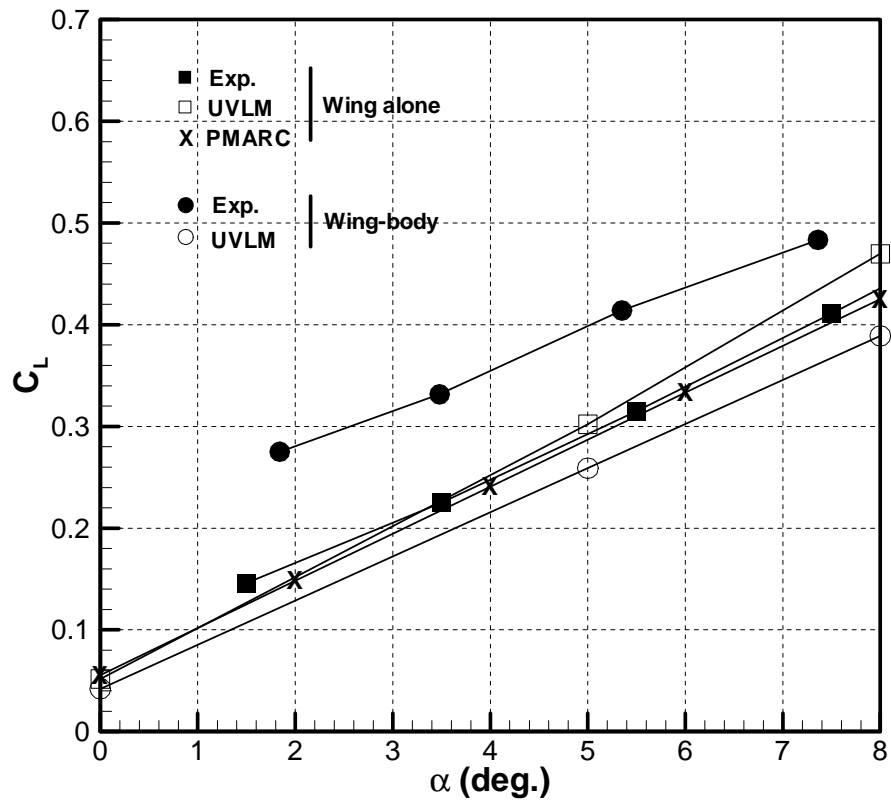
Figure 3-26: Experimentally (Magill (2000)) and numerically obtained lift coefficient, C_L, as functions of the angle of attack, α, for the wing alone and the wing-body combination
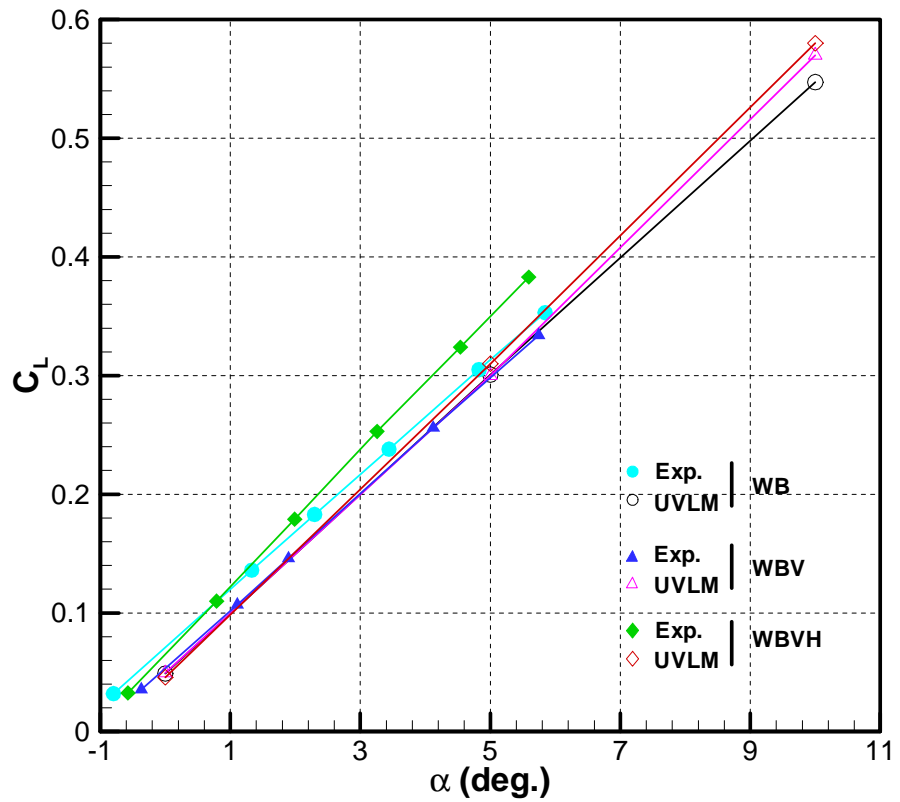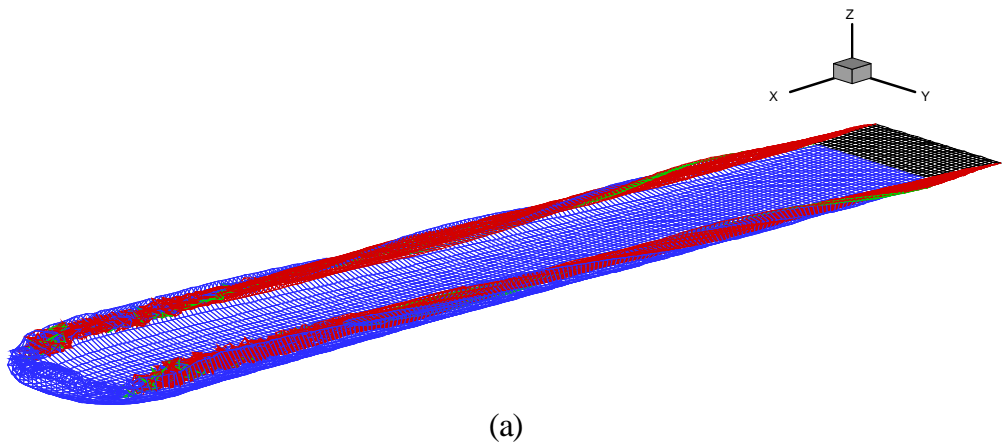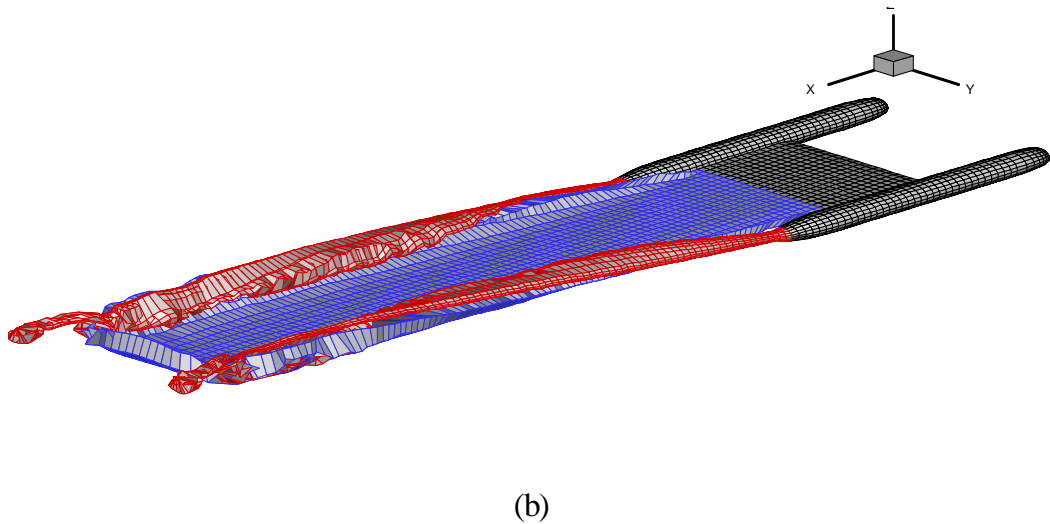
Figure 3-27: Experimentally (Spearman *et al.* (1998)) and numerically obtained lift coefficients, C_L, as functions of angle of attack, α, for various configurations

Figure 3-28: Computed vortex lattices that imitate the wake: (a) wing alone, (b) wing-body combination
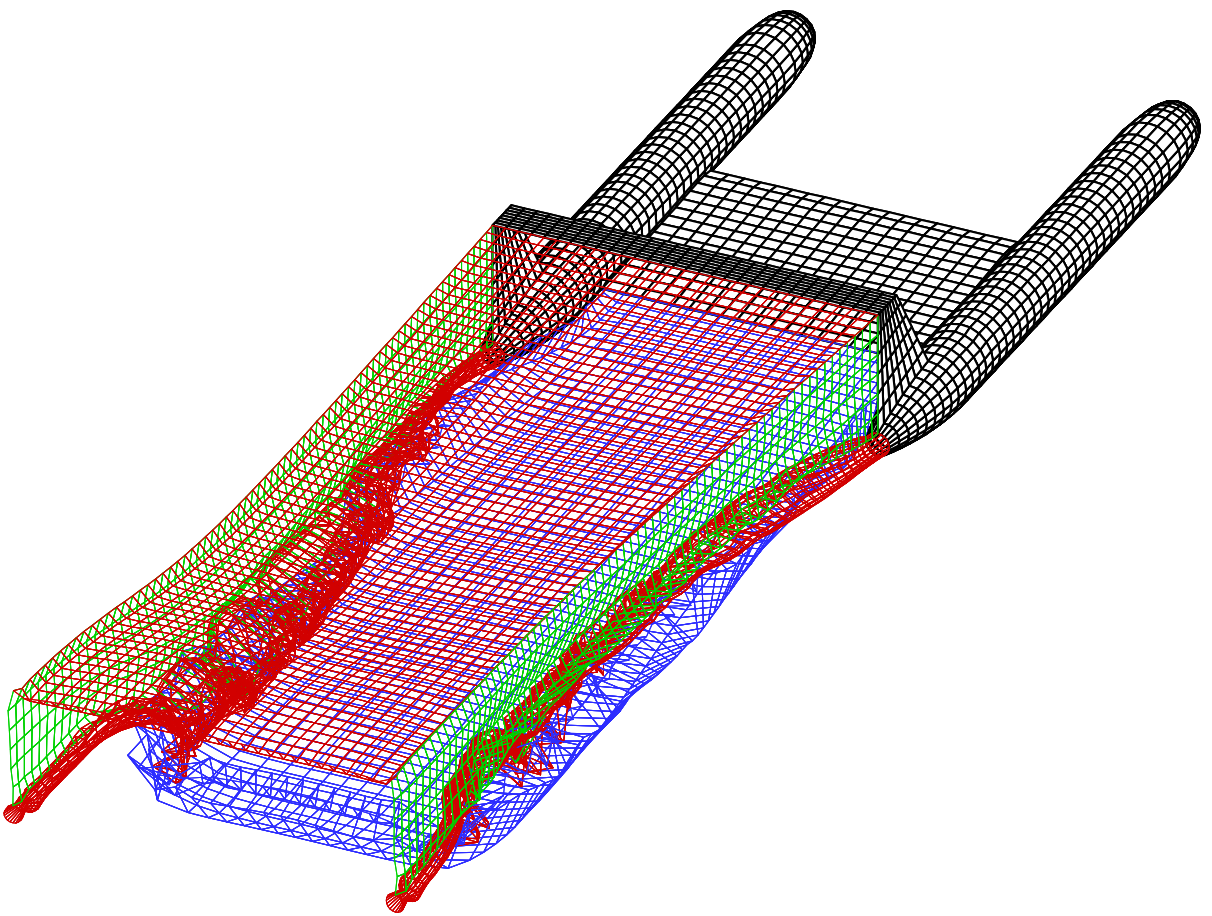
Figure 3-29: Computed vortex lattices that imitate the wake for the complete configuration with wing, fuselages, vertical tails, and horizontal stabilizer
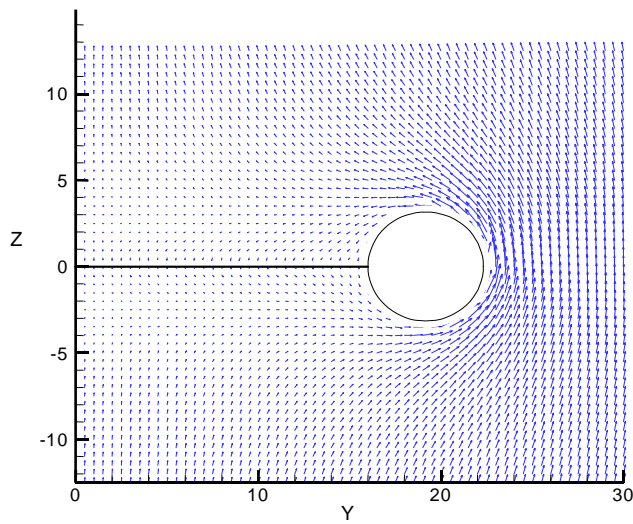
Figure 3-30: Computed cross flow in the Trefftz plane at the mid-chord of the wing-body combination
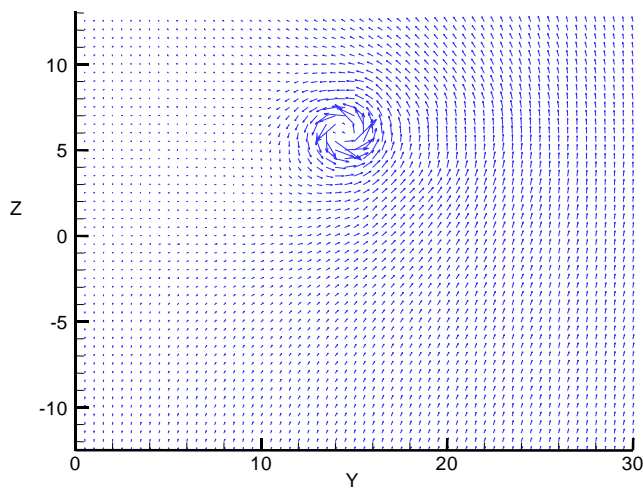

Figure 3-31: Computed cross flow in the Trefftz plane four chord-lengths downstream from the trailing edge of the wing for the wing-body combination
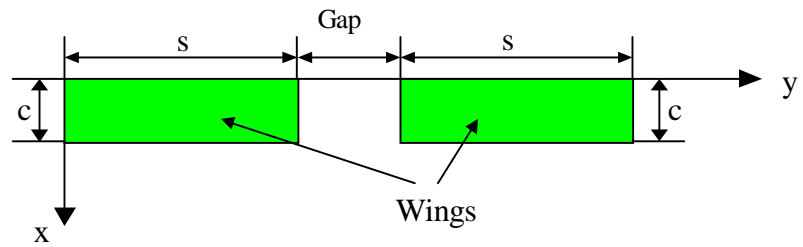
Figure 3-32: Two-wing formation flight configuration
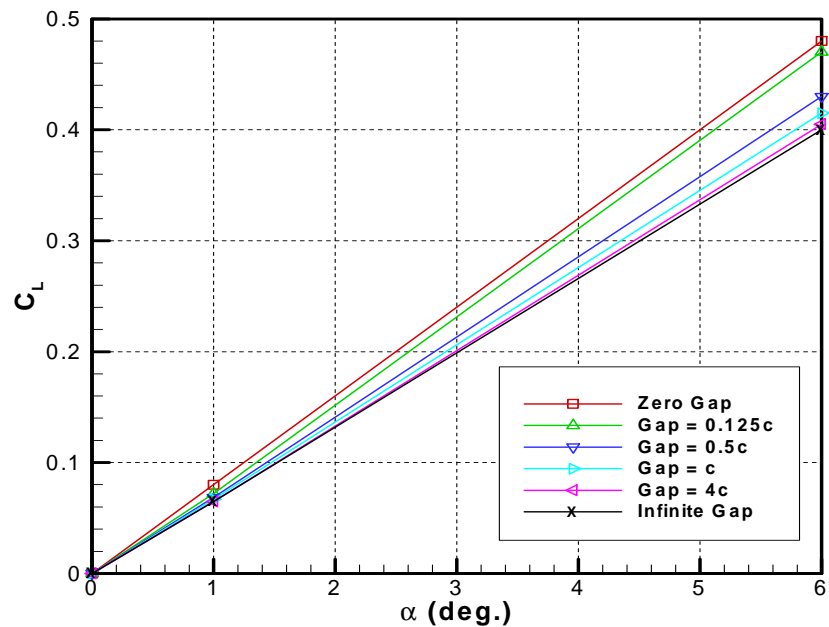
Figure 3-33: Lift coefficient as a function of the angle of attack for the two-wing configuration; c is the chord length of the wing

(a)
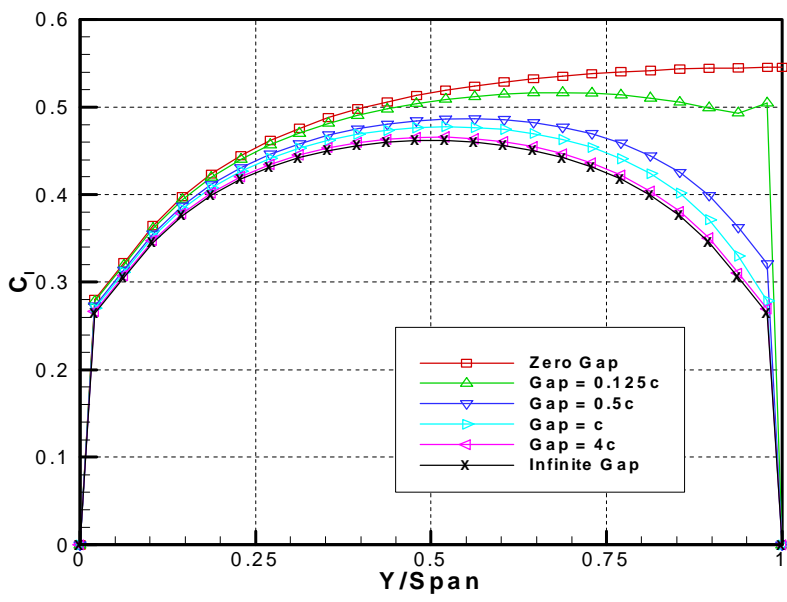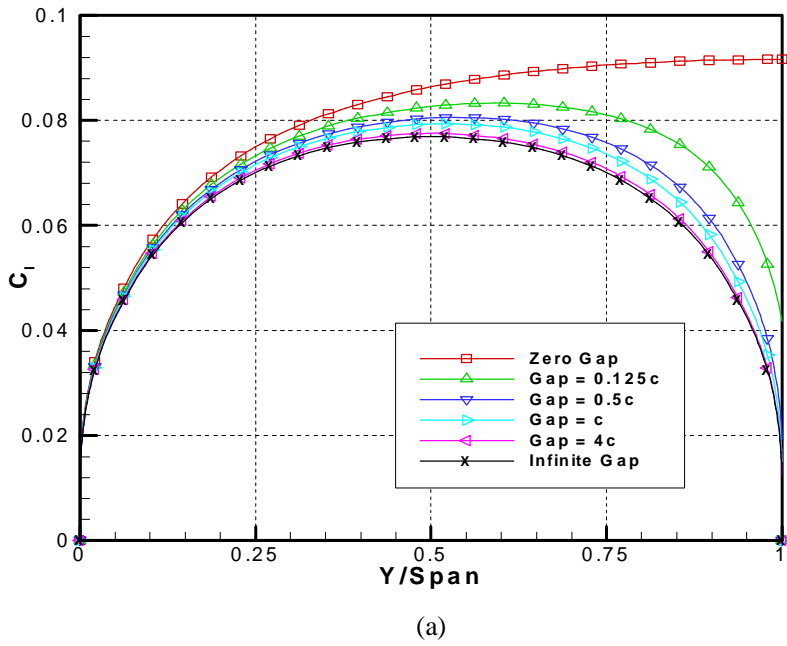
Figure 3-34: The lift distribution as a function of spanwise position for (a) 1 deg. angle of attack, (b) 6 deg. angle of attack for the two-wing configuration
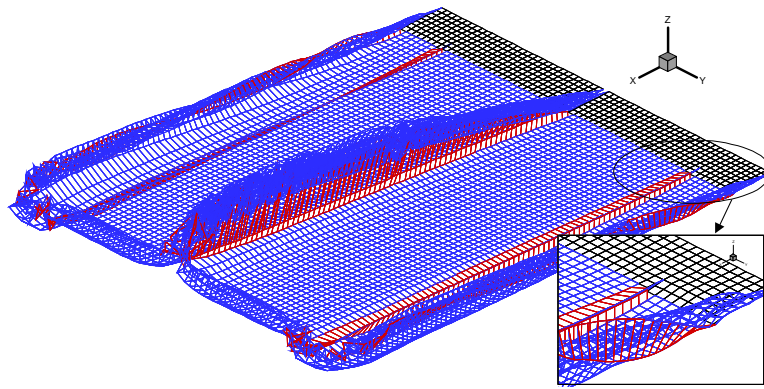
Figure 3-35: The calculated position of the vorticity in the wake when the gap=0.125 chord and the outboard ailerons are deflected five degrees
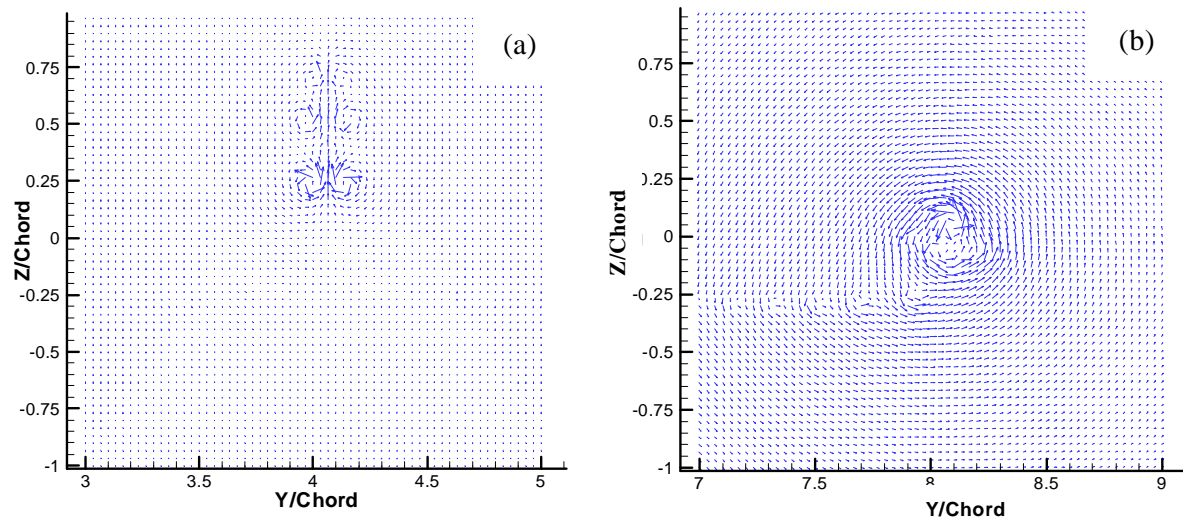
Figure 3-36: The calculated cross flow in a Trefftz plane behind (a) the gap, and (b) the right-hand wingtip without aileron defelction at $6 \deg$. angle of attack

100
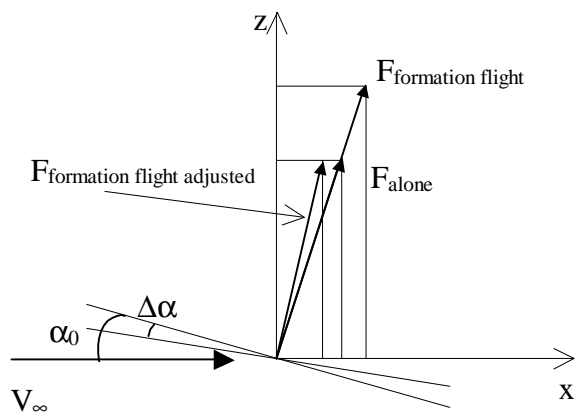
Figure 3-37: Force diagram showing the reduction of induced drag
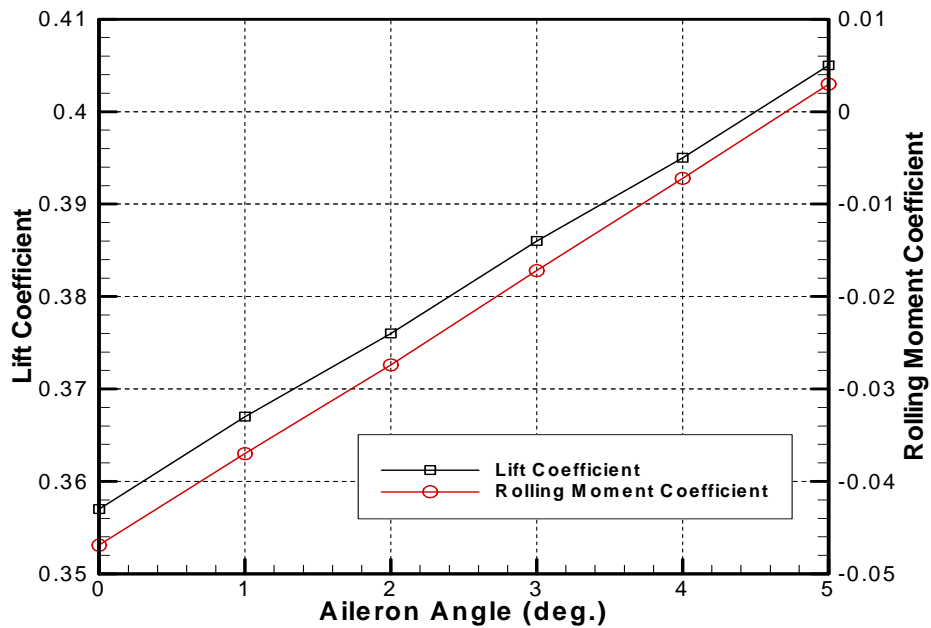
Figure 3-38: The lift and roll moment coefficients as functions of aileron angle at 4.6 deg . angle of attack
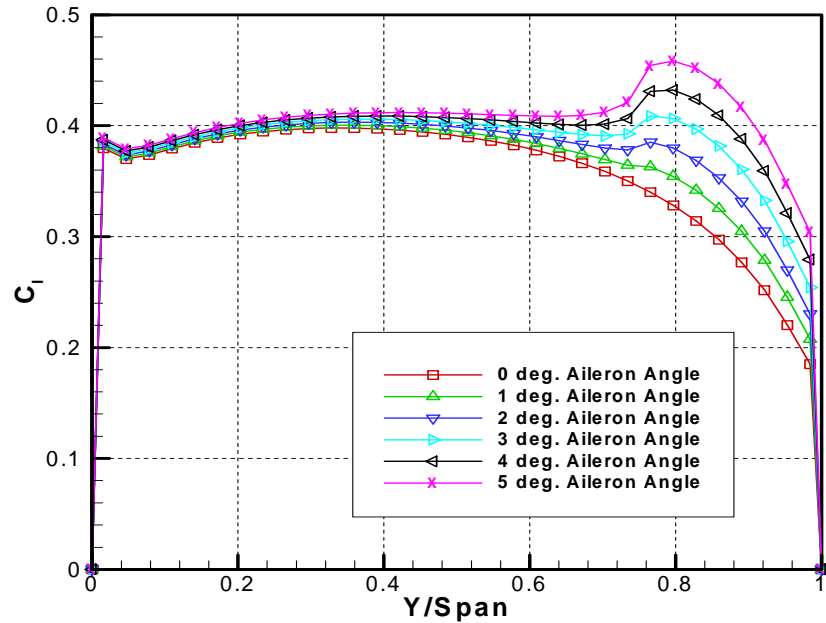
Figure 3-39: Span-wise distributions of section lift for different aileron-deflection angles at $4.6\,\mathrm{deg}$. angle of attack
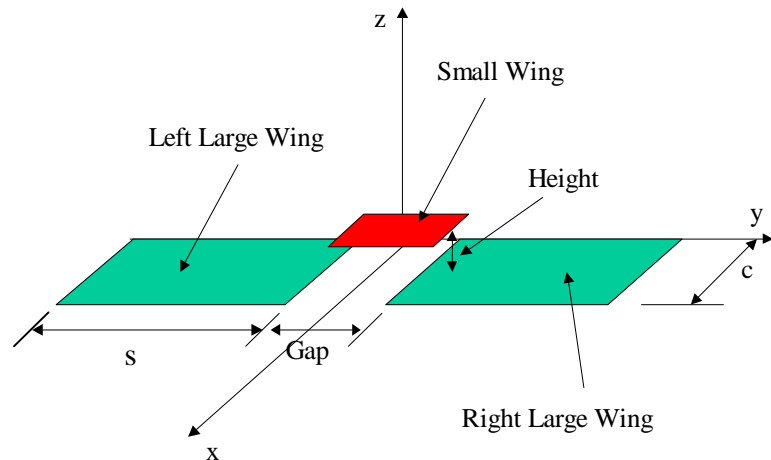
Figure 3-40: The three-wing formation flight configuration

102

(a)
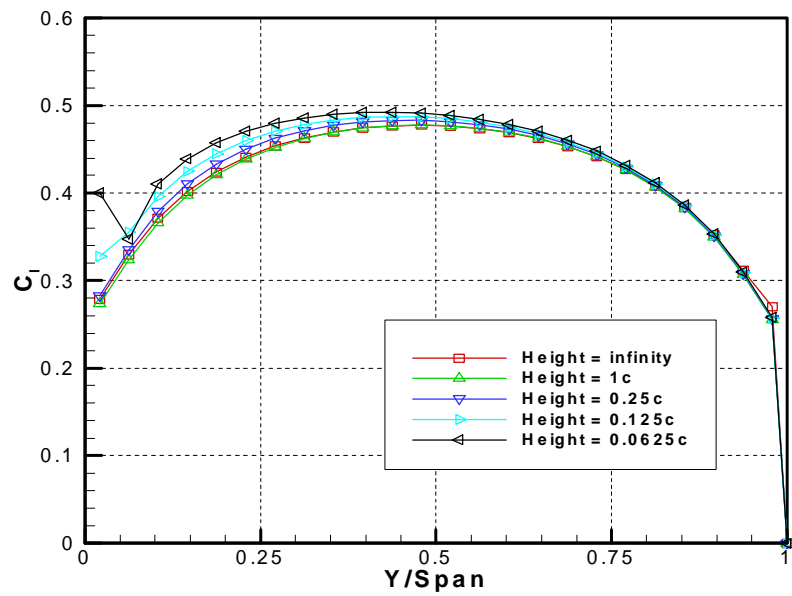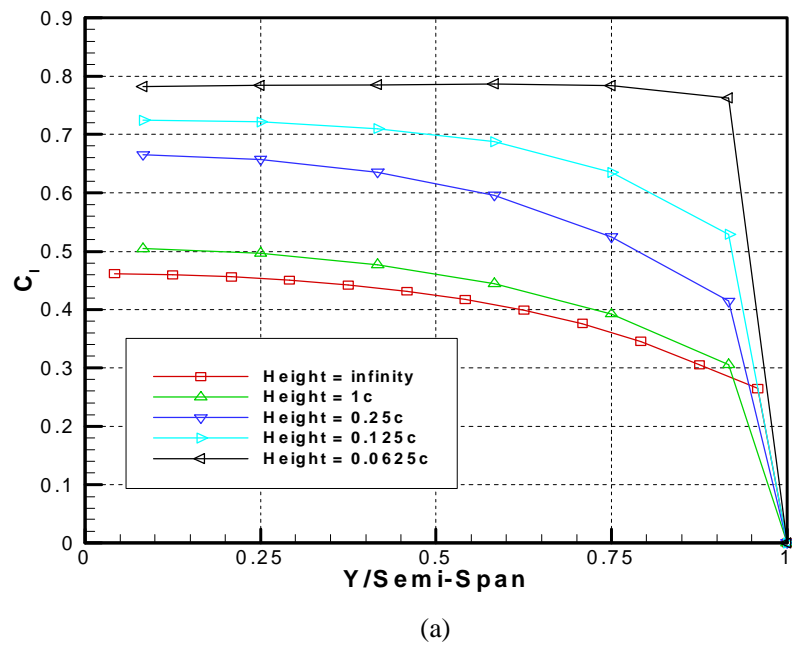
Figure 3-41: Span-wise distributions of section lift for the three-wing configuration at $6 \deg$. angle of attack: (a) the right-hand half of the small wing, and (b) the entire right-hand large wing. c is the chord length of the large wing

103
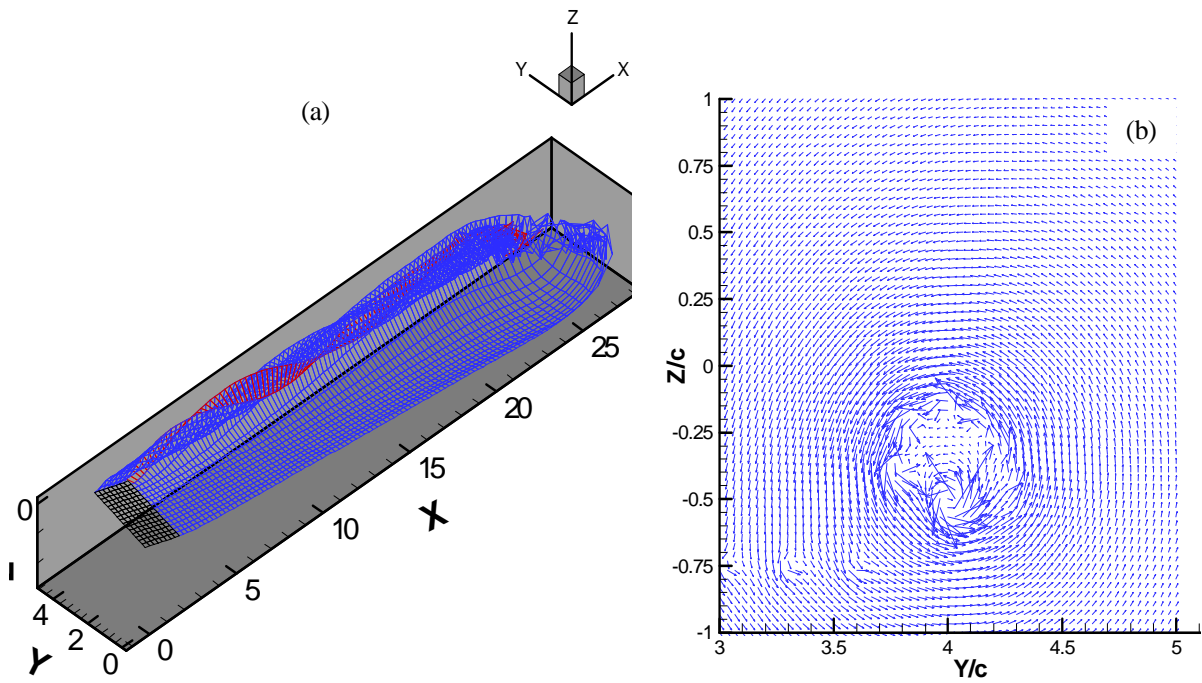
Figure 3-42: (a) the calculated positions of the vortex segments in the wake, and (b) the associated cross flow in a Trefftz plane behind the wing tip for swept wing alone case
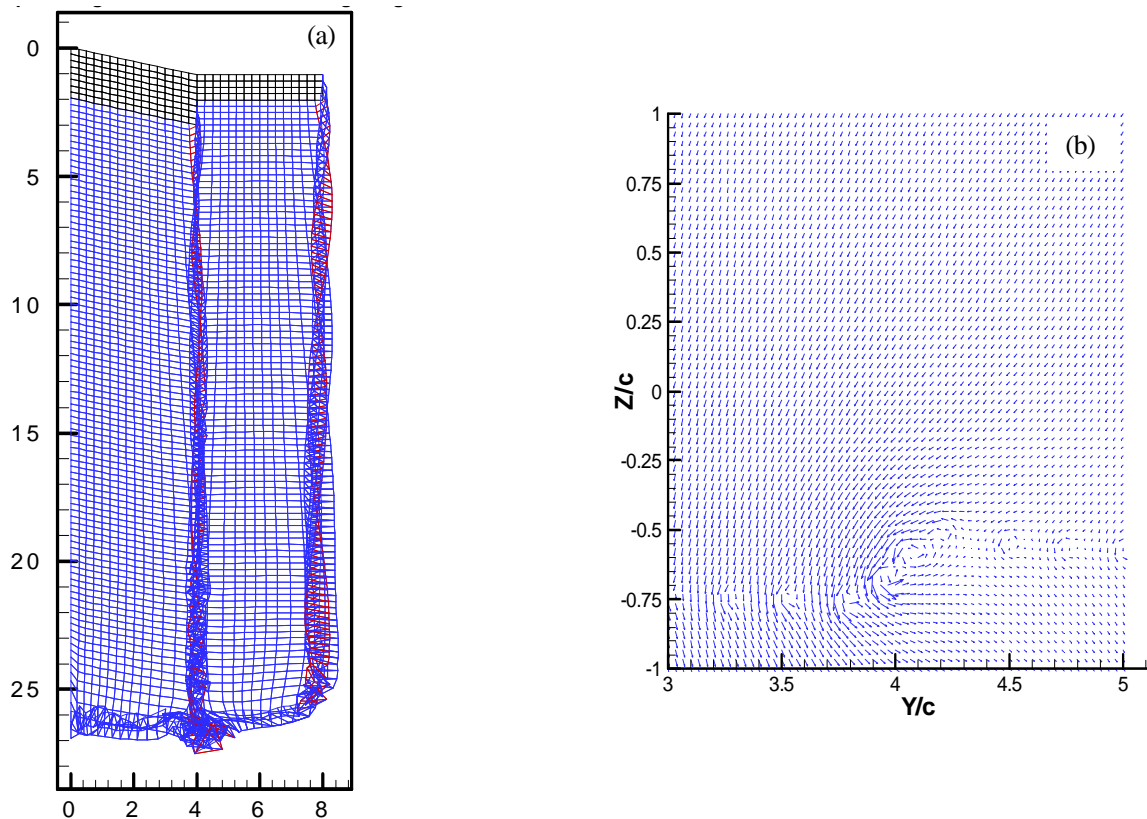
Figure 3-43: (a) the vortex segments in the wake, and (b) the associated cross flow in the plane behind the junction of the swept wing and hitchhiker and four chords down stream from the trailing corner of the swept wing when the wings are aligned at the leading edge
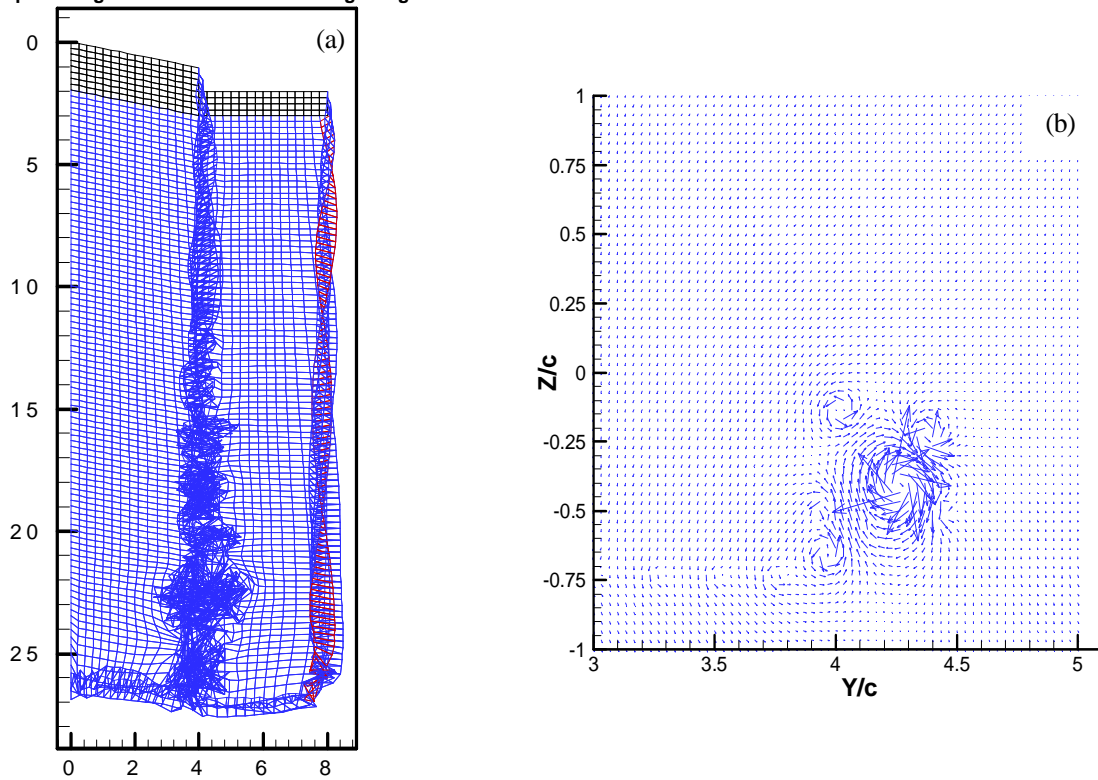
Figure 3-44: (a) the vortex segments in the wakes, and (b) the associated cross flow in a plane four chords downstream from the swept wing when the wings are aligned at the trailing edge

106
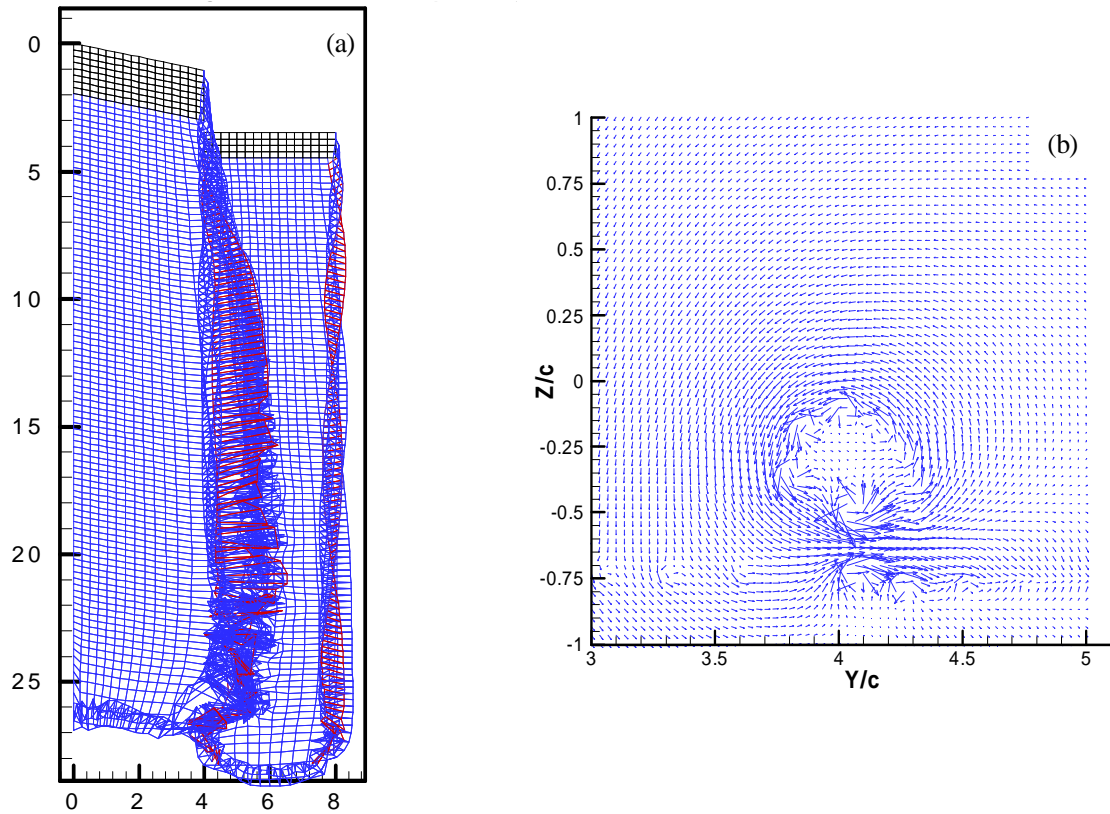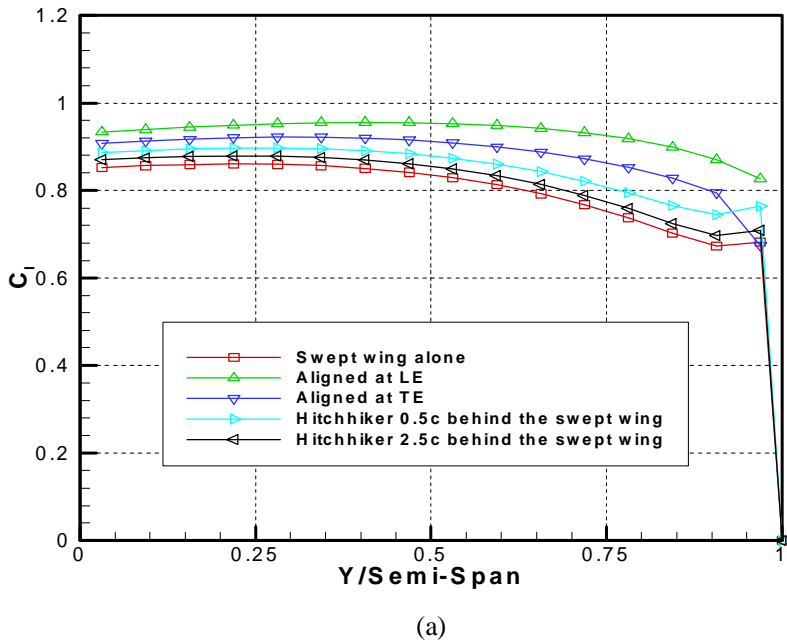
Figure 3-45: (a) the vortex segments in the wakes and (b) the associated cross flow in a plane four chords downstream from the swept wing when the hitchhiker is 0.5c behind the swept wing

107

(a)
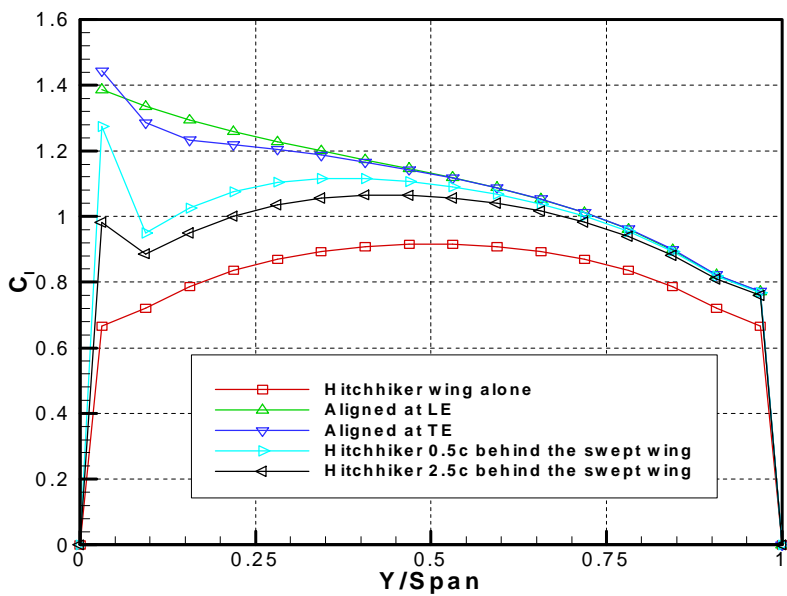
Figure 3-46: The lift distributions along the span for different alignments on (a) the right-hand half of the swept wing, and (b) the entire hitchhiker wing

Chapter 4

Combining the Structural and Aerodynamic Models

We first repeat here our final equation about the generalized coordinates q_i developed in Chapter 2, Equation (2.74), for convenience:

$$\left\{\ddot{q}\right\} + [\Lambda]\left\{q\right\} = [\boldsymbol{\varphi}]^T\left\{F\right\} \tag{4.1}$$

The generalized force vector in the equation, $\{F\}$, usually consists of two parts: $\{F_s\}$ that is from the aerodynamic forces, and $\{F_c\}$ that comes from the control system. i.e.,

$$\{F\} = \{F_s\} + \{F_c\} \tag{4.2}$$

We leave the discussion of control to the next chapter.

Since we use a beam to model the wing, the elastic deformation is calculated from the beam, while the forces are calculated in the aerodynamic grid. We need to find the relation between the elastic beam FEM nodes and the aerodynamic grid. This serves two purposes: one is that, when we know the displacement of the beam nodes, we can determine the new position of the aerodynamic grid; the other is that, when we find the aerodynamic forces, we can transform or map them to the structural forces applied on

the beam model.

4.1 Connection between Finite Element Nodes and Aerodynamic Grid Nodes

The cross sections of the beam are considered to be rigid. The aerodynamic grid points can be regarded to be at the cross sections of the beam and defined in the undeformed local b-system at a distance y from the origin F of the a-system with the coordinates $(r_1, 0, \ r_3)$ (refer to Figure 2-1). Therefore the displacement of a point in the aerodynamic grid is given by

$$\left\{ \begin{array}{c} u_{a1} \\ u_{a2} \\ u_{a3} \end{array} \right\} = \left\{ \begin{array}{c} u_{1s} + r_3\theta_{2s} \\ -r_3\gamma + u_{2s} - r_3 u'_{3s} - r_1 u'_{1s} \\ y\gamma + u_{3s} - r_1\theta_{2s} \end{array} \right\} \tag{4.3}$$

$$= \left\{ \begin{array}{c} 0 \\ -r_3 \\ y \end{array} \right\}\gamma + \left[\begin{array}{cccccc} 1 & 0 & 0 & 0 & r_3 & 0 \\ 0 & 1 & 0 & -r_3 & 0 & -r_1 \\ 0 & 0 & 1 & 0 & -r_1 & 0 \end{array} \right] \left\{ \begin{array}{c} u_{1s} \\ u_{2s} \\ u_{3s} \\ u'_{3s} \\ \theta_{2s} \\ u'_{1s} \end{array} \right\}$$

where the subscripts a and s denote quantities associated with the aerodynamic and structural grids respectively. Generally, y will not exactly fall on a structural node, and so, in these cases the structural displacements are determined by interpolation.

4.1.1 Interpolation

In the case when y coordinate is not on a structural node, we assume it is located between nodes y_i and y_j. Then the displacement vector at location y is obtained by interpolation

110

using the shape functions that have been given in Chapter 2:

$$
\left\{
\begin{array}{c}
u_{1s} \\
u_{2s} \\
u_{3s} \\
u'_{3s} \\
\theta_{2s} \\
u'_{1s}
\end{array}
\right\}
= [N_s]
\left\{
\begin{array}{c}
u_{1i} \\
u_{2i} \\
u_{3i} \\
u'_{3i} \\
\theta_{2i} \\
u'_{1i} \\
u_{1j} \\
u_{2j} \\
u_{3j} \\
u'_{3j} \\
\theta_{2j} \\
u'_{1j}
\end{array}
\right\}
\tag{4.4}
$$

where

$$
[N_s] =
\begin{bmatrix}
N_i^0 & 0 & 0 & 0 & 0 & N_i^1 & N_j^0 & 0 & 0 & 0 & 0 & N_j^1 \\
0 & N_i & 0 & 0 & 0 & 0 & 0 & N_j & 0 & 0 & 0 & 0 \\
0 & 0 & N_i^0 & N_i^1 & 0 & 0 & 0 & 0 & N_j^0 & N_j^1 & 0 & 0 \\
0 & 0 & \frac{d}{dy}N_i^0 & \frac{d}{dy}N_i^1 & 0 & 0 & 0 & 0 & \frac{d}{dy}N_j^0 & \frac{d}{dy}N_j^1 & 0 & 0 \\
0 & 0 & 0 & 0 & N_i & 0 & 0 & 0 & 0 & 0 & N_j & 0 \\
\frac{d}{dy}N_i^0 & 0 & 0 & 0 & 0 & \frac{d}{dy}N_i^1 & \frac{d}{dy}N_j^0 & 0 & 0 & 0 & 0 & \frac{d}{dy}N_j^1
\end{bmatrix}
\tag{4.5}
$$

and the finite element shape functions and their derivatives are evaluated at location y.

4.1.2 Connection to the End Node

It is possible that an aerodynamic grid point may intersect the extension of the elastic-axis of the beam model. In this situation, the aerodynamic grid point is expressed with the coordinates (r_1, r_2, r_3) in the local b-system at the end finite element node. We

make a small change to the Equation (4.3), so that the displacements of the point in the aerodynamic grid are determined by the displacements of the end finite element node:

$$
\left\{ \begin{array}{c} u_{a1} \\ u_{a2} \\ u_{a3} \end{array} \right\} = \left\{ \begin{array}{c} u_{1s} + r_3\theta_{2s} \\ -r_3\gamma + u_{2s} - r_3u'_{3s} - r_1u'_{1s} \\ y\gamma + u_{3s} - r_1\theta_{2s} \end{array} \right\} \tag{4.6}
$$

$$
= \left\{ \begin{array}{c} 0 \\ -r_3 \\ y \end{array} \right\} \gamma + \left[\begin{array}{cccccc} 1 & 0 & 0 & 0 & r_3 & -r_2 \\ 0 & 1 & 0 & -r_3 & 0 & -r_1 \\ 0 & 0 & 1 & r_2 & -r_1 & 0 \end{array} \right] \left\{ \begin{array}{c} u_{1N} \\ u_{2N} \\ u_{3N} \\ u'_{3N} \\ \theta_{2N} \\ u'_{1N} \end{array} \right\}
$$

Using the above three equations (4.3), (4.4), and (4.6), we can construct the following equation to relate the deformations of the points in the aerodynamic grid with those of the finite element nodes:

$$
\{U_a\} = [G_{as}]\{U_s\} \tag{4.7}
$$

where $\{U_a\}$ is the vector containing the displacements of all of the aerodynamic grid points, $\{U_s\}$ is the vector containing the overall rolling angle and the structural nodal displacements, and $[G_{as}]$ is a rather sparse matrix with all of the relevant geometrical data. The same expression can be used to relate the velocities when the displacements are replaced with their time derivatives.

4.2 Connection between Finite Element Nodes and Aerodynamic Control Points

The aerodynamic forces are evaluated at the control points of the aerodynamic grid, thus, we also need the transfer matrix between the displacements of the control points

and those of the finite element nodes. For any panel in the aerodynamic grid, the position of the control point (both initially and during the motion) is the average of the positions of the four vertices, so that we can compute the displacements of the control point as follows:

$$
\left\{ \begin{array}{c} u_{a1}^{CP} \\ u_{a2}^{CP} \\ u_{a3}^{CP} \end{array} \right\} = \frac{1}{4} \left(\left\{ \begin{array}{c} u_{a1}^{i} \\ u_{a2}^{i} \\ u_{a3}^{i} \end{array} \right\} + \left\{ \begin{array}{c} u_{a1}^{j} \\ u_{a2}^{j} \\ u_{a3}^{j} \end{array} \right\} + \left\{ \begin{array}{c} u_{a1}^{k} \\ u_{a2}^{i} \\ u_{a3}^{k} \end{array} \right\} + \left\{ \begin{array}{c} u_{a1}^{l} \\ u_{a2}^{l} \\ u_{a3}^{l} \end{array} \right\} \right) \qquad (4.8)
$$

The displacements at the four aerodynamic grid points i, j, k, l of the element at which the control point is located are found by using either Equation (4.3), or (4.4), or (4.6). From Equation (4.8), we are able to find the geometric relation matrix between the aerodynamic control points and the finite element nodes; we denote this matrix as $\left[G_{as}^{CP} \right]$:

$$
\left\{ U_a^{CP} \right\} = \left[G_{as}^{CP} \right] \left\{ U_s \right\} \qquad (4.9)
$$

where $\left\{ U_a^{CP} \right\}$ is the vector containing the displacements of all aerodynamic control points.

4.3   Principle of Virtual Work

Now we consider the transfer, or mapping, of the aerodynamic loads from the aerodynamic grid onto the structural space. This transfer is based on the stipulation that the virtual work done by the aerodynamic loads must equal that done by the equivalent structural loads. Equating the virtual work leads to

$$
\delta W_a = \delta W_s \qquad (4.10)
$$

where δW_a is the virtual work done by the aerodynamic forces over the virtual displacements of the aerodynamic control points, $\left\{ \delta U_a^{CP} \right\}$, and δW_s is the virtual work done by the structural forces over the virtual displacements of the finite element nodes, $\left\{ \delta U_s \right\}$,

i.e.,

$$\delta W_a = \left\{ \delta U_a^{CP} \right\}^T \left\{ F_a^{CP} \right\} \tag{4.11}$$

and

$$\delta W_s = \left\{ \delta U_s \right\}^T \left\{ F_s \right\} \tag{4.12}$$

Thus,

$$\left\{ \delta U_a^{CP} \right\}^T \left\{ F_a^{CP} \right\} = \left\{ \delta U_s \right\}^T \left\{ F_s \right\} \tag{4.13}$$

Substituting Equation (4.9) into Equation (4.13) yields:

$$\left\{ \delta U_s \right\}^T \left[G_{as}^{CP} \right]^T \left\{ F_a^{CP} \right\} = \left\{ \delta U_s \right\}^T \left\{ F_s \right\} \tag{4.14}$$

This equation must hold for every admissible $\{\delta U_s\}$, so we end up with the following relationship between aerodynamic forces $\left\{ F_a^{CP} \right\}$ and structural forces $\{F_s\}$:

$$\{F_s\} = \left[G_{as}^{CP} \right]^T \left\{ F_a^{CP} \right\} \tag{4.15}$$

4.4   Numerical-Integration Algorithm

Hamming's fourth-order predictor-corrector technique is used to simultaneously and interactively integrate the aerodynamic and structural equations of motion. This algorithm, instead of the commonly used Runge-Kutta method, was chosen for several reasons: (1) the general unsteady vortex lattice aerodynamic model provides better results when the loads are evaluated at only the integral time steps, (2) the aerodynamic loads contain contributions that are implicitly proportional to the accelerations, and (3) the interaction between the wing's motion and the aerodynamics can be readily handled by iteration to account for each other's effects during each time step.

To proceed with the numerical integration procedure, we first nondimensionalize the

equations of motion. Using the dimensionless time,

$$t^* = \frac{t}{L_C/V_C} = \frac{t}{T_C} \tag{4.16}$$

where the characteristic time $T_C = L_C/V_C$, the characteristic length L_C which is usually the size of one typical element of the aerodynamic mesh, and the characteristic velocity $V_C = V_\infty$, we get

$$\dot{q} = \frac{dq}{dt} = \frac{dq}{dt^*}\frac{dt^*}{dt} = \frac{1}{T_C}\frac{dq}{dt^*} \tag{4.17}$$

and similarly,

$$\ddot{q} = \frac{d^2q}{dt^2} = \frac{1}{T_C^2}\frac{d^2q}{dt^{*2}} \tag{4.18}$$

Note that the generalized coordinates q_i are already dimensionless variables.

Equation (4.1) then becomes

$$\frac{1}{T_C^2}\left\{\frac{d^2q}{dt^{*2}}\right\} + [\Lambda]\{q\} = [\varphi]^T\{F\} \tag{4.19}$$

Multiplying both sides by T_C^2, and converting the result to first-order differential equations leads to

$$\frac{d}{dt^*}\left\{\begin{array}{c} q \\ dq/dt^* \end{array}\right\} = \left\{\begin{array}{c} dq/dt^* \\ -T_C^2[\Lambda]\{q\} + T_C^2[\varphi]^T\{F\} \end{array}\right\} \tag{4.20}$$

By denoting that

$$\{p\} = \left\{\begin{array}{c} q \\ dq/dt^* \end{array}\right\}, \text{ and } \{R\} = \left\{\begin{array}{c} dq/dt^* \\ -T_C^2[\Lambda]\{q\} + T_C^2[\varphi]^T\{F\} \end{array}\right\} \tag{4.21}$$

we have

$$\frac{d}{dt^*}\{p\} = \{R\} \tag{4.22}$$

Since Hamming's fourth-order predictor-corrector algorithm requires the solutions at three previous steps to calculate the solution at the current time, it is necessary to set

115

up an algorithm to provide the first four solutions, including the zero-time, or initial conditions. In the following we give the procedure of integration step by step:

1) At t_0 (i.e., $t = 0$), we give the initial conditions of the wing, $\{p\}^0$, consisting of the initial position and the initial velocity of the wing. No wake vortex is shed from the trailing edges and wing tips of the wing. Evaluate the right hand side of Equation (4.22):

$$\left\{\dot{p}\right\}^0 = \{R\}^0 = \left\{R\left(p^0\right)\right\} \tag{4.23}$$

2) At t_1 (i.e., $t = \Delta t$), vorticity is shed and convects to its new position based on the state of the system at moment t_0. The predicted solution, $^p\{p\}^1$, is computed by Euler method:

$$^p\{p\}^1 = \{p\}^0 + \Delta t \{R\}^0 \tag{4.24}$$

The predicted solution is corrected by iteration through using the modified Euler method:

$$^{k+1}\{p\}^1 = \{p\}^0 + \frac{\Delta t}{2}\left(^k\{R\}^0 + \{R\}^0\right) \tag{4.25}$$

where k denotes the iteration number, and $^k\{R\}^0 = \left\{R\left(^kp^1\right)\right\}$ with $^1p^1 = {}^p\{p\}^1$. The position of the aerodynamic grid is updated with $^kp^1$ during the iteration.

The iterations do not stop until the iteration error which is defined as the maximum component of the absolute difference between the consecutive solutions:

$$err = \max_{1 \leq i \leq m}\left|{}^{k+1}p_i^1 - {}^k p_i^1\right| \tag{4.26}$$

is less than the prescribed error tolerance ε. Then

$$\{p\}^1 = {}^{k+1}\{p\}^1, \quad \{R\}^1 = \left\{R\left(p^1\right)\right\} \tag{4.27}$$

During the iterations, we do not recalculate the position of the wake. Numerical experiments show that this is adequate, see Preidikman (1998).

3) At t_2 (i.e., $t = 2\Delta t$), more vorticity is shed and all the vorticity in the wake is

convected to its new position according to the state of the system at moment t_1; the predicted solution, $^p\{p\}^2$, is computed by Adams-Bashforth two-step predictor method:

$$^p\{p\}^2 = \{p\}^1 + \frac{\Delta t}{2}\left(3\{R\}^1 - \{R\}^0\right) \tag{4.28}$$

The solution is corrected iteratively by using Adams-Moulton two-step method:

$$^{k+1}\{p\}^2 = \{p\}^1 + \frac{\Delta t}{12}\left(5\ ^k\{R\}^2 + 8\{R\}^1 - \{R\}^0\right) \tag{4.29}$$

where $^k\{R\}^2 = \left\{R\left(^k p^2\right)\right\}$ with $^1 p^2 = {}^p\{p\}^2$.

4) At t_3 (i.e., $t = 3\Delta t$), the wake is convected to its new position according to the state of the system at moment t_2; the predicted solution, $^p\{p\}^3$, is computed by Adams-Bashforth three-step predictor method:

$$^p\{p\}^3 = \{p\}^2 + \frac{\Delta t}{12}\left(23\{R\}^2 - 16\{R\}^1 + 5\{R\}^0\right) \tag{4.30}$$

The solution is iterated by using Adams-Moulton three-step method:

$$^{k+1}\{p\}^3 = \{p\}^{12} + \frac{\Delta t}{24}\left(9\ ^k\{R\}^3 + 19\{R\}^2 - 5\{R\}^1 + \{R\}^0\right) \tag{4.31}$$

where $^k\{R\}^3 = \left\{R\left(^k p^3\right)\right\}$ with $^1 p^3 = {}^p\{p\}^3$.

5) For t_4, t_5, t_6, $\cdots$ (i.e., $t = 4\Delta t$, $t = 5\Delta t$, $t = 6\Delta t$, $\cdots$), the wake is convected to its new position according to the state of the system at previous moment; the solution is computed by using Hamming's fourth-order modified predictor-corrector method. The predicted solution, $^p\{p\}^j$ ($j = 4,\ 5,\ 6,\ \cdots$), is calculated by

$$^p\{p\}^j = \{p\}^{j-4} + \frac{4\Delta t}{3}\left(2\{R\}^{j-1} - \{R\}^{j-2} + 2\{R\}^{j-3}\right) \tag{4.32}$$

The predicted solution is modified by using the local truncation error from the previous time step:

$$^1\{p\}^j = {}^p\{p\}^j + \frac{112}{9}\{e\}^{j-1} \tag{4.33}$$

117

where $\{e\}^3$ is assumed to be a zero vector.

Then the solution is iterated by using the corrector equation:

$$^{k+1}\{p\}^j = \frac{1}{8}\left(9\{p\}^{j-1} - \{p\}^{j-3} + 3\Delta t \left(^k\{R\}^j + 2\{R\}^{j-1} - \{R\}^{j-2}\right)\right) \qquad (4.34)$$

where $^k\{R\}^j = \{R\left(^kp^j\right)\}$ with $^1p^j = {}^p\{p\}^j$.

When the error tolerance is satisfied, we use the following expression to estimate the local truncation error:

$$\{e\}^j = \frac{9}{121}\left(^{k+1}\{p\}^j - {}^p\{p\}^j\right) \qquad (4.35)$$

The final solution at step j is given by

$$\{p\}^j = {}^{k+1}\{p\}^j - \{e\}^j \qquad (4.36)$$

4.5 Numerical Examples

4.5.1 Stability Analysis of the Hitchhiker Wing

Configurations consisting of several airplanes flying in a staggered or swept formation or flying wing tip to wing tip are considered for the purpose of improving range or economy. We have analyzed the aerodynamics for the formation flights. Here we investigate the stability of one of the docking configurations.

As early as the 1940's and 1950's, several projects that included many flight tests were conducted, one of which is the well-known Tom-Tom project. Unfortunately this work ended with a disaster. On April 24, 1953, during the towing test, one F-84 hitchhiking fighter airplane flapped upward and rolled into the B-29. No one survived in this accident.

Several research groups including those working in wind tunnels, water tunnels, and structural analysis, at Virginia Tech recently teamed together and cooperated with the Lockheed Martin Corporation to review the concept of compound aircraft transportation (CAT) under DARPA Contract MDA972-01-C-0046. In the initial phase of the work great emphasis is placed on the instabilities that had been demonstrated in the earlier tests of

compound aircraft flights.

As a member of the above CAT group, we couple the general unsteady vortex-lattice method (UVLM) with the rigid-body motion of the wing structure to investigate the effects of the relative positioning between the main aircraft and the hitchhiker on the stability. Different from the flutter analysis where the elastic deformation of the wing structure is coupled with the aerodynamics, here we only have the rolling motion of the hitchhiker wing. Figure 4-1 shows a schematic representation of the compound flights that to be analyzed. Both wings are represented by planar rectangular lifting surfaces with an aspect ratio of 4. Three coordinate systems are involved in the configuration. The A-system is fixed on the main wing, the C-system is fixed on the hitchhiker wing (which is implicit in the figure) and is coincident with the B-system at the initial moment. The main wing is assumed to be fixed in position; while the hitchhiker wing can rotate about either $\overrightarrow{b_1}$ or the $\overrightarrow{c_1}$ axis which is aligned with the hinge. The flow in the aerodynamic model is symmetric about the plane formed by $\overrightarrow{a_1}$ and $\overrightarrow{a_3}$, i.e., there is another hitchhiker wing on the other side, otherwise non-symmetry exists.

The transformation matrix between the A and B-systems is defined by:

$$
\left\{ \begin{array}{c} \overrightarrow{b_1} \\ \overrightarrow{b_2} \\ \overrightarrow{b_3} \end{array} \right\} = \left[\begin{array}{ccc} \cos \beta_H & \sin \beta_H & 0 \\ -\sin \beta_H & \cos \beta_H & 0 \\ 0 & 0 & 1 \end{array} \right] \left[\begin{array}{ccc} \cos \alpha_H & 0 & -\sin \alpha_H \\ 0 & 1 & 0 \\ \sin \alpha_H & 0 & \cos \alpha_H \end{array} \right] \left\{ \begin{array}{c} \overrightarrow{a_1} \\ \overrightarrow{a_2} \\ \overrightarrow{a_3} \end{array} \right\} \tag{4.37}
$$

where α_H, β_H are the hinge pitch angle and the yaw angle between the main wing and the hitchhiker wing, respectively. When the hitchhiker wing is swept forward, β_H is positive. Since no elastic deformation is considered, the equation of motion (EOM) for the hitchhiker wing is only its rolling-motion equation, which is defined at the B-system as follows:

$$
I\ddot{\gamma} = M = M_a + M_g \tag{4.38}
$$

where γ is the rolling angle, M_a is the moment from the aerodynamic forces, M_g is the moment generated by gravity force.

119

EOM can be rewritten in form of two first-order differential equations:

$$\left\{ \begin{array}{c} \dot{\gamma} \\ \dot{\omega} \end{array} \right\} = \left\{ \begin{array}{c} \omega \\ M/I \end{array} \right\} \tag{4.39}$$

We nondimensionalize the EOM by defining dimensionless time t^*:

$$t^* = \frac{t}{L_C/V_C} \tag{4.40}$$

so that the equation becomes

$$\left\{ \begin{array}{c} d\gamma/dt^* \\ d\omega^*/dt^* \end{array} \right\} = \left\{ \begin{array}{c} \omega^* \\ M^*/I^* \end{array} \right\} \tag{4.41}$$

where

$$\omega^* = \frac{\omega}{V_C/L_C}, \ \ M^* = \frac{M}{\frac{1}{2}\rho_\infty V_C^2 L_C^3}, \ \text{and} \ I^* = \frac{I}{\frac{1}{2}\rho_\infty L_C^5}$$

Now that we have the same form of the equations as the one when elastic deformations are considered, we can use the integration procedure described in this chapter to numerically simulate the flapping motion of the hitchhiker wing. To investigate the stability of this compound flight configuration, we give the hitchhiker wing an initial rolling angular velocity. Simulations are conducted at zero angle of attack. Numerical solutions for a positive 6 degrees of yawing angle and a negative 6 degrees of yawing angle between the main wing and the hitchhiker wing are shown in Figure 4-2.

If there is no yawing angle between the two wings, it is not hard to imagine in such a case that the initial rolling angular velocity will virtually result in an uneven distributed negative angle of attack in the hitchhiker wing. The aerodynamic forces generated by this negative angle of attack will push the hitchhiker wing back. However, when a yawing angle exists, similar to the analytical divergence analysis for a swept wing, there will be a wash in or wash out effect associated with the swept forward angle or the swept backward angle respectively.

In part (a) of Figure 4-2, it is shown that there is definitely an instability associated with the positive yawing angle; the rolling angle keeps growing with the positive β_H. Conversely, the rolling angle is increasing initially, then decreasing and approaching zero when β_H is negative. In part (b) of Figure 4-2, the evolution of the rolling angular velocity is shown; it assures the same argument. With a negative β_H, rolling angular velocity finally approaches zero. The experiments in a small wind tunnel at ESM department of Virginia Tech show the same phenomena.

4.5.2 HALE Aircraft Wing Cantilevered from the Wall of the Wind Tunnel

For the flutter analysis, we first of all analyze the case when the rolling motion of the aircraft is not included, i.e., the wing is considered as a cantilever beam, which corresponds to a semi-span wing cantilevered from the wall of the wind tunnel. The flow is considered symmetric about the wall of the wind tunnel. The modes with lower frequencies are easier to excite compared to the modes with higher frequencies. The structural properties are given in Table 2-1, and the first six natural modes are shown in Figure 2-7. We list the natural frequencies in Table 4-1. We see that there is a sharp jump from the fifth mode, and considering that the fourth mode is the back and forth in-plane bending mode which does not play an important role in the flutter analysis, we expect to see that the first 3 modes will be sufficient for our analysis.

Mode No.	1	2	3	4	5	6	7	8
Freq (Hz)	1.5167	7.3678	9.5083	10.7277	22.0883	26.5771	32.7402	37.0622

Table 4.1: Natural frequencies for the cantilevered beam model

To verify our expectation that the first three modes are sufficient for the analysis, we conducted the simulation with the first two modes, the first three modes, the first five modes and the first eight modes. Since we integrate the aerodynamics and structural dynamics in the time domain, we need the initial conditions. The initial conditions chosen

here are such that the general coordinates and their derivatives are zero. Under the effect of aerodynamic forces, the wing will undergo a "static" deformation or equilibrium deformation as well as a possible oscillation around this equilibrium position. The wing-tip deflection and the twist (or rotation) angle at the wing tip at 55 m/s freestream and 0.5 degrees angle of attack are shown in Fig 4-3.

From Figure 4-3, we can see that the oscillations of the wing-tip deflection and twist angle are decaying as time goes. The solution with the first three modes is very close to the solutions with more modes included. So, if there is no explicit statement otherwise, the following solutions are obtained by using the first three modes for the cantilever beam model.

The histories (functions of time) of the first three generalized modal coordinates, the wing-tip deflection and rotation as well as their FFT's are plotted in Figures 4-4 and 4-5. The airspeed is $55m/s$, and the angle of attack is 0.5 degrees. The modal amplitudes are decaying, eventually all have the same frequency although the wing is not in flutter. The change in frequency is most apparent in the history of q_3 around time 250. As one could expect, the high-frequency mode decays more rapidly than the low-frequency ones. But, because there is still an excitation due to the motion of the low-frequency modes, the low-frequency is noticeable in the later portion of the history. The modal coupling responsible for this common frequency is through the aerodynamic loads. If we plot a close-up for the first generalized coordinate q_1 and the wing-tip deflection u_3, we will see decaying oscillations as well, which are not apparent with the scale used in the plot. The power spectral densities (PSDs) of Fast Fourier Transform (FFT) for the histories between time steps 500 and 2000 confirm that all modes are decaying at the same frequency.

In Figure 4-6, the histories of the wing-tip motion are plotted for different airspeeds; it appears (more clearly in the twist perhaps) that somewhere between 95 m/s and 105 m/s the wing flutters. Precisely determining the lowest airspeed at which the motion does not decay is difficult. In part (b), the developing limit-cycle motion is evident for 95 m/s and 105 m/s.

In Figure 4-7, the histories are plotted for an airspeed of 105 m/s, clearly an airspeed at which the wing is experiencing a limit cycle oscillation (LCO). LCO's are characterized by constant amplitude and frequency. Again around time 250, we see (best perhaps in q_3) the frequency changing to the flutter frequency. Another important observation is that the the first mode, i.e., the flexural mode, is significantly out of phase from the second mode, i.e., the torsional mode, and so is the wing-tip deflection with respect to the wing-tip twist. This phase difference accounts for the occurrence of flutter in such a way that the energy can be absorbed by the wing from the airstream. Figure 4-8 shows the FFT's, which confirm that eventually all of the modes are synchronized at the same frequency as expected when the wing is in flutter. We give the phase portraits for the first three generalized modal coordinates in Figure 4-9, 4-10, and 4-11.

If the motion is truly a stable LCO, we would expect that different initial conditions eventually lead to the same motion. In Figures $4\text{-}12 - 4\text{-}16$, the solutions at the airspeed of 105 m/s with the initial condition of $q_1(0) = -10$, 0, and 10 and all the other initial conditions being zeroes are plotted at the same figure. It is clear that after an initial period, all the three cases settle down into the same motions.

4.5.3 HALE Aircraft Wing Mounted on a Free-to-Roll Sting at its Mid-span without a Center Mass

In this section, the rolling motion of the wing is included, but assume that the center located fuselage's mass moment of inertia is zero. The corresponding natural modes are very similar to those given in Figure 2-6. The natural frequencies for the symmetric modes are same as the case when the mass moment of inertia of the center mass, $I_F = 500$ $Kg\text{-}m^2$, while the ones for asymmetric modes are slightly higher.

To investigate the effects of the asymmetric modes, we give an initial velocity to the third mode which is the first asymmetric mode and keep the other initial conditions zero. Thus, the flow is no longer symmetric about the center-span plane, and the full-span wing has to be considered. Only the first six modes are used for the computation.

The time histories of the first six generalized modal coordinates are shown in Figure 4-17. The addition of the rolling motion certainly complicates the situation. At 55 m/s of airstream speed, the magnitude of the oscillations of all the modes is decaying. Some of them are approaching a steady state. Because there is no damping taken into account in the structural model, the damping effect comes only from the aerodynamics. This effect may not be sufficient to completely suppress the overall rolling motion. As a result, the rolling motion remains, but the oscillations superimposed on it are disappearing. At 75 m/s, the first mode and the unsymmetrical modes, i.e., the third and the fifth mode are growing, while the symmetric modes are decaying. At 95 m/s, the first mode and the unsymmetrical modes are growing, while the symmetric modes seem to reach periodic motions. At 105 m/s, all the modes are growing. This suggests that mounting a semi-span model on the wall will not give a true indication of the flutter speed. As a consequence of the rigidity added by the wall, the airspeed at flutter for a wall-mounted semi-model will be higher than that for the full-span model.

The FFT analyses shown in Figure 4-18 show that, no matter growing or decaying or periodic motion, all the modes respond at the same frequency once their motions settle through an initial transient period.

The time histories of the deflection and twist at both wing tips and the rolling angle are presented at Figure 4-19. We can see that the left wing tip experiences different motion from the right wing tip. At lower airspeed, the deflection and twist at both wing tips are decaying. Starting from somewhere between 75 m/s and 95 m/s airspeed, the elastic deformations at the left wing tip and the rolling angle begin to have growing oscillations, while the right wing tip's motion is still decaying, which indicates that the left semi-span wing is absorbing the energy from the airstream and the right semi-span wing is dumping the energy to the airstream at the same time.

4.5.4 HALE Aircraft Wing Mounted on a Free-to-Roll Sting at its Mid-span with a Center Mass

In this case, a center mass with moment of inertia of 500 $Kg\text{-}m^2$ is taken into account. The natural frequencies and natural mode shapes are given in Figure 2-6. We impose the same kind of initial conditions as in the previous section and run the simulation.

Numerical results are shown in Figure 4-20. At 55 m/s, 75 m/s and 95 m/s of airstream speed, the magnitude of the oscillations of all the modes is decaying. Especially at 95 m/s, all the modes except the first mode are very close to periodic motions. At 105 m/s, all the modes have growing oscillations. The rather heavy mass at F constrains the motion and almost acts as a wall; so that the asymmetric modes are nearly completely suppressed, the rolling motion decays, limit cycles develop, and generally the motion resembles that for the wall-mounted semi-span model.

The FFT analyses in Figure 4-21 also show that, no matter whether the motion is growing or decaying or periodic, all the modes respond at the same frequency once their motions get through an initial transient period.

Figure 4-22 shows the time histories of the deflection and twist at both wing tips and the rolling angle. The elastic deformations at both wing tips are very similar to each other at the given airspeeds. By comparing Figure 4-22 and Figure 4-19, it is further confirmed that the center mass constrains the motion so that the asymmetric modes are nearly completely suppressed.
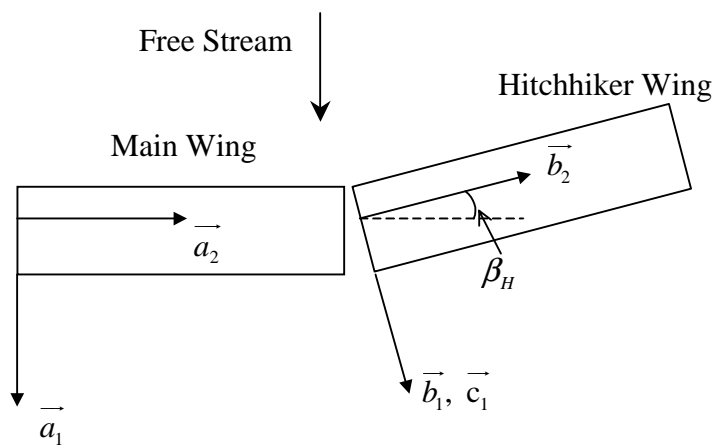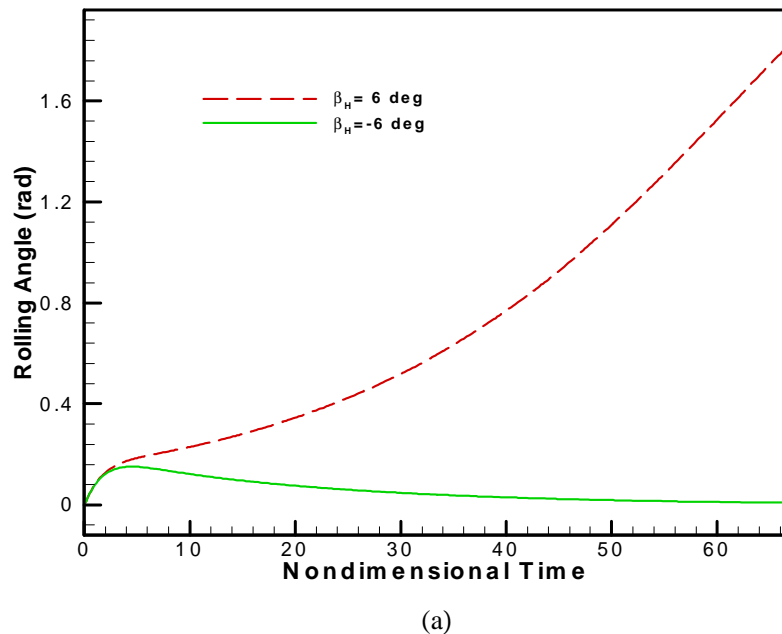
Figure 4-1: A schematic representation of the hitchhiking compound flight

(a)
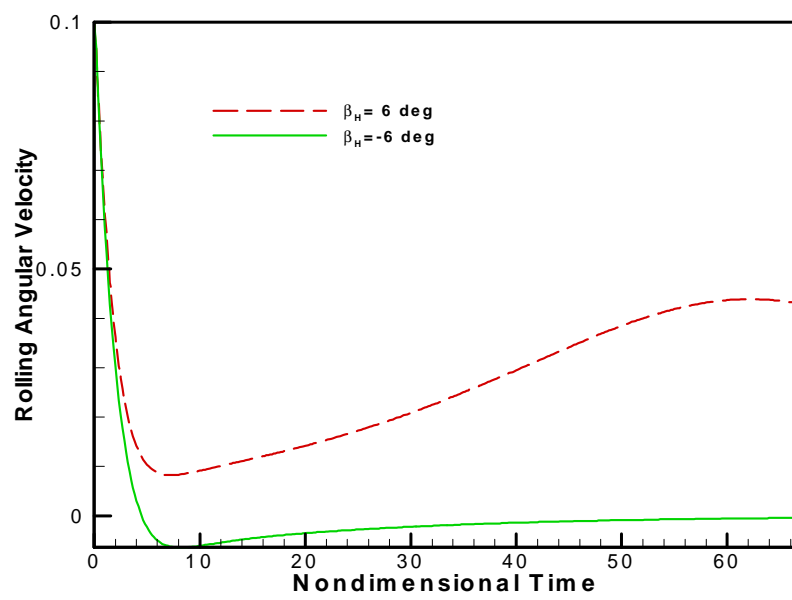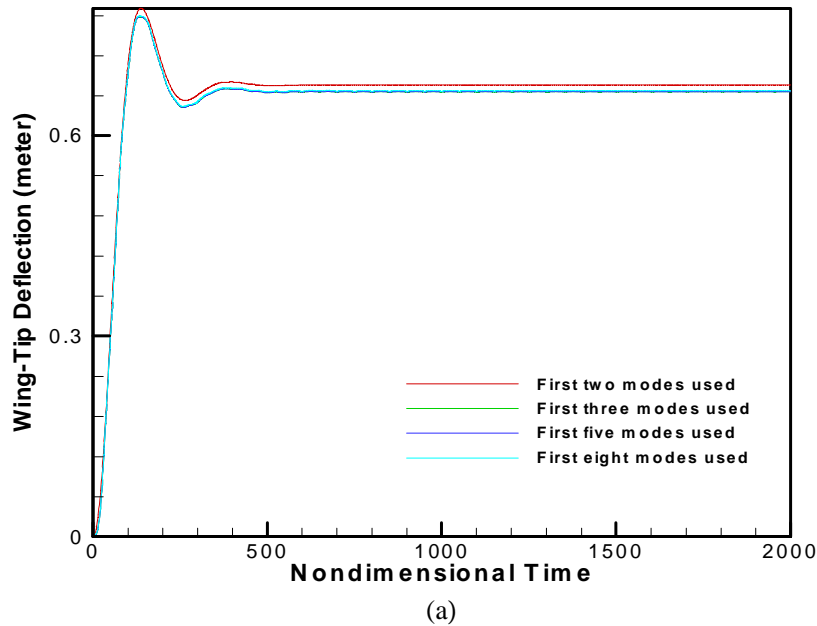
Figure 4-2: Time histories for the hitchhiker wing: (a) rolling angle, (b) rolling angluar velocity

(a)
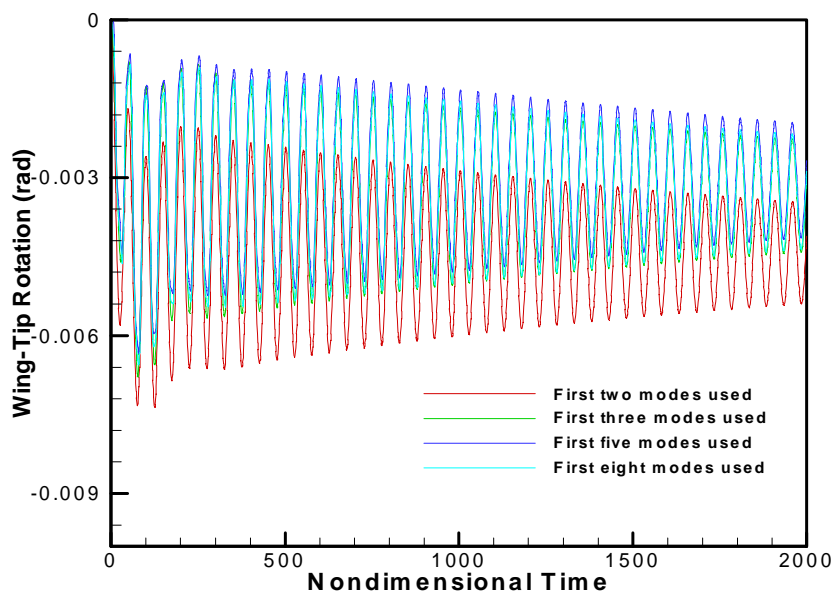
Figure 4-3: Wing-tip deformations at 55 m/s airspeed and 0.5 deg. angle of attack
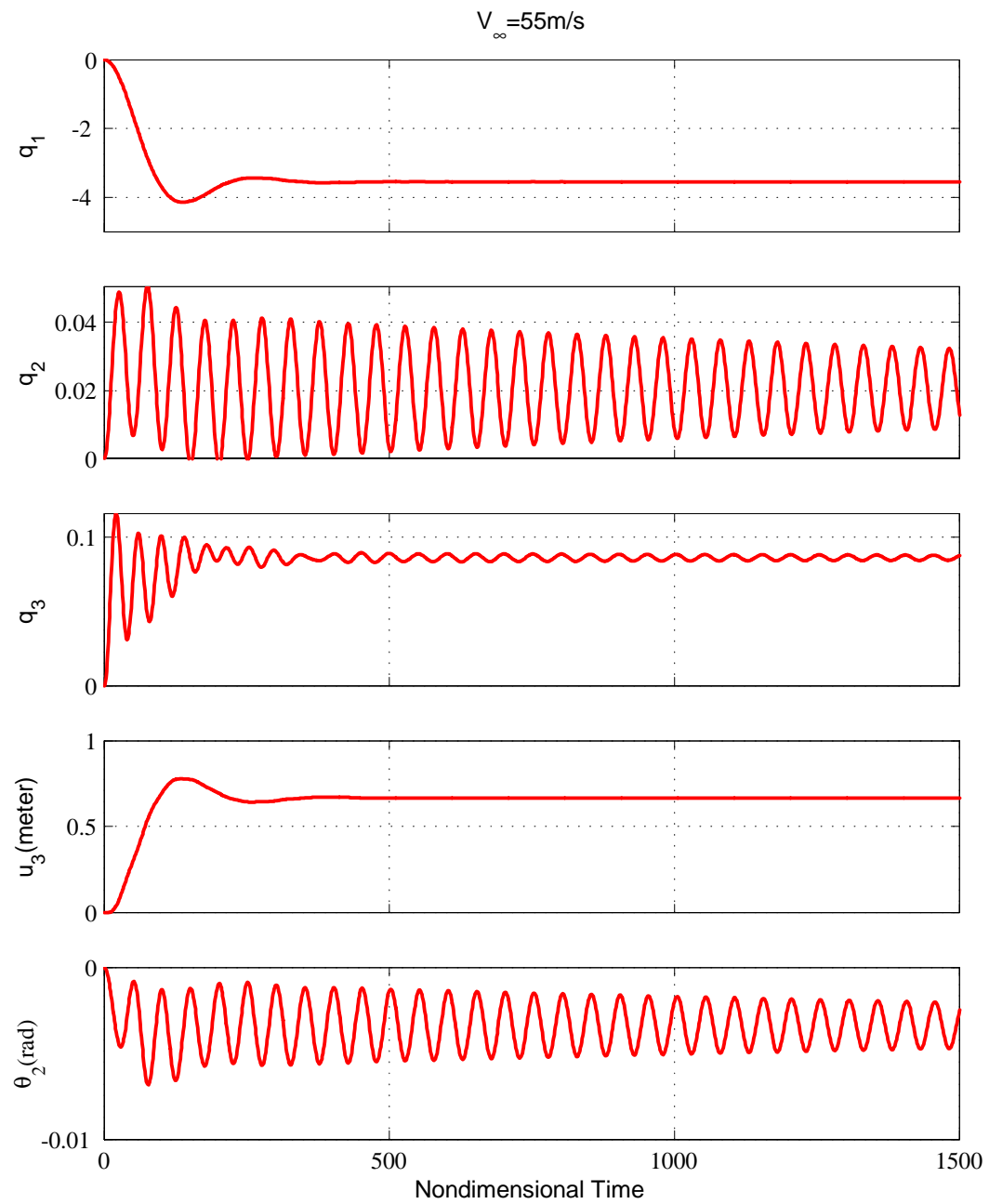
Figure 4-4: Time histories of the generalized modal coordinates and the wing-tip deformations at 55 m/s airspeed for the wing mounted on the wall of the tunnel
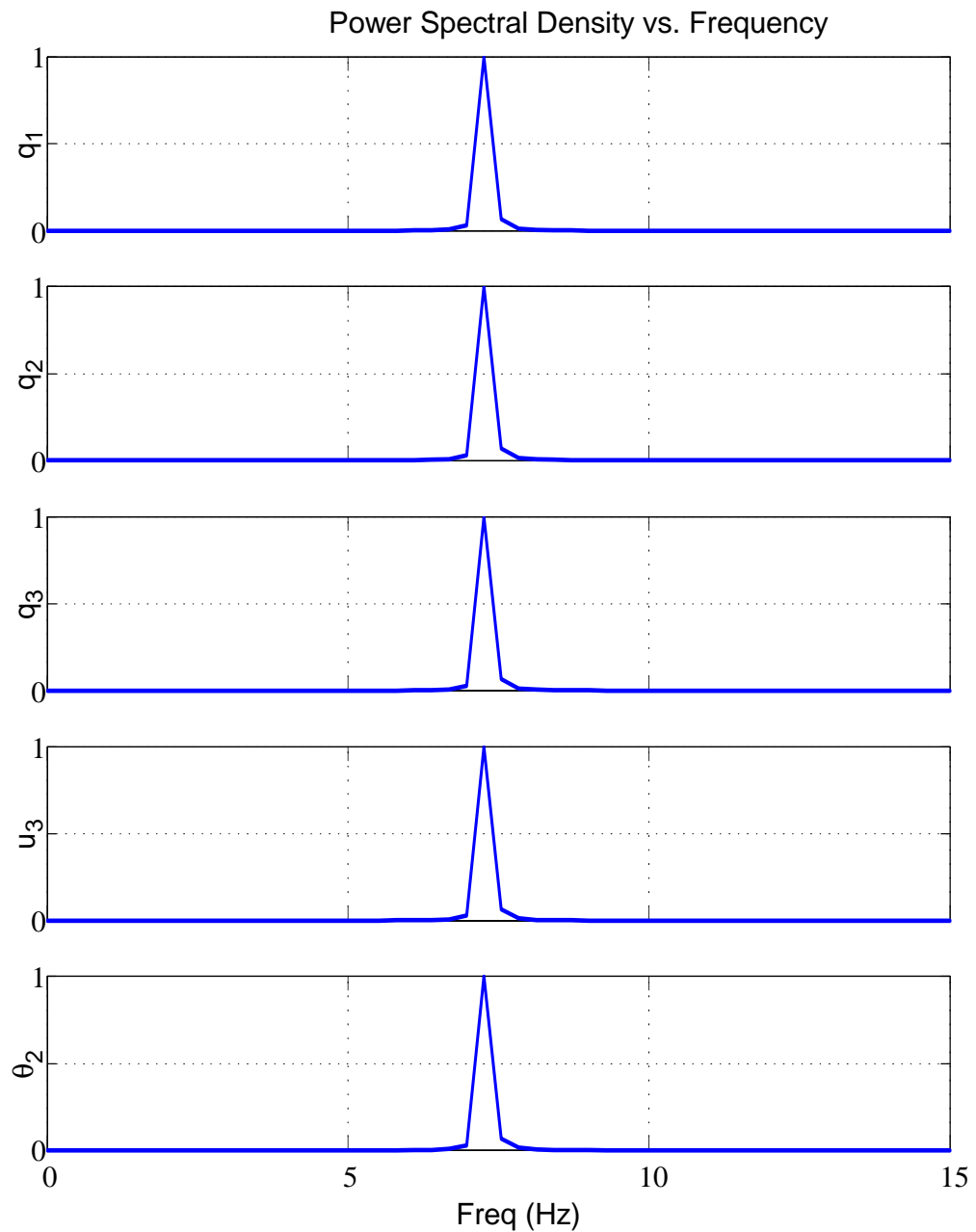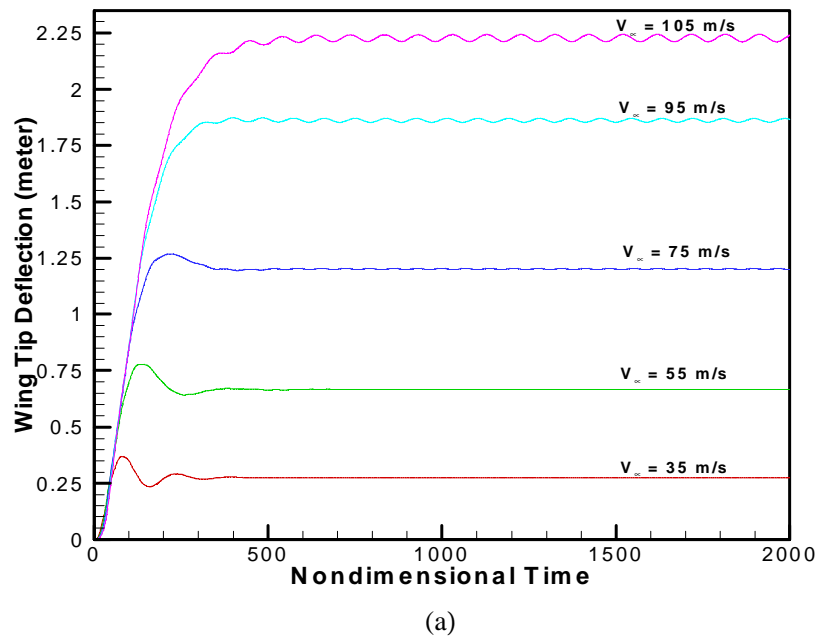
Figure 4-5: FFT's for the generalized modal coordinates and the wing tip deformations at 55 m/s airspeed for the wing mounted on the wall of the tunnel

(a)
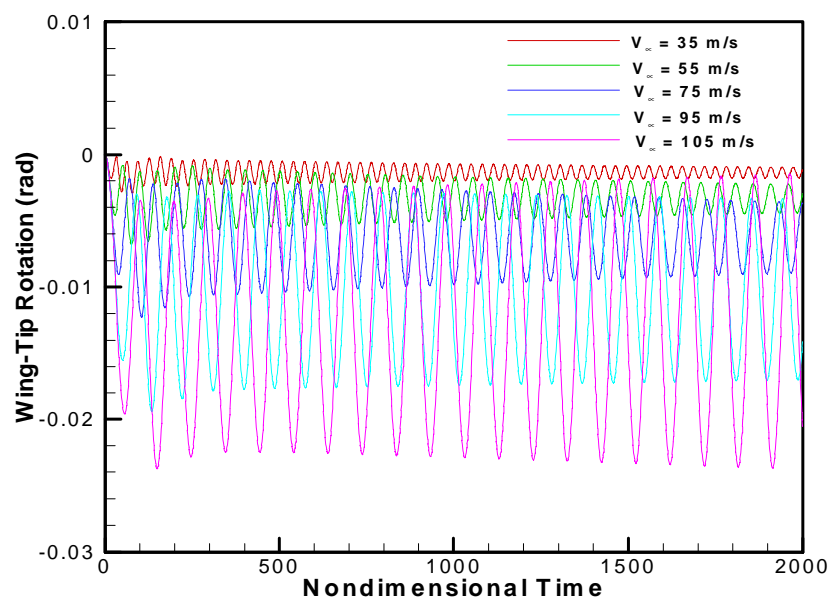
Figure 4-6: Time histories of the wing-tip (a) deflection, and (b) twist for several different airspeeds for the wing mounted on the wall of the tunnel

131
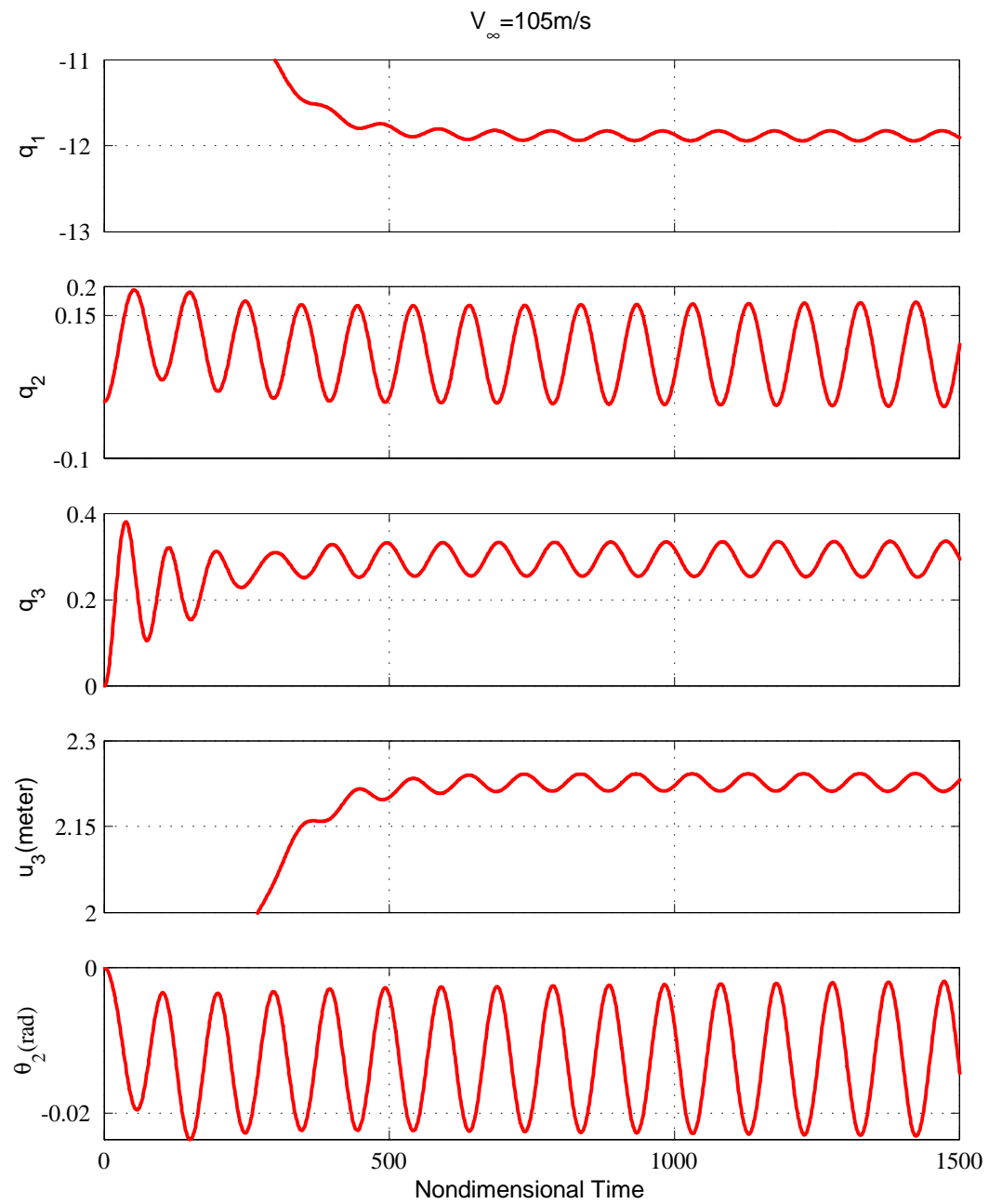
Figure 4-7: Time histories of the generalized modal coordinates and the wing-tip deformations at 105 m/s airspeed for the wing mounted on the wall of the tunnel
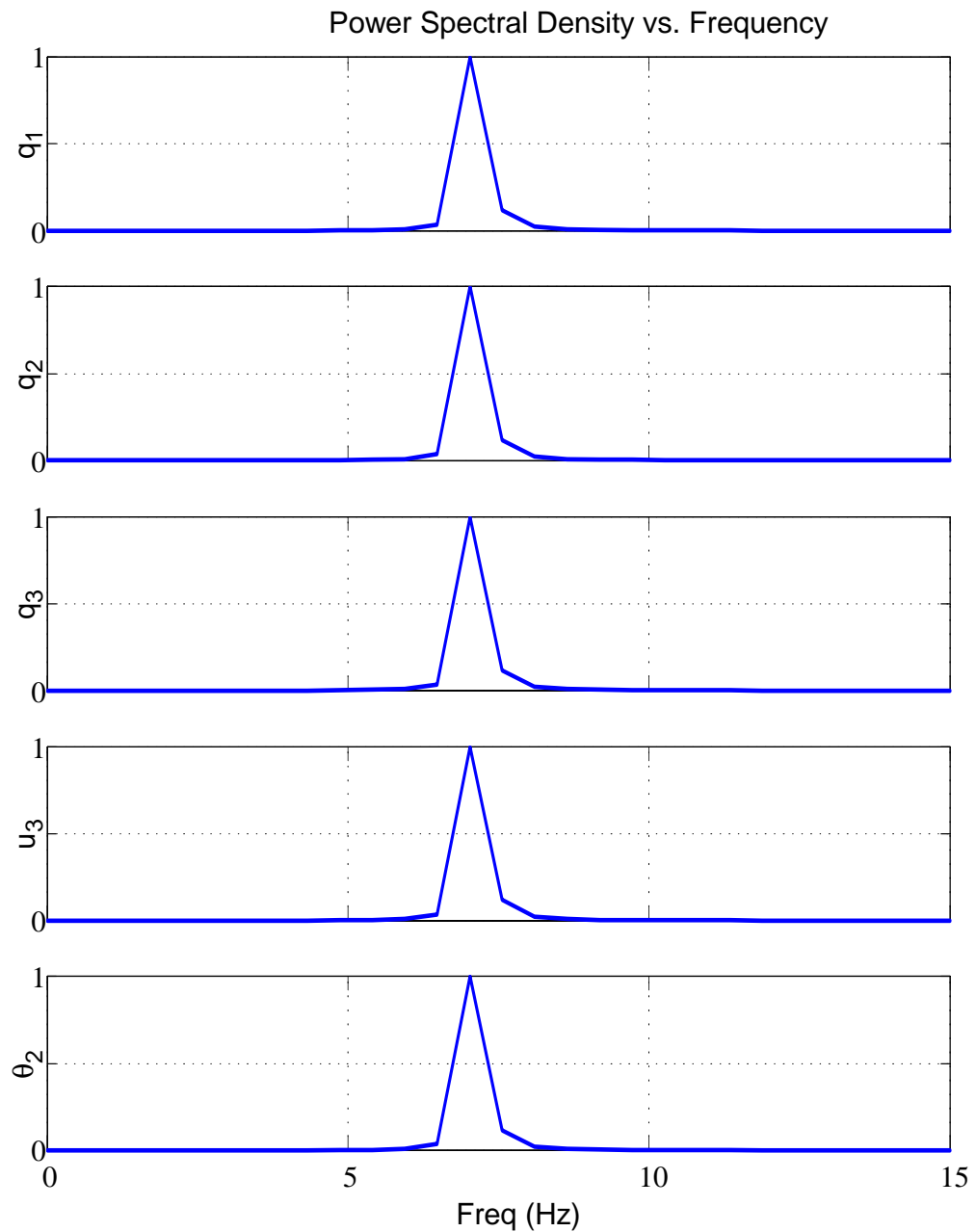
Figure 4-8: FFT's of the generalized modal coordinates and the wing tip deformations at 105 m/s airspeed for the wing mounted on the wall of the tunnel
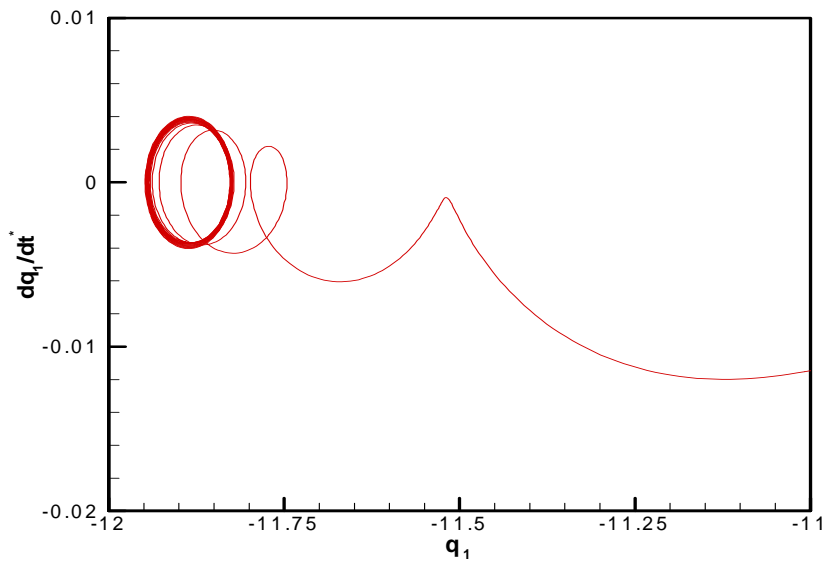
Figure 4-9: Phase portrait of the first generalized modal coordinate at 105 m/s airspeed for the wing mounted on the wall of the tunnel
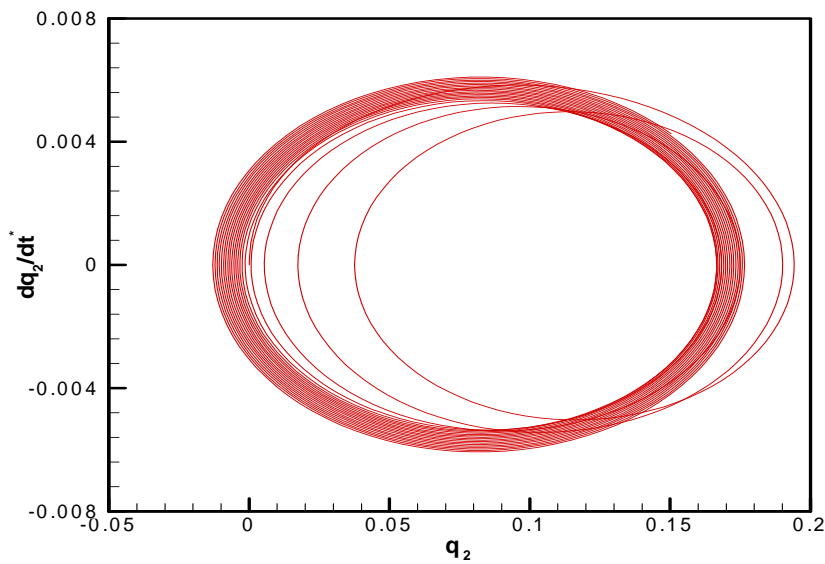
Figure 4-10: Phase portrait of the second generalized modal coordinate at 105 m/s airspeed for the wing mounted on the wall of the tunnel
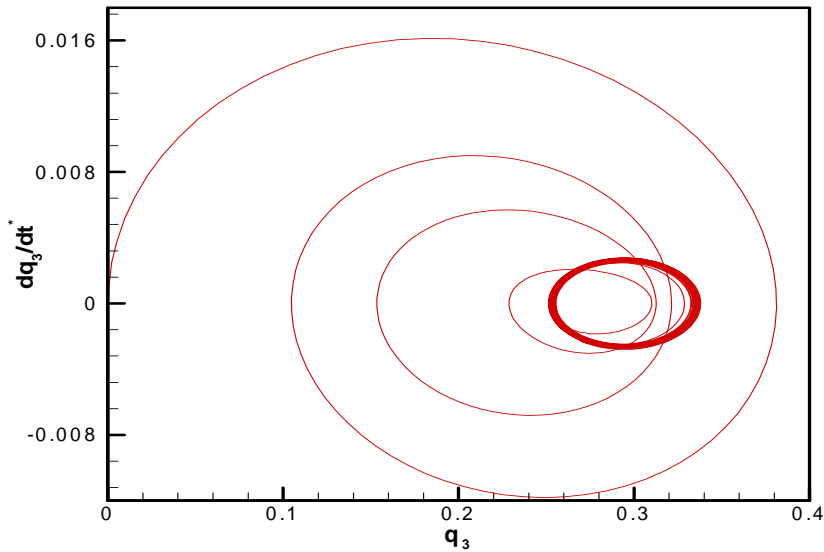
Figure 4-11: Phase portrait of the third generalized modal coordinate at 105 m/s airspeed for the wing mounted on the wall of the tunnel
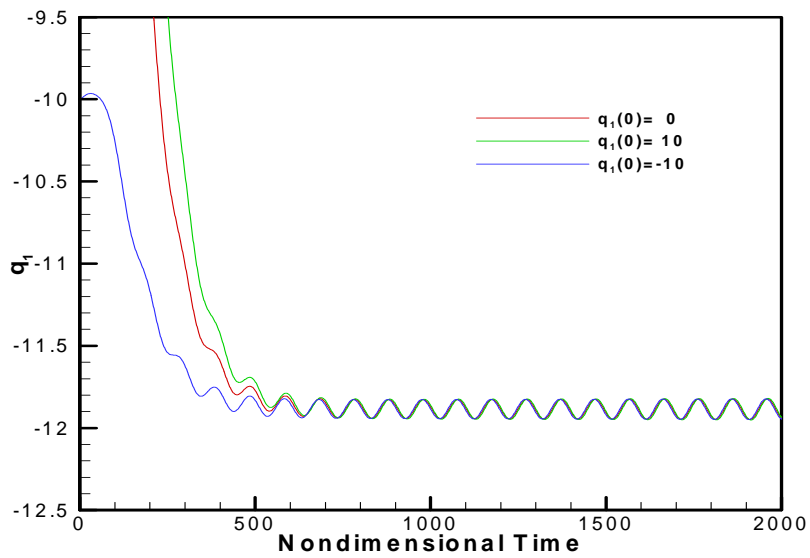
Figure 4-12: Time history of the first generalized modal coordinate for various initial conditions. $V_\infty = 105\ m/s$
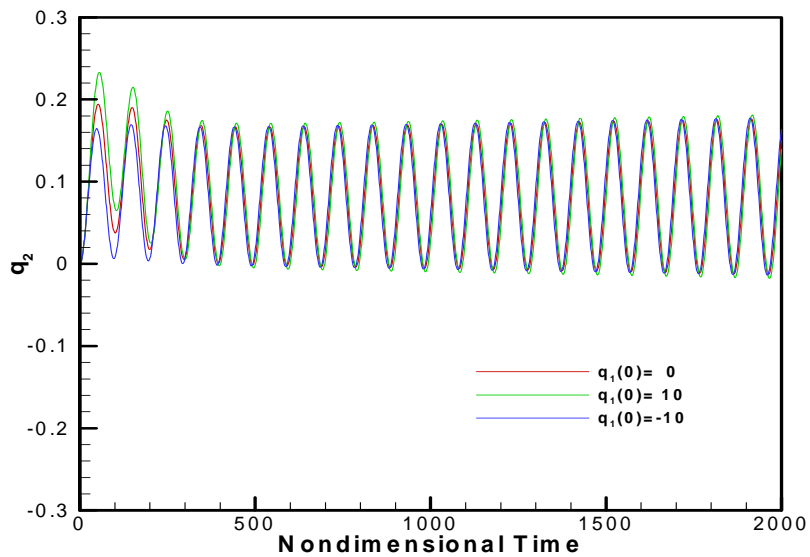
Figure 4-13: Time history of the second generalized modal coordinate for various initial conditions. $V_\infty = 105 \ m/s$
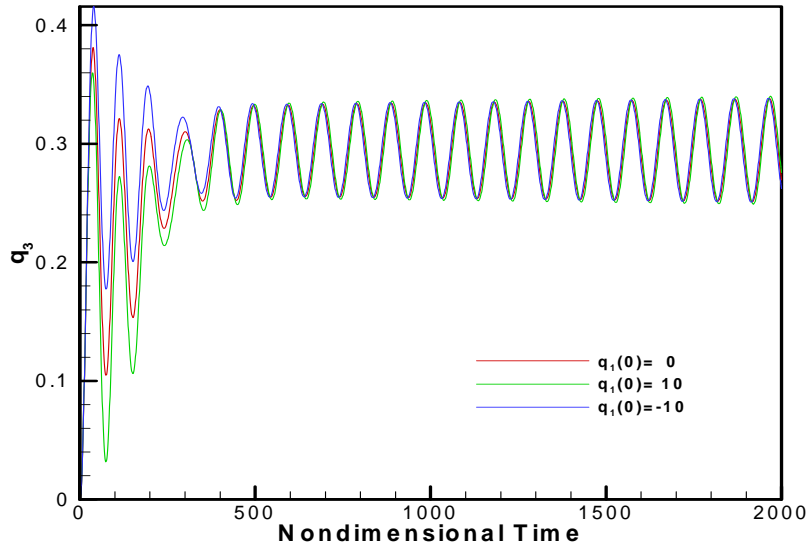
Figure 4-14: Time history of the third generalized modal coordinate for various initial conditions. $V_\infty = 105 \ m/s$

136
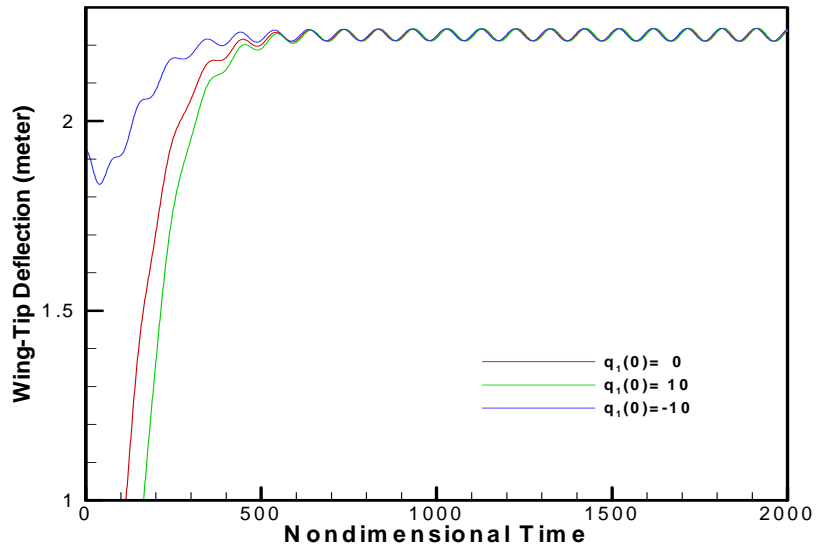
Figure 4-15: Time history of the wing-tip deflection for various initial conditions. $V_\infty = 105\ m/s$
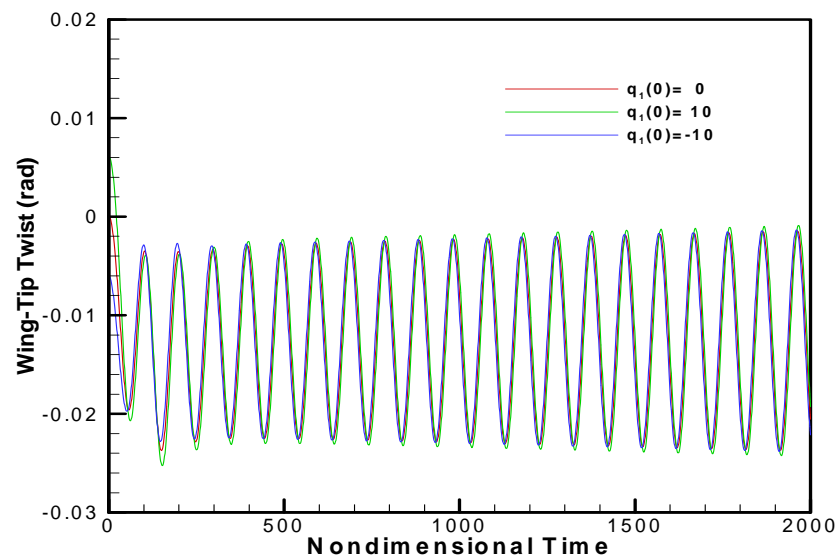
Figure 4-16: Time history of the wing-tip twist for various initial conditions. $V_\infty = 105\ m/s$

137
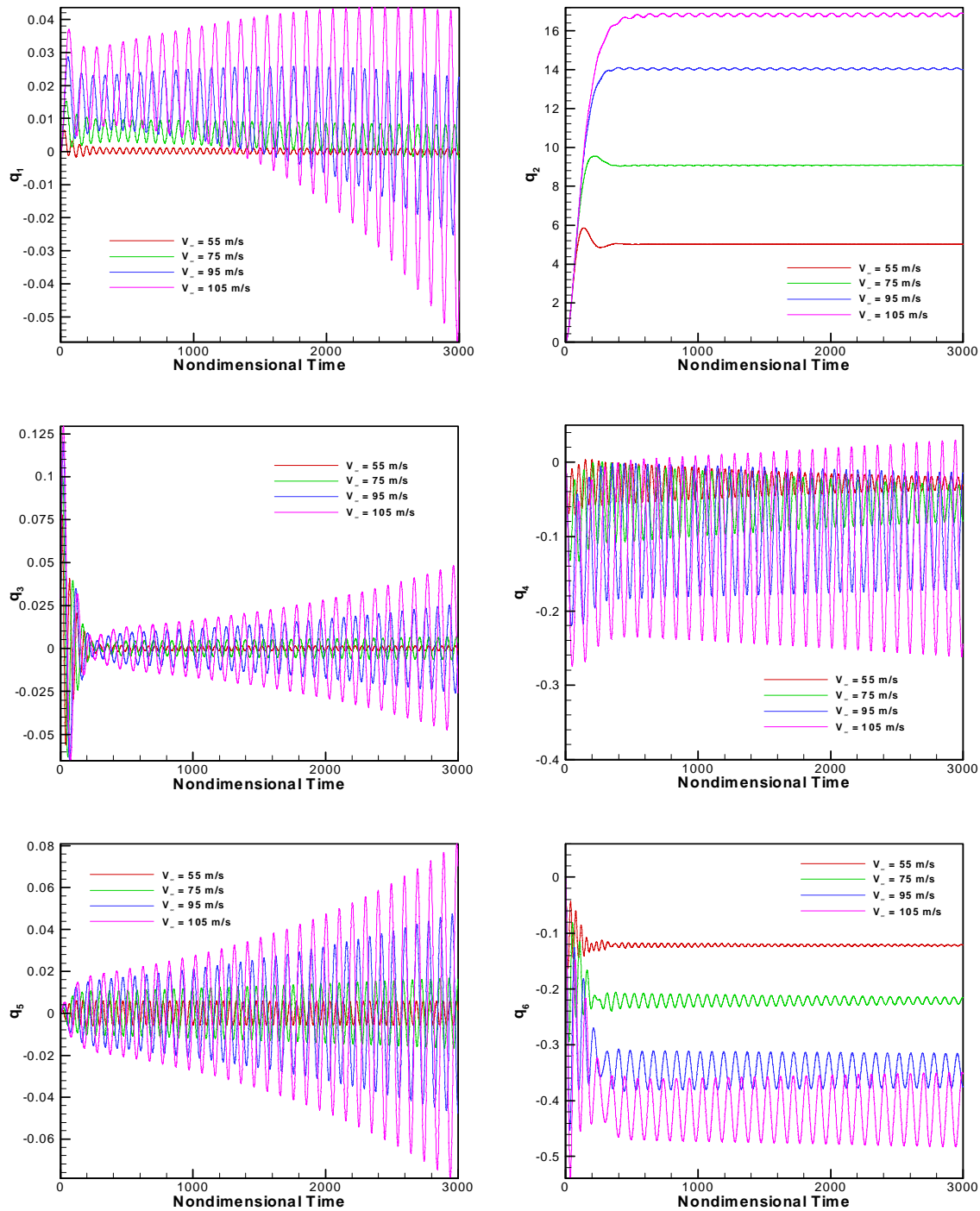
Figure 4-17: Time histories of the first six generalized modal coordinates for a full-span wing without a center mass
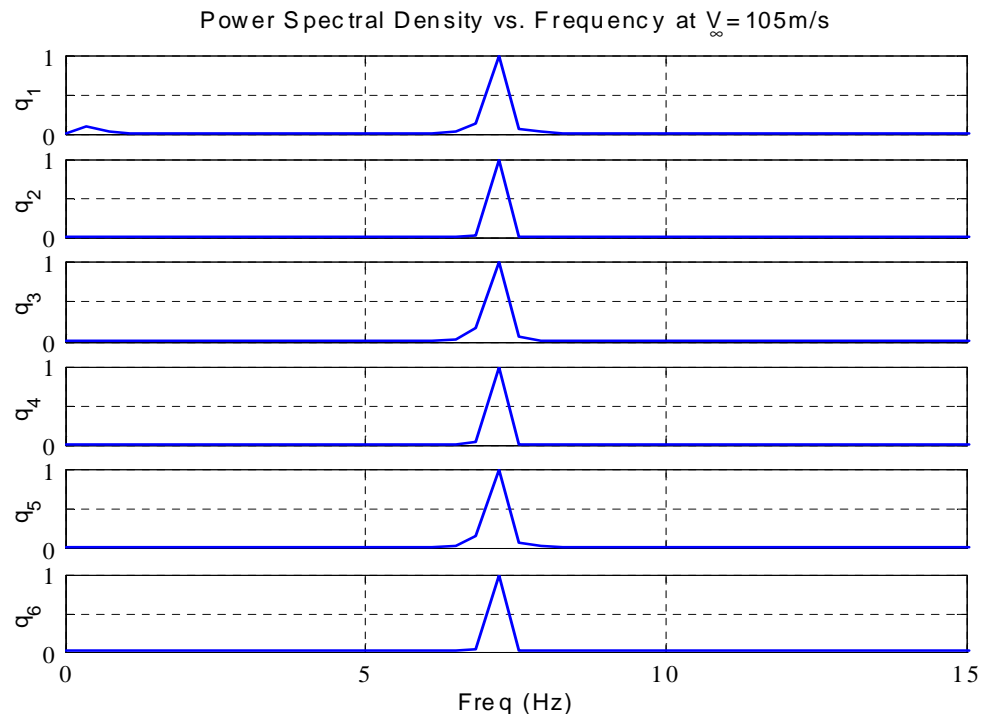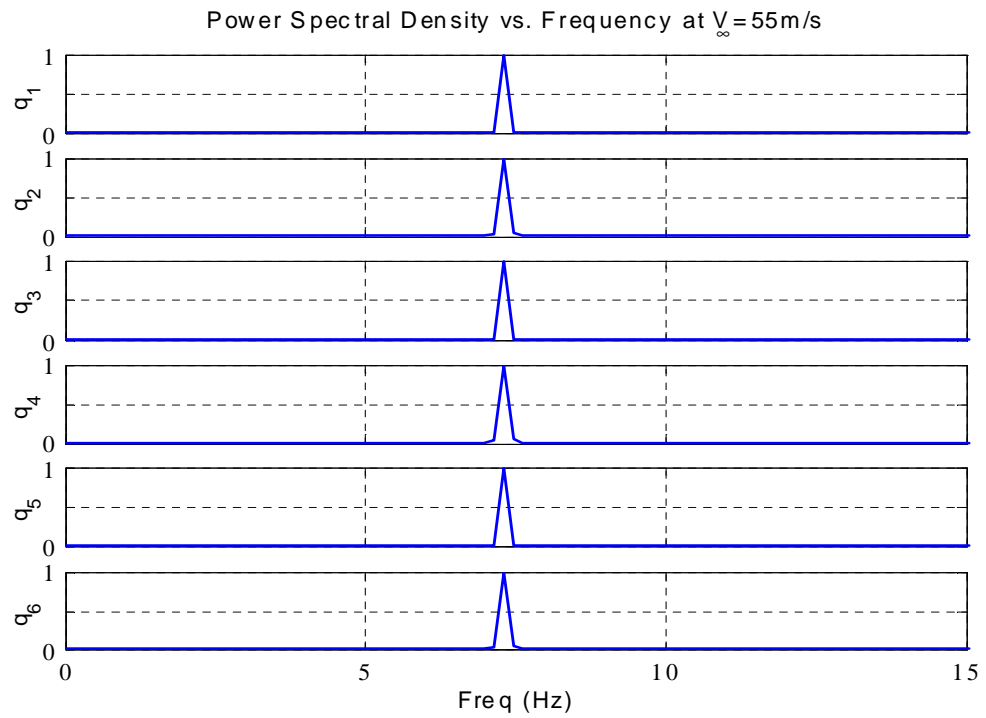
Figure 4-18: FFT's of the first six generalized modal coordinates of the full-span wing without a center mass
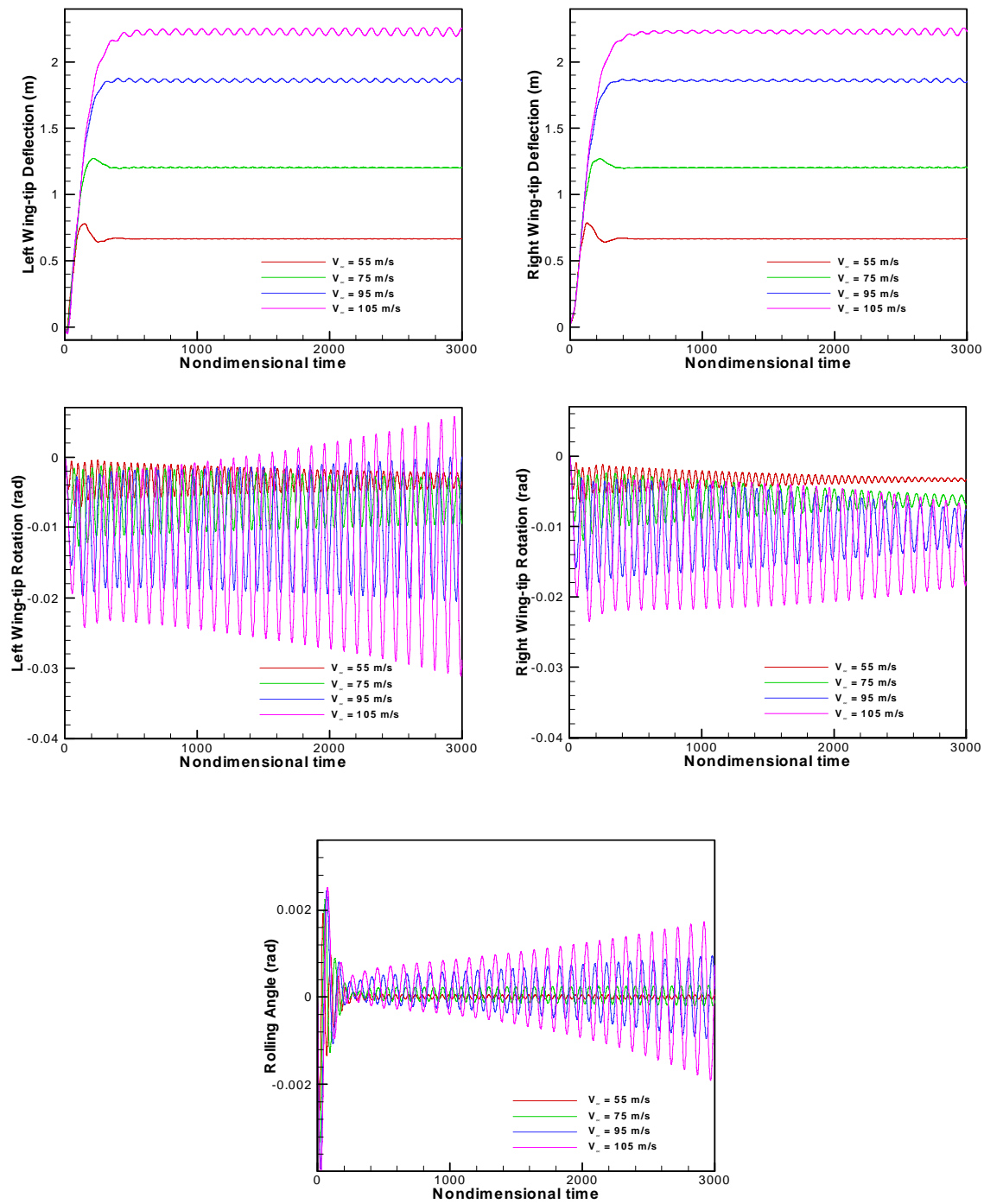
Figure 4-19: Time histories of the wing-tip deformations and the rolling angle for a full-span wing without a center mass
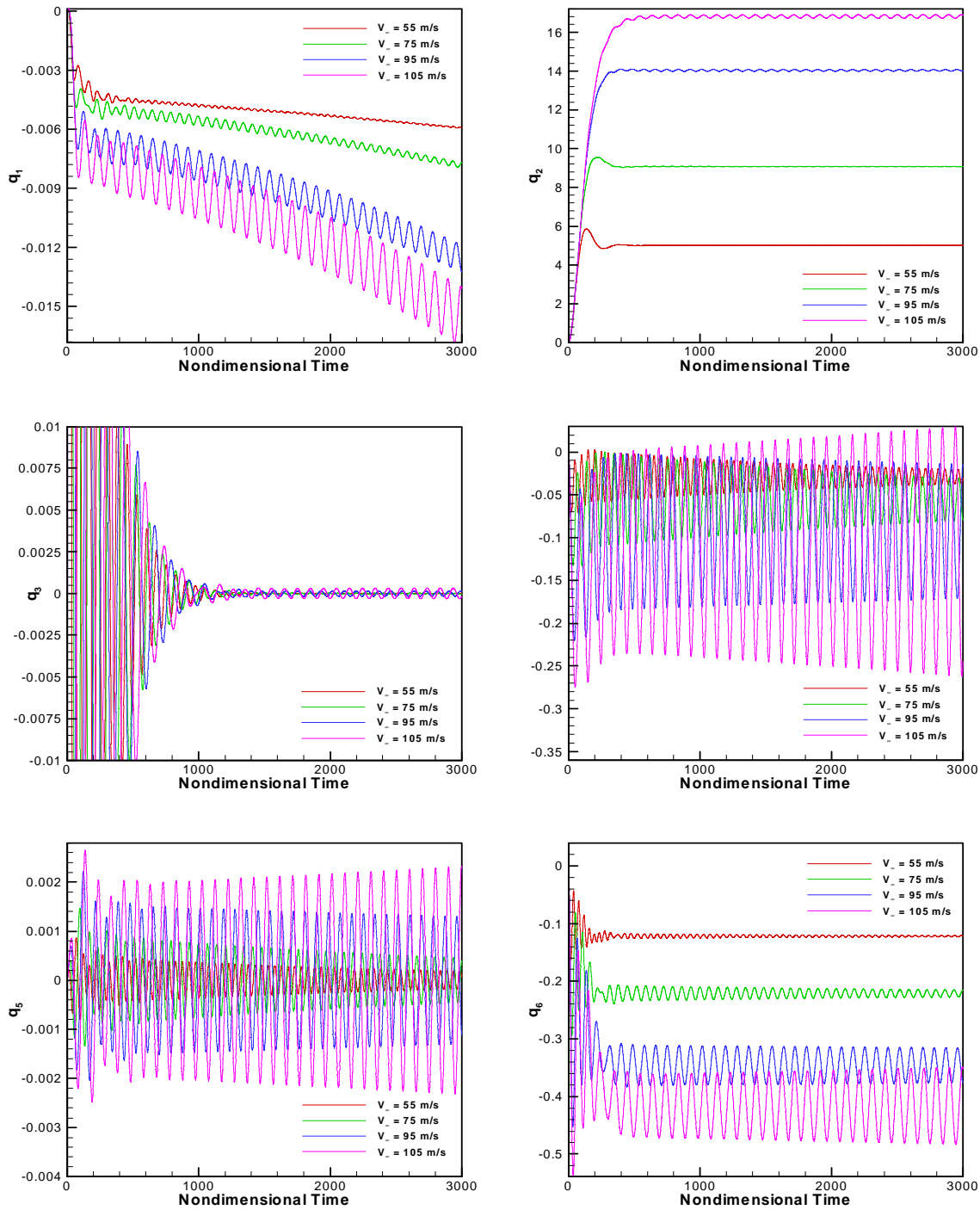
Figure 4-20: Time histories of the first six generalized modal coordinates for a full-span wing with a center mass
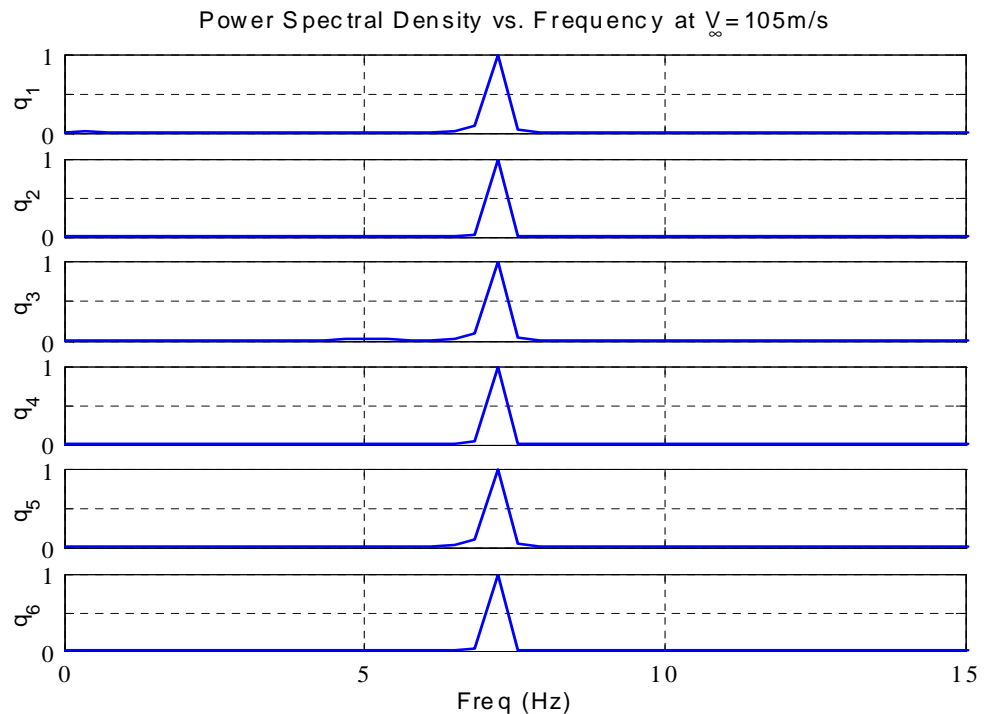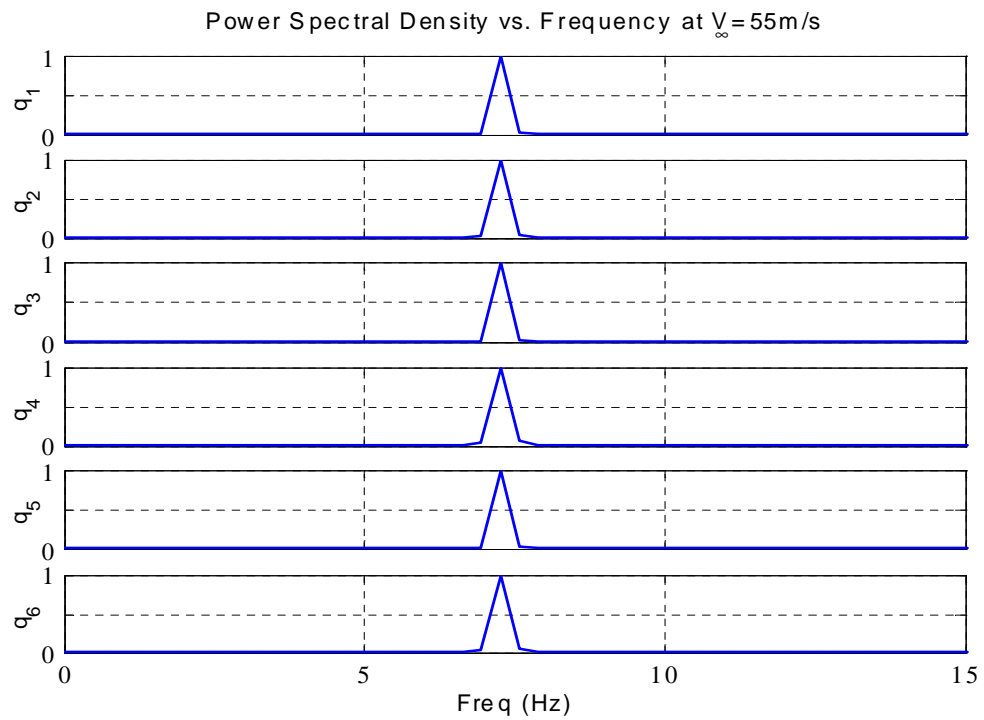
Figure 4-21: FFT's for the first six generalized modal coordinates of the full-span wing with a center mass
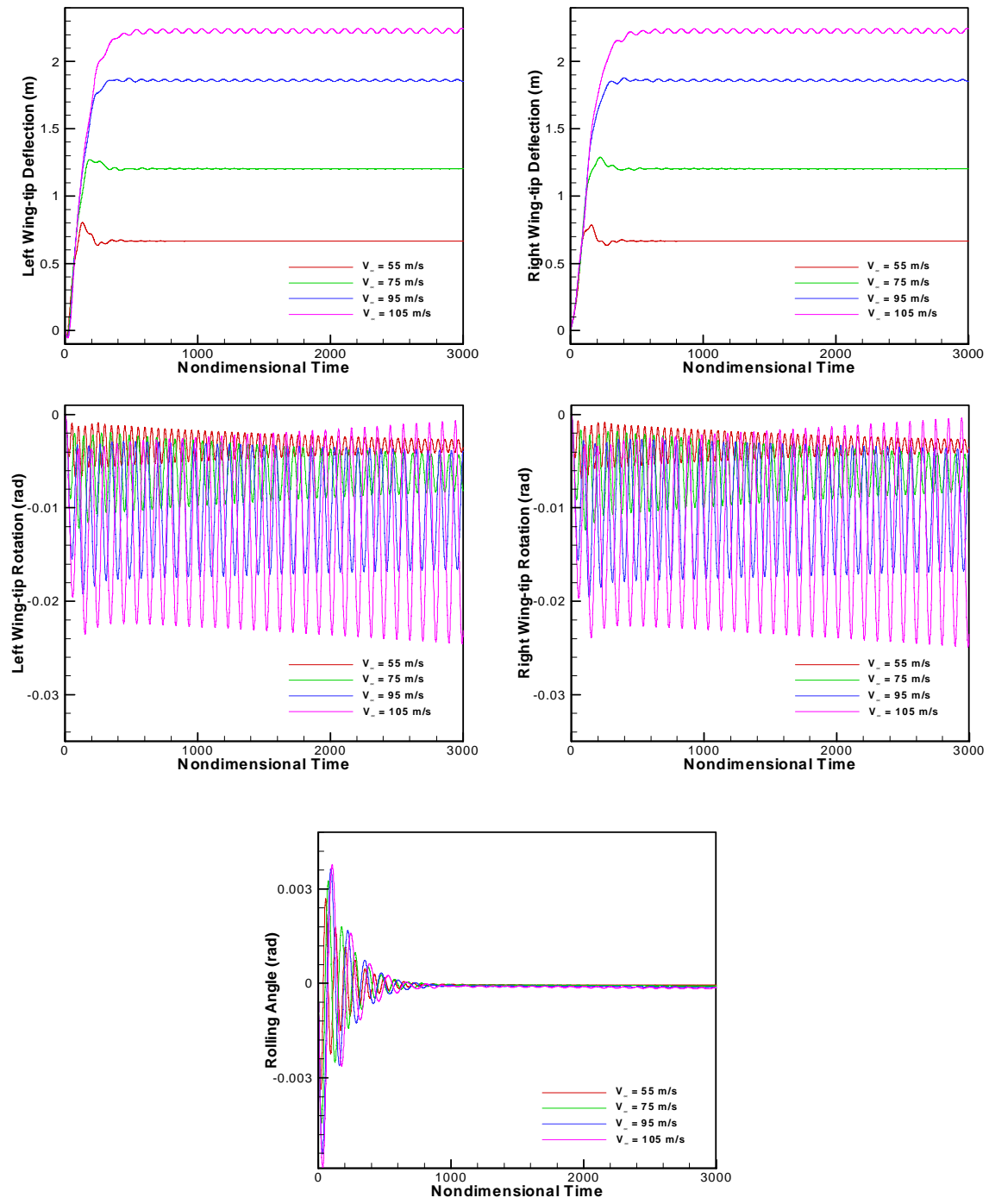
Figure 4-22: Time histories of the wing-tip deformations and the rolling angle for a full-span wing with a center mass

Chapter 5

Neural Network Control

In this chapter, we introduce a neural network control technique to suppress the flutter oscillations of a cantilever beam model for the wing.

5.1   Control Actuator

Different from the traditional use of ailerons or flaps to output the control signals, the control force is assumed to be given by an actuator that can apply a distributed torque along the spanwise direction of the wing. One example of this kind of actuator may be realized by a piezoelectric device embedded in the wing structure.

We also assume that the dynamics associated with the actuators is much faster than the system dynamics. The evenly distributed torque $\tau(t)$ is given by:

$$\tau(t) = Ku(t) \tag{5.1}$$

where the constant K defines the actuator gain factor, u is the input voltage to the actuator. u will be determined by a neural network predictive controller, which we will discuss in the next sections. We first describe how we get the generalized control force vector $\{F_c\}$ in Equation (4.2).

Regarding the governing equations, the controller produces the following forces:

$$f_{u_1} = 0, \ f_{u_2} = 0, \ f_{u_3} = 0, \ m_{\theta_2} = \tau \qquad (5.2)$$

On a typical finite element with element length h_e, the equivalent nodal force generated by the controller would be:

$$\{F_{\theta_2}\}^e = \int_{y_i}^{y_j} m_{\theta_2} \left\{ \begin{array}{c} N_i \\ N_j \end{array} \right\} dy = \left\{ \begin{array}{c} \frac{1}{2} \\ \frac{1}{2} \end{array} \right\} h_e \tau \qquad (5.3)$$

With that we could construct the generalized control force vector $\{F_c\}$ by combining all of the elemental nodal forces. As an example, for an even distributed finite element mesh:

$$\{F_c\} = [\ 0 \ \ 0 \ \ 0 \ \ 0 \ \ \tfrac{1}{2} \ \ 0 \ | \ 0 \ \ 0 \ \ 0 \ \ 0 \ \ 1 \ \ 0 \ | \qquad (5.4)$$
$$\cdots \ \ 0 \ \ 0 \ \ 0 \ \ 0 \ \ 1 \ \ 0 \ | \ 0 \ \ 0 \ \ 0 \ \ 0 \ \ \tfrac{1}{2} \ \ 0 \ ]^T h_e \tau$$

These control forces will also affect the bending modes through the modal matrix $[\boldsymbol{\varphi}]$ due to the inertial coupling between bending and torsion.

5.2 Description of Neural Network Predictive Control

Neural networks have been applied very successfully in the identification and control of dynamic systems. That has been largely contributed by the universal approximation capability possessed by the multi-layer networks. In the neural network predictive control (NNPC) technique, the controller uses a neural network model to predict future plant response to potential control signals. A search algorithm is used to select the best control input that optimize future plant performance. Obviously, NNPC requires several steps in its application. The first step is to determine the neural network plant model, which

is typically called system identification. Next, the network plant model is used by the controller to predict future performance.

5.2.1 System Identification

A simplified block diagram of the system-identification process is shown in Figure 5-1, where u denotes the control input to the plant, y_p represents the output of the plant, and y_m represents the output of the neural network plant model. The prediction error between the plant output and the neural network output is used for the neural network training.

We choose a two layer neural network shown in Figure 5-2, which consists of an input layer and an output layer, to represent the forward dynamics of the plant. Sometimes, the layers other than the output layer are also called hidden layers. The inputs of the network consist of the current and previous control signals and previous plant outputs.

The input layer shown in Figure 5-2 includes R_1 control input signals comprising input vector $\mathbf{u}$, R_2 previous plant outputs comprising input vector $\mathbf{y}_p$, and S neurons. R_1 and R_2 represents the order of the delay of the control input signals and the plant outputs, respectively. In vector notation, we have

$$\mathbf{u} = \left\{ \begin{array}{c} u\left(t\right) \\ \vdots \\ u\left(t - \left(R_1 - 1\right)\Delta t\right) \end{array} \right\}, \quad \mathbf{y}_p = \left\{ \begin{array}{c} y_p\left(t - \Delta t\right) \\ \vdots \\ y_p\left(t - R_2\Delta t\right) \end{array} \right\} \tag{5.5}$$

Each element of the input vector $\mathbf{u}$ is connected to each neuron through the weight matrix $\mathbf{W}^{(1,1)}$, while each element of the input vector $\mathbf{y}_p$ is connected to each neuron through the weight matrix $\mathbf{W}^{(1,2)}$. Each neuron has a bias $b_i^{(1)}$, a summer, a transfer function f and an output $a_i^{(1)}$. Taken together, the outputs form the output vector $\mathbf{a}^{(1)}$. It is common for the number of inputs to a layer to be different from the number of neurons.

The input weight matrix, through which the input vector elements enter the network,

146

has the following form:

$$\mathbf{W}^{(1,1)} = \begin{bmatrix} W_{1,1}^{(1,1)} & W_{1,2}^{(1,1)} & \cdots & W_{1,R_1}^{(1,1)} \\ W_{2,1}^{(1,1)} & W_{2,2}^{(1,1)} & \cdots & W_{2,R_1}^{(1,1)} \\ \vdots & \vdots & & \vdots \\ W_{S,1}^{(1,1)} & W_{S,2}^{(1,1)} & \cdots & W_{S,R_1}^{(1,1)} \end{bmatrix} \tag{5.6}$$

$$\mathbf{W}^{(1,2)} = \begin{bmatrix} W_{1,1}^{(1,2)} & W_{1,2}^{(1,2)} & \cdots & W_{1,R_2}^{(1,2)} \\ W_{2,1}^{(1,2)} & W_{2,2}^{(1,2)} & \cdots & W_{2,R_2}^{(1,2)} \\ \vdots & \vdots & & \vdots \\ W_{S,1}^{(1,2)} & W_{S,2}^{(1,2)} & \cdots & W_{S,R_2}^{(1,2)} \end{bmatrix} \tag{5.7}$$

As noted previously, the row indices of the elements of matrix $\mathbf{W}^{(1,1)}$ and $\mathbf{W}^{(1,2)}$ indicate the destination neuron associated with that weight, while the column indices indicate the source of the input for that weight. Thus, the indices in $W_{3,2}^{(1,1)}$ mean that this weight represents the connection to the third neuron from the second source of input vector $\mathbf{u}$; while the indices in $W_{3,2}^{(1,2)}$ mean that this weight represents the connection to the third neuron from the second source of the input vector $\mathbf{y}_p$.

The output layer only has one neuron with bias $b^{(2)}$ but S input data. The output vector of the input layer $\mathbf{a}^{(1)}$ enter the output layer by a $1 \times S$ weight matrix $\mathbf{W}^{(2,1)}$:

$$\mathbf{W}^{(2,1)} = \begin{bmatrix} W_1^{(2,1)} & W_2^{(2,1)} & \cdots & W_S^{(2,1)} \end{bmatrix} \tag{5.8}$$

The transfer function in the first layer of the neural network is chosen to be the so-called squashing function, the Hyperbolic Tangent Sigmoid function. This transfer function takes the input, which may have any value between plus and minus infinity, and squashes the output into the range -1 to 1. Another reason for this choice is in part because this function is differentiable. The transfer function in the second layer is set to be the linear transfer function. Thus, with the illustration in Figure 5-2, it's easy to get:

$$n_i^{(1)} = \sum_{j=1}^{R_1} W_{ij}^{(1,1)} \, u_j \; + \; \sum_{j=1}^{R_2} W_{ij}^{(1,2)} \, y_{pj} + b_i^{(1)} \qquad \text{for } i = 1, 2, \cdots, S \qquad (5.9)$$

$$a_i^{(1)} = \tanh\left(n_i^{(1)}\right) \qquad \text{for } i = 1, 2, \cdots, S \qquad (5.10)$$

and

$$n^{(2)} = \sum_{j=1}^{S} W_j^{(2,1)} \, a_j^{(1)} + b^{(2)} \qquad (5.11)$$

$$a^{(2)} = purelin\left(n^{(2)}\right) = n^{(2)} \qquad (5.12)$$

The predicted plant output at time t by the neural network would be given in a concise notation as:

$$y_m\left(t\right) = a^{(2)} = \mathbf{W}^{(2,1)} \cdot \tanh\left(\mathbf{W}^{(1,1)} \cdot \mathbf{u} + \mathbf{W}^{(1,2)} \cdot \mathbf{y}_p + \mathbf{b}^{(1)}\right) + b^{(2)} \qquad (5.13)$$

When the neural network is given appropriate weights and biases, it provides the desired outputs. The process to get the proper set of the weight matrixes and the biases is called the training or learning of the network. The backpropagation algorithm is one typical choice.

Backpropagation

Backpropagation was created by generalizing the Widrow-Hoff learning rule to multiple-layer networks and nonlinear differentiable transfer functions. It finds the weights and bias of the network by minimizing the performance index, the mean square error. The algorithm is provided with a series of examples of proper network behavior:

$$\{\mathbf{p}_1, T_1\}, \; \{\mathbf{p}_2, T_2\}, \; \cdots, \; \{\mathbf{p}_Q, T_Q\} \qquad (5.14)$$

where $\mathbf{p}_q$ $(q = 1, 2, \cdots, Q)$ is an input vector to the network, which consists of $\mathbf{u}$ and $\mathbf{y}_p$ in the network shown in Figure 5-2, and T_q $(q = 1, 2, \cdots, Q)$ is the corresponding target output, which is the real output of the plant. As each input is applied to the network, the output of the network, $a^{(2)}$, is compared to the target, T. The mean square error is defined as:

$$F\left(\mathbf{x}\right) = e^2 = \left(T - a^{(2)}\right)^2 \tag{5.15}$$

where $\mathbf{x}$ is the vector of the weights and biases of the network. With a different set of weights and biases, there will be a different output from the network and, thus, a different mean square error. The mean square error is approximated at iteration k as:

$$\widehat{F}\left(\mathbf{x}\right) = e\left(k\right)^2 = \left(T\left(k\right) - a^{(2)}\left(k\right)\right)^2 \tag{5.16}$$

The weights and biases are updated at each iteration by the gradient descent algorithm:

$$W_{i,j}^{(m,n)}\left(k+1\right) = W_{i,j}^{(m,n)}\left(k\right) + \Delta W_{i,j}^{(m,n)}\left(k\right) \qquad m, n = 1, 2 \tag{5.17}$$

$$b_i^{(m)}\left(k+1\right) = b_i^{(m)}\left(k\right) + \Delta b_i^{(m)}\left(k\right) \qquad m = 1, 2 \tag{5.18}$$

where

$$\Delta W_{i,j}^{(m,n)}\left(k\right) = -\alpha \frac{\partial \widehat{F}}{\partial W_{i,j}^{(m,n)}} \tag{5.19}$$

$$\Delta b_i^{(m)}\left(k\right) = -\alpha \frac{\partial \widehat{F}}{\partial b_i^{(m)}} \tag{5.20}$$

and α is the learning rate and is a heuristic constant.

The term backpropagation refers to the manner in which the gradient is computed. Because the error is an indirect function of the weights in the hidden layer (input layer), the chain rule of calculus is used to calculate the derivatives:

$$\frac{\partial \widehat{F}}{\partial W_{i,j}^{(m,n)}} = \frac{\partial \widehat{F}}{\partial n_i^{(m)}} \frac{\partial n_i^{(m)}}{\partial W_{i,j}^{(m,n)}} \tag{5.21}$$

$$\frac{\partial \widehat{F}}{\partial b_i^{(m)}} = \frac{\partial \widehat{F}}{\partial n_i^{(m)}} \frac{\partial n_i^{(m)}}{\partial b_i^{(m)}} \tag{5.22}$$

where $\frac{\partial \widehat{F}}{\partial n_i^{(m)}}$ is commonly called as the sensitivity $s_i^{(m)}$, i.e.,

$$s_i^{(m)} = \frac{\partial \widehat{F}}{\partial n_i^{(m)}} \tag{5.23}$$

which represents the sensitivity of $\widehat{F}$ to the changes in the i-th element of the network input at Layer m. Note that there is no repeated index summation implication.

We first consider Layer 2, i.e., $m = 2$. We have

$$\frac{\partial \widehat{F}}{\partial W_j^{(2,1)}} = \frac{\partial \widehat{F}}{\partial n^{(2)}} \frac{\partial n^{(2)}}{\partial W_j^{(2,1)}}, \qquad (j = 1, 2, \cdots S) \tag{5.24}$$

$$\frac{\partial \widehat{F}}{\partial b^{(2)}} = \frac{\partial \widehat{F}}{\partial n^{(2)}} \frac{\partial n^{(2)}}{\partial b^{(2)}} \tag{5.25}$$

From Equation (5.11), we obtain

$$\frac{\partial n^{(2)}}{\partial W_j^{(2,1)}} = a_j^{(1)}, \qquad (j = 1, 2, \cdots S) \tag{5.26}$$

and
$$\frac{\partial n^{(2)}}{\partial b^{(2)}} = 1 \tag{5.27}$$

Substituting the above two equations into (5.24) and (5.25), and considering

$$s^{(2)} = \frac{\partial \widehat{F}}{\partial n^{(2)}} = 2e\frac{\partial e}{\partial n^{(2)}} = -2e\frac{\partial a^{(2)}}{\partial n^{(2)}} = -2e \tag{5.28}$$

yields
$$\frac{\partial \widehat{F}}{\partial W_j^{(2,1)}} = -2ea_j^{(1)}, \qquad (j = 1, 2, \cdots S) \tag{5.29}$$

$$\frac{\partial \widehat{F}}{\partial b^{(2)}} = -2e \tag{5.30}$$

For Layer 1, we have

$$\frac{\partial \widehat{F}}{\partial W_{i,j}^{(1,1)}} = \frac{\partial \widehat{F}}{\partial n_i^{(1)}} \frac{\partial n_i^{(1)}}{\partial W_{i,j}^{(1,1)}} \qquad (5.31)$$

$$\frac{\partial \widehat{F}}{\partial W_{i,j}^{(1,2)}} = \frac{\partial \widehat{F}}{\partial n_i^{(1)}} \frac{\partial n_i^{(1)}}{\partial W_{i,j}^{(1,2)}} \qquad (5.32)$$

$$\frac{\partial \widehat{F}}{\partial b_i^{(1)}} = \frac{\partial \widehat{F}}{\partial n_i^{(1)}} \frac{\partial n_i^{(1)}}{\partial b_i^{(2)}} \qquad (5.33)$$

From Equation (5.9), we can find that

$$\frac{\partial n_i^{(1)}}{\partial W_{i,j}^{(1,1)}} = u_j, \;\; \frac{\partial n_i^{(1)}}{\partial W_{i,j}^{(1,2)}} = y_{pj}, \;\; \frac{\partial n_i^{(1)}}{\partial b_i^{(2)}} = 1 \qquad (5.34)$$

We need to find the derivatives $\frac{\partial \widehat{F}}{\partial n_i^{(1)}}$. By using the chain rule again, we obtain

$$
\begin{aligned}
s_i^{(1)} &= \frac{\partial \widehat{F}}{\partial n_i^{(1)}} = \frac{\partial \widehat{F}}{\partial n^{(2)}} \frac{\partial n^{(2)}}{\partial n_i^{(1)}} = \frac{\partial \widehat{F}}{\partial n^{(2)}} \frac{\partial}{\partial n_i^{(1)}} \left(\sum_{j=1}^{S} W_j^{(2,1)} \, a_j^{(1)} + b^{(2)} \right) \qquad (5.35) \\
&= \frac{\partial \widehat{F}}{\partial n^{(2)}} W_i^{(2,1)} \frac{\partial \, a_i^{(1)}}{\partial n_i^{(1)}} = W_i^{(2,1)} \frac{\partial \widehat{F}}{\partial n^{(2)}} \frac{\partial \left[\tanh \left(n_i^{(1)} \right) \right]}{\partial n_i^{(1)}} \\
&= W_i^{(2,1)} \frac{\partial \widehat{F}}{\partial n^{(2)}} \left(1 - \tanh^2 \left(n_i^{(1)} \right) \right) \\
&= W_i^{(2,1)} \left[1 - \tanh^2 \left(n_i^{(1)} \right) \right] s^{(2)}
\end{aligned}
$$

where $s^{(2)}$ has been given in Equation (5.28).

Equation (5.35) shows that the sensitivities are propagated backward through the network from the last to the first layer. Up to this point, we have found the gradients used in the gradient descent algorithm.

Batch Mode Training and Improvement of Backpropagation Algorithm

There are two different ways in which the backpropagation algorithm can be implemented: incremental mode and batch mode. In the incremental mode, the gradients are computed

and the weights and biases are updated after each input is applied to the network.

In the batch mode, the gradients are averaged at the total set of training samples such as the one given in Equation (5.14) to produce a more accurate estimate of the gradients, and the weights and biases of the network are updated only after each epoch, i.e., after the entire training set has been applied to the network.

Although the backpropagation algorithm is a powerful tool to train the network, there are certain drawbacks associated with it. One of the drawbacks is its slow convergence. The backpropagation algorithm is theoretically guaranteed to converge to a solution that minimizes the mean square error so long as the learning rate is not too large. The compensation for the small choice of the learning rate would be longer searching time to find the minimum. Many modifications have been suggested to improve the performance of the backpropagation algorithm. Among them are the use of momentum and the method of variable learning rate. The method of momentum takes into account the previous adjustments to the weights and biases of the network in order to smooth the searching trajectory:

$$\Delta W_{i,j}^{(m,n)}(k) = -\left(1-\gamma\right)\alpha\frac{\partial \widehat{F}}{\partial W_{i,j}^{(m,n)}} + \gamma\Delta W_{i,j}^{(m,n)}(k-1) \tag{5.36}$$

$$\Delta b_{i}^{(m)}(k) = -\alpha\left(1-\gamma\right)\frac{\partial \widehat{F}}{\partial b_{i}^{(m)}} + \gamma\Delta b_{i}^{(m)}(k-1) \tag{5.37}$$

where γ is the momentum coefficient and experimentally determined, and $0 \leq \gamma \leq 1$. When $\gamma = 0$, the above equations reduced to Equations (5.19) and (5.20). The method of variable learning rate changes the learning rate α accordingly. One approach is such that, if the average mean square error over the entire training set increases by more than some set percentage ζ (typically one to five) after a weight update, then the weight update is discarded, the learning rate is decreased by multiplying it with a factor $0 < \eta < 1$, and the momentum coefficient γ (if used) is set to zero. If the mean square error increases by less than ζ, then the weight update is accepted but the learning rate and momentum coefficient remain unchanged. If the mean square error decreases after a weight update,

then the weight update is accepted and the learning rate is increased by multiplying it with a factor $\eta > 1$, and the momentum coefficient is reset to its original value.

There are other algorithms or techniques to train the neural network, which are based on standard numerical optimization techniques. Two common methods are the conjugate gradient algorithm and the Levenberg-Marquardt method. Compared to the traditional backpropagation method, these methods converge faster, but require extra computations. Some of those numerical optimization techniques cannot directly applied to the training of the neural network, certain modifications are required for their use on the network training. Details of these methods can be found in the book by Hagan, etc. [69].

In our simulation, the neural network plant model is trained offline in batch mode by using the neural network toolbox provided in MATLAB$^\circledR$. After being appropriately trained, the network plant model uses previous inputs and previous plant outputs to predict the future values of the plant output for the use in the predictive control scheme.

5.2.2 Predictive Control

The model predictive control scheme is shown in Figure 5-3. The controller consists of the neural network plant model and the optimization block. The optimization block solves for the optimal control signal by minimizing a cost function or performance index over a specified time period or time horizon, then outputs it to the plant. The cost function is typically a quadratic function of the regulation/tracking error and required control inputs. In this dissertation, the cost function is given in the following form:

$$J = \sum_{j=N_1}^{N_2} \left[y_r \left(t + j\Delta t \right) - y_m \left(t + j\Delta t \right) \right]^2 + \xi \sum_{j=1}^{N_u} \left[u' \left(t + (j-1)\Delta t \right) - u' \left(t + (j-2)\Delta t \right) \right]^2$$

$$(5.38)$$

where Δt is the time step size, N_1, N_2, and N_u define the horizons over which the tracking error and the control increments are evaluated, u' is the tentative control signal, y_r is the desired plant response, and y_m is the network model response. The ξ value determines the contribution that the sum of the squares of the control increments has on

the performance index. Without ξ, the controller reduces to a simple minimum-variance controller. But unfortunately such a controller results in an instability issue in the vast majority of digital control practices (see Scott (2000)). Including a nonzero ξ, not only stabilizes the system and, if carefully chosen, does not significantly degrade controller performance, but also prevents sharp jumps in the control signals.

The cost function or performance index J depends only on a set of control sequences starting from time t, $u'\left(t + \left(j - 1\right)\Delta t\right)$, $\left(j = 1, 2, \cdots, N_u\right)$, because the network model output is also a function of this control sequence. In the case when horizon N_2 is greater than N_u, which is very common, the control inputs after the moment of $\left(t + \left(N_u - 1\right)\Delta t\right)$ that are needed to compute the network output y_m are assumed to remain the same as $u'\left(t + \left(N_u - 1\right)\Delta t\right)$.

A step-by-step procedure for the predictive control algorithm is given as follows:

1) Specify a reference plant response y_r for the instant. For flutter suppression, y_r is assumed to be the static response or the equilibrium response of the wing system. In flutter, the wing is oscillating around a certain response that we call the static, or equilibrium, response. When properly damped, the wing approaches the static response.

2) Predict the plant output y_m over the range of future period by using the neural network plant model.

3) Evaluate the performance of a set of trial control inputs according to the cost function (5.38).

4) Repeat steps 2 and 3 with an optimization scheme until the termination criteria are achieved.

5) Output the trial control value selected by the optimization process to the plant.

6) Repeat the entire process at the next instant.

5.3   Numerical Simulations for Flutter Suppression

The HALE aircraft wing cantilevered from the wall of the wind tunnel has been analyzed in Chapter 4. We found that at approximately 105 m/s, the wing experiences limit

cycle oscillations. The simulation for the wing's response without a controller by the aeroelastic analysis code coupled with the general unsteady vortex lattice method can be seen in Figure 4-7. To implement the neural network predictive control, the first stage is the system identification.

We choose a series of control signals with random step sizes and random magnitude within the range between -1 and 1 at each period given in Figure 5-4. At the initial period, there is no control input for the cause to let the response of the wing system becomes well developed through the transient initial period. Shown in this figure, nonzero control signals appear from nondimensional time 600. These control signals are sent to the aeroelastic analysis code to compute the response of the wing. The actuator gain factor K in Equation 5.1 is given as -50. The negative sign is chosen for convenience, and it does not make any difference in the final results. The wing-tip twist is first chosen as the representative for the wing response under the effects of aerodynamic forces and the control inputs. In other words, the wing-tip twist angle represents the plant output in the predictive control model. Figure 5-5 shows the time history of the wing-tip twist at an airstream speed of 105 m/s.

The number of neurons in the first layer of the neural network plant model S is set at 7, and time-delay parameters for the control input and previous plant output, R_1 and R_2, are both chosen to be 2. The control signals along with the history data of the wing-tip twist at each nondimensional time step from nondimensional time 600 to 3000 are used as the training data. Note that the nondimensional time step of the aeroelastic simulation is one; thus there are 2401 sample data points serving as the data pairs shown in Equation (5.14). The training algorithm *tranlm* in MATLAB$^{\circledR}$ is used to train the neural network.

Once the weights and biases are determined from MATLAB$^{\circledR}$, they are saved into a data file, which are used later in the aeroelastic analysis code for predictive control. In the predictive control stage, the optimization procedure built in the aeroelastic analysis code searches for the optimal control signal with the neural network plant model at each time step; this optimal control signal determines the torque generated by the actuator

and enters the iterations in the aeroelastic behavior simulation. Some other parameters of the predictive control are given as $\xi = 0.05$, $N_1 = 1$, $N_2 = 50$, and $N_u = 2$. Figure 5-6 presents the optimal control signal history during the predictive control process. Same as the system identification stage, the controller is turned on at nondimensional time 600. As we can see from the figure, the magnitude of the control signal decays as the time goes, and it should correspond to a decaying oscillation in the response of the wing. Figure 5-7 shows the history of the wing tip twist. Starting from nondimensional time 600, the wing tip twist is decaying. Because of the inertial coupling between twist and bending, it is no surprise that the oscillation of the deflection is suppressed at the same time as it is shown in Figure 5-8.

The solutions with the wing-tip deflection as the plant output are presented in Figure 5-9 - 5-12. Figure 5-9 shows the time history of the wing-tip deflection under the control input shown in Figure 5-4 at the airstream speed of 105 m/s for system identification. The parameters in the neural network model are chosen to be the same as the ones used with the wing-tip twist as the plant output. After the network model is trained, the weights and biases are output to the aeroelastic analysis code. Figures 5-10, 5-11 and 5-12 show the optimal control signals to suppress the limit-cycle oscillations, the time history of the wing-tip deflection, and the time history of the wing-tip twist, respectively. As shown in the figures, oscillations are successfully suppressed, but the wing-tip deflection approaches a higher value than the static or equilibrium position. Comparatively, the neural network predictive control with the wing tip twist as the plant output renders better solution. It is most likely because the control actuator directly adjust the twist of the wing.
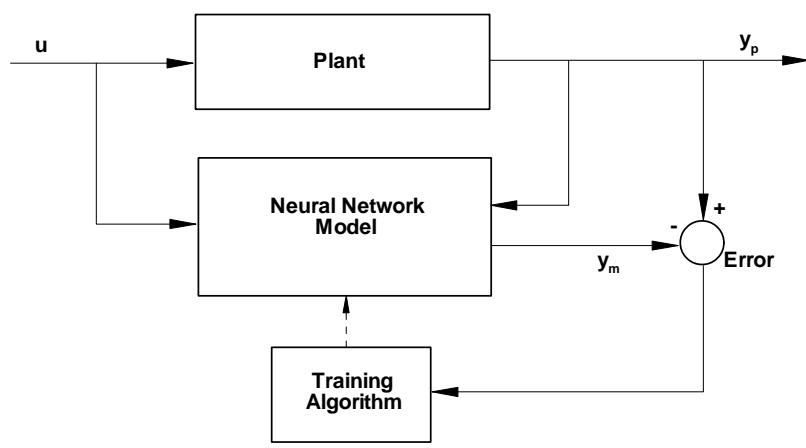
Figure 5-1: System identification diagram
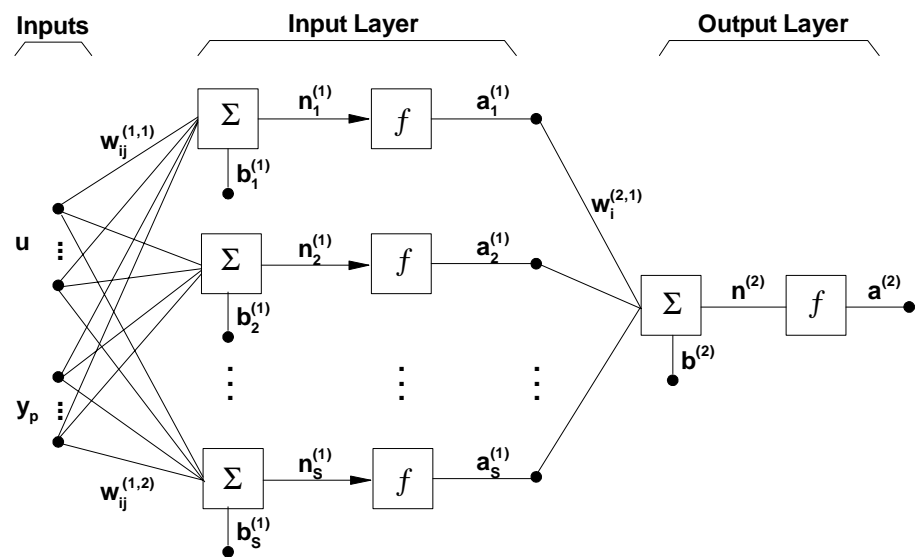
Figure 5-2: Two-layer neural network
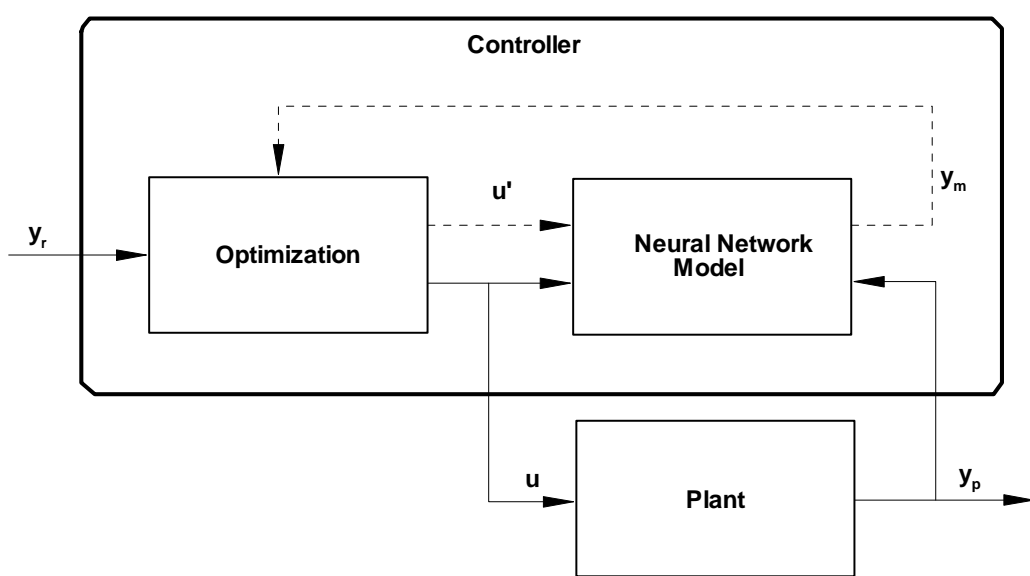
Figure 5-3: Neural network predictive control diagram
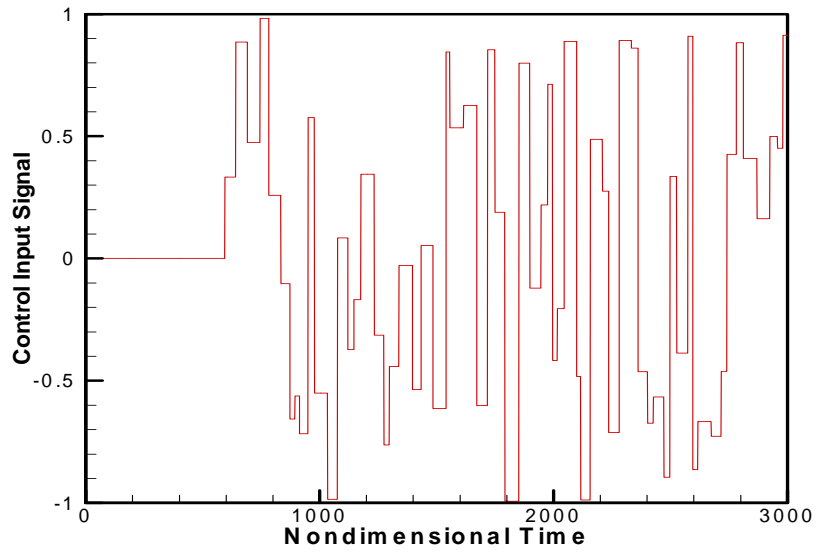
Figure 5-4: The control input signal used for the system identification
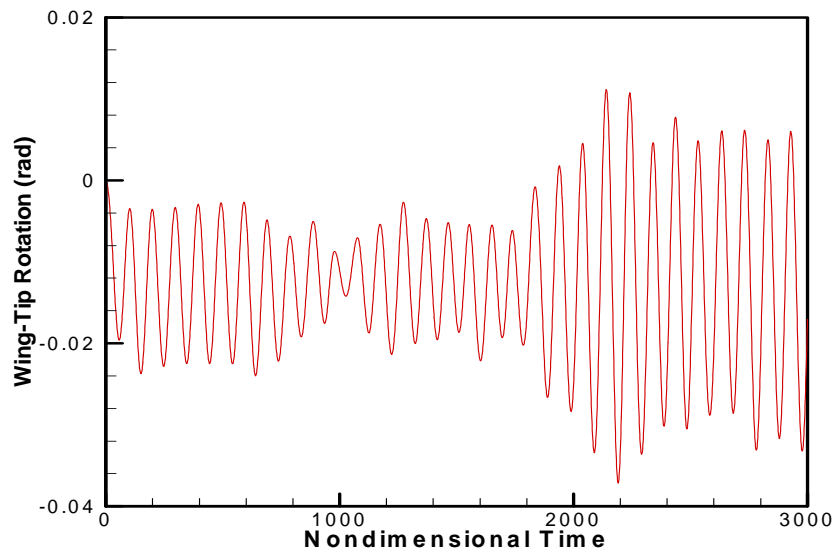
Figure 5-5: Time history of the wing-tip twist angle under the control inputs for the system identification ($V_\infty = 105 \ m/s$)
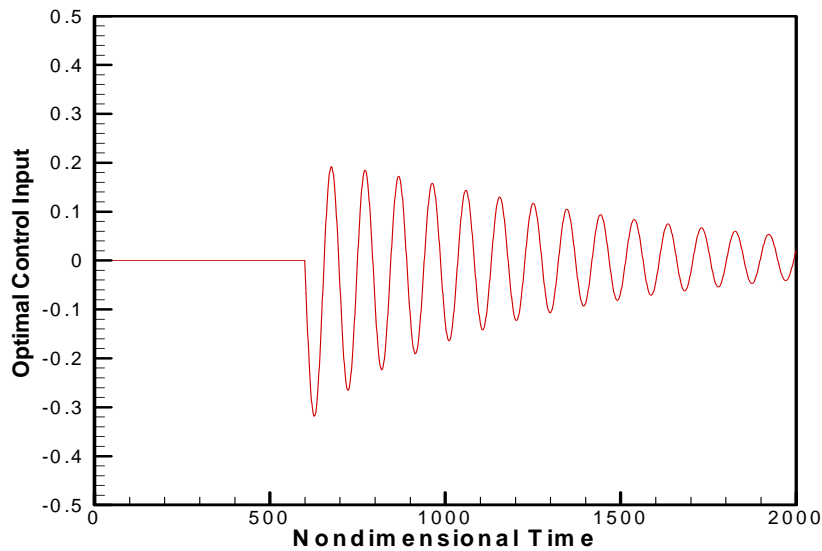
Figure 5-6: The optimal control input with the wing-tip twist representing the plant output
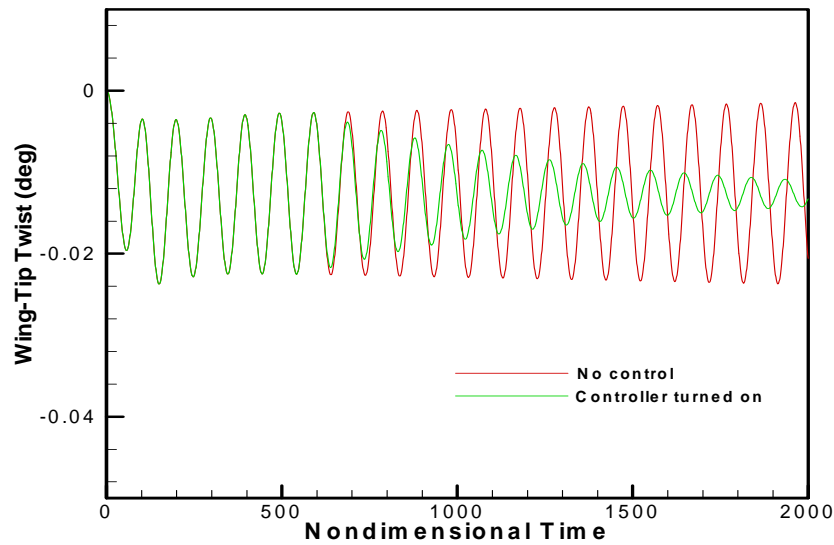
Figure 5-7: Time history of the wing-tip twist without control and with neural network predictive control

161
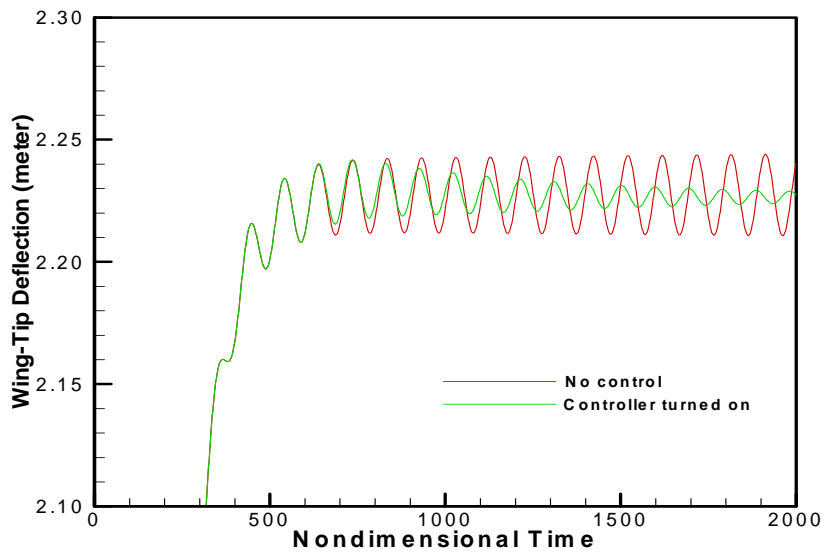
Figure 5-8: Time history of the wing-tip deflection without control and with neural network predictive control
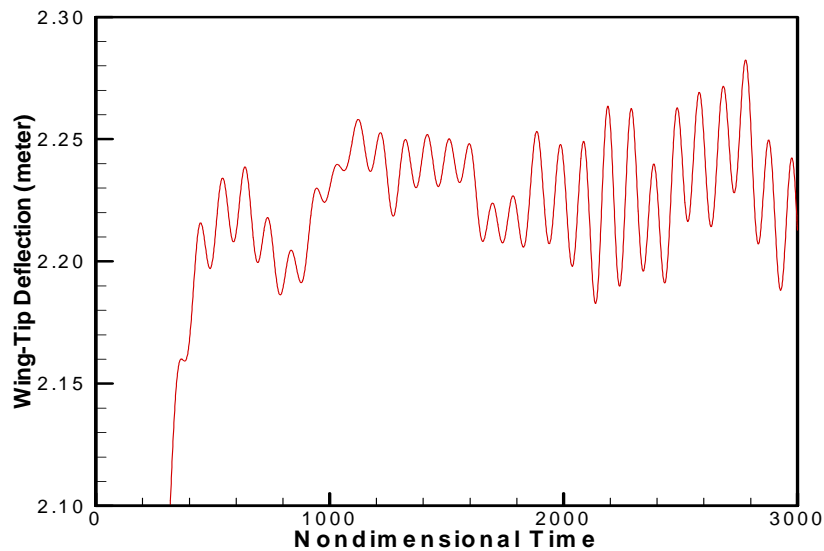
Figure 5-9: Time history of the wing-tip deflection under the control inputs for the system identification ($V_\infty = 105 \ m/s$)
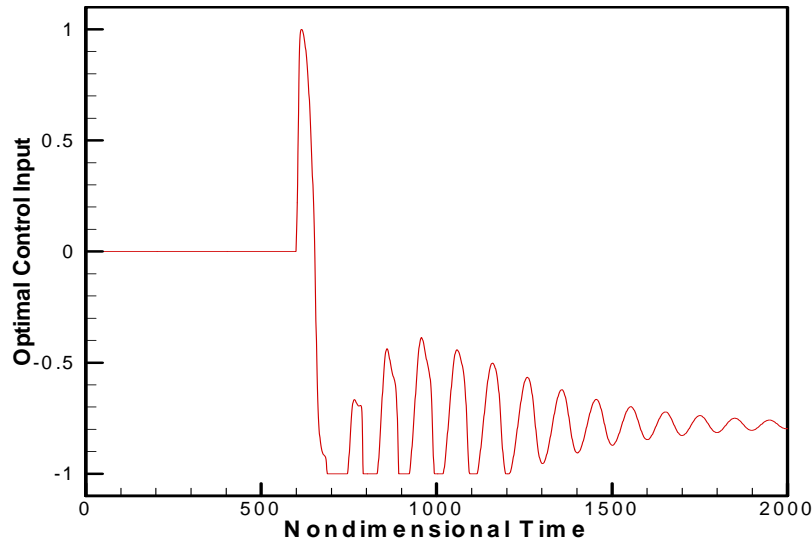
Figure 5-10: The optimal control input with the wing-tip deflection representing the plant output
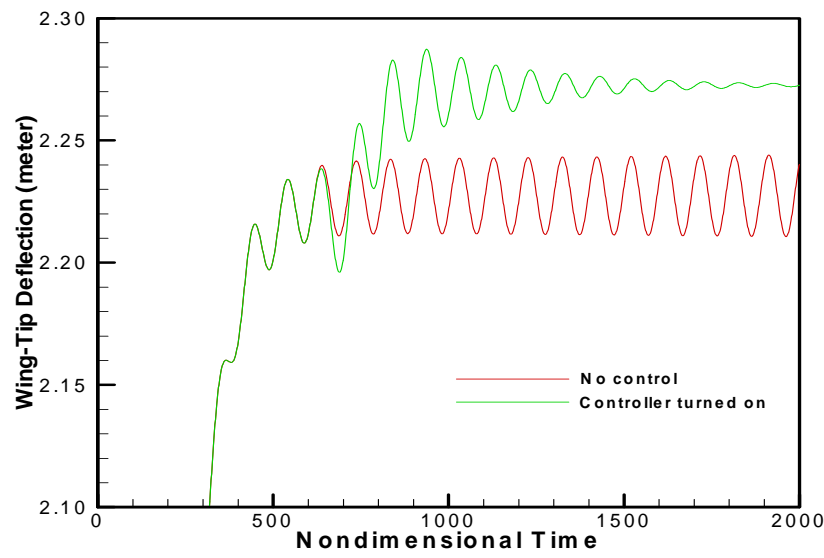
Figure 5-11: Time history of the wing-tip deflection without control and with neural network predictive control

163
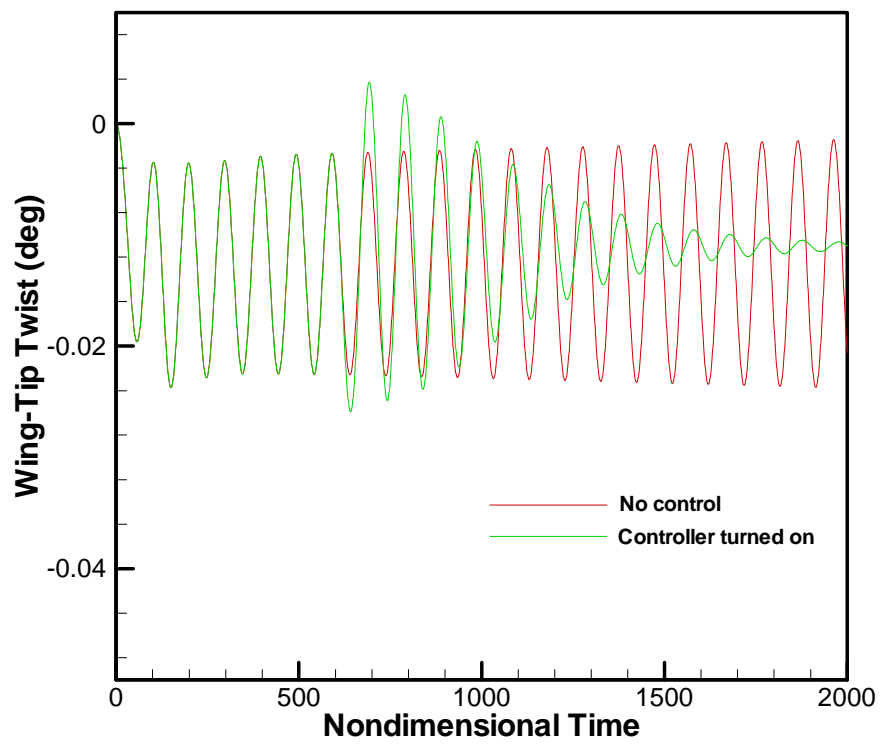
Figure 5-12: Time history of the wing-tip twist without control and with neural network predictive control

Chapter 6

Concluding Remarks

In this chapter the work that has been done in this dissertation is summarized and some remarks regarding further work are made.

6.1 Summary

In this dissertation, the general unsteady nonlinear interactions between aerodynamic forces and wing structures are numerically investigated as integrated dynamic systems, including structural models, aerodynamics, and control systems, in the time domain. A High Altitude Long Endurance (HALE) aircraft wing model's aeroelastic behavior is analyzed as numerical examples in several situations, e.g., when it is cantilevered from the wall of wind tunnel, and when it is mounted on a free-to-roll sting at its mid-span both without and with a center mass simulating a fuselage.

The wing is modeled structurally as an elastic beam, and is extended to include the rigid-body rotation, or the overall system rolling. The governing equations of motion are developed through the extended Hamilton's principle. There are inertial couplings not only between the rigid-body rotation and the elastic deformations, but also between the elastic bending and torsion because the elastic axis is not coincident with the inertial axis of the beam model. The generalized Galerkin approach is used to convert the partial-differential equations of motion into weak forms in terms of integrals, and the

finite element method is implemented to finalize the equations to facilitate our analysis. The reason for choosing the finite-element method to discretize the equations of motion is that the finite element method is fully compatible with the aerodynamic model and the communication between the structural and aerodynamic models is easy. The free vibration problem of the beam model is solved to find the natural frequencies and the natural mode shapes for use in the aeroelastic analysis. With the addition of the rigid body rotation, the asymmetric modes appear along with the symmetric modes.

The aerodynamic forces are found by a general nonlinear unsteady vortex-lattice method. In a high-Reynolds-number flow past a streamlined body, thin boundary layers of highly concentrated vorticity form on the surface, and some vorticity is shed into the flow, usually from sharp edges, and convected away from the body to form the wake, a free-shear layer. We assume the wings are thin and merge the boundary layers on the upper and lower surfaces into a single layer on the camber, or lifting, surface. Every vorticity field has a velocity field associated with it; in fact, vorticity anywhere in the flow field has associated velocity everywhere in the flow field. To expedite the calculation of the velocity field associated with the vorticity in the boundary layers and wakes, we first consider these layers to be surfaces in the mathematical sense (i.e., discontinuities in the components of velocity tangent to the surfaces) and then replace the surfaces of vorticity with lattices of discrete lines of vorticity. For the two-dimensional case there is a theoretical justification for this step; for the three-dimensional case, there are comparisons with experiment, which strongly support its validity.

In the real flow, the velocity associated with the vorticity interacts with the oncoming stream in such a way that the normal component of the velocity of the fluid relative to the body's surface is zero (the no-penetration condition). We imitate reality by imposing the no-penetration condition at a discrete number of points on the lifting surface in order to determine the vorticity distribution in the lattice. The fluid velocity depends on the free stream as well as the vorticity in the boundary layers and the wake; the latter captures the essence of the vorticity-dominated flows.

In addition to the no-penetration condition, we eliminate the difference in the pres-

sures in the air streams that are merging as they come off the upper and lower surfaces along the trailing edge and wing tips. To do this, we convect the line segments of discrete vorticity that lie along these edges into the flow at the local fluid-particle velocity while maintaining the circulations around them constant. At each time step, new segments are shed into the flow, and those already there move a bit farther downstream, a process that provides the force-free shape of, and the distribution of vorticity in, the wake. The aerodynamic forces are computed by using the unsteady Bernoulli's equation.

The aerodynamic code written in Fortran 90 along with OpenMP directives is verified by several numerical examples. The first example considers the flow past a spherically blunted cylinder-cone configuration. The pressure distribution over the body obtained by UVLM is in very good agreement with the experimental results at zero angle of attack and at ± 20 deg. angle of attack. The second example is a mid-wing/single-fuselage configuration. The aerodynamic interference between the wing and fuselage is fully accounted for by the freely deformed wake interactions. The numerical lift coefficients for both the wing alone and the whole configuration are very close to the experimental results for angles of attack below ten degrees. The lift coefficients for the rectangular wings with NACA 23012 airfoil and the normal force spanwise distribution along a flat plate are also analyzed by UVLM. The numerical solutions are well compared to the experimental results.

We implement the vortex-lattice code into some applications, such as the inboard-wing/twin-fuselage configuration and formation flights. Instead of one fuselage located in the center of the configuration, the inboard-wing/twin-fuselage configuration suggests that twin fuselages be placed at the tips of an inboard wing. The original thought that the twin fuselage could achieve two-dimensional flow on the wing by eliminating free wing tips appears to be incorrect. The computed flow in the Trefftz plane indicates a strong vortical flow behind the aircraft, similar to the flow associated with the wing-tip vortex systems of a conventional configuration. The numerical solution shows that the twin fuselages decrease the lift coefficient as well as the lift curve slope when compared with the wing-alone case with aspect ratio of 2, whose span is equal to the distance

between the outerlines of the twin fuselages. If compared with the wing with aspect ratio of 1.7, whose span is equal to the distance between the centerlines of the twin fuselages, the addition of the fuselages do not make much difference to the coefficient of lift.

Configurations consisting of several airplanes flying in close formation are considered for the purpose of improving range or economy. The benefits of formation flight arise from the disturbance-velocity associated with the vorticity shed primarily from the wing tips, thus the flow field for the hitchhiker is dominated by vorticity. Hence, UVLM appears to be a good candidate for modeling this flow field. In this dissertation we demonstrate its capability to accurately model the flow field for two or more wings flying in close formation with several examples. The numerical results show that there can be a lift increase when two or more wings fly together, compared to when they fly alone. The lift increase due to the aerodynamic interference will finally result in a reduction of the induced drag. As for the example with the swept wing and the rectangular wing, the case of two wings docking with their leading edges aligned gives the highest lift increase benefit among the cases that have been analyzed.

To attack the aeroelastic problem, we need to combine the aerodynamic model with the finite-element structural model. The rigid-body rotation and elastic deformations are approximated by an expansion in terms of finite number of the free-vibration modes to reduce the size of the problem, and the time-dependent coefficients in this expansion are used as the generalized coordinates of the entire dynamic system. By assuming the cross sections of the beam model to be rigid, the geometric relationship between the displacements of a point in the aerodynamic grid and the displacements in the finite element nodes can be found. The aerodynamic loads are transferred or mapped from the aerodynamic grid onto the modal space based on the stipulation that the virtual work done by the aerodynamic loads must be equal to that done by the equivalent structural loads. Hamming's fourth-order predictor-corrector algorithm is used to simultaneously integrate the equations of motion for the flowfield and the structure. The scheme is modular so that the models of the flow field and structure can be changed independently without changing the overall algorithm. If the aerodynamic loads are obtained by solving

the Navier-Stokes equations, then it may be more efficient to run the structural and aerodynamic codes with different time steps, which has been done and requires only a very small modification. The overall scheme with any flow model is well-suited for parallel processing.

The stability of the hitchhiker wing in the docking formation flight is firstly analyzed as an example for combining models. The wings are assumed to be rigid bodies, but the hitchhiker wing can rotate along the hinge fixed at the main wing. Numerical solutions confirm the instability associated with the positive yawing angle of the hitchhiker with respect to the main wing, i.e., the hitchhiker is swept forward.

Flutter analysis is conducted for a HALE aircraft wing model. The first three free-vibration modes are found to be sufficient for the case when the wing is considered as a cantilever beam, which corresponds to the semi-span wing cantilevered from the wall of the wind tunnel. The time histories of the generalized modal coordinates show that, at subcritical free-stream speeds, the generalized coordinates as well as the wing tip deformations experience decaying oscillations and finally approach steady status, and that, when the free-stream reaches a certain critical speed, the flutter speed, limit-cycle oscillations are observed. The power spectral densities (PSDs) of Fast Fourier Transforms (FFT) for the histories confirm that all modes are responding at the same frequency when the flutter speed is reached. In addition, at subcritical free-stream speeds, all the modes and the wing tip deformations are eventually found decaying at the same frequency as well. The modal coupling responsible for this common frequency is through the aerodynamic loads. The first six free-vibration modes are used for numerical simulations for the cases with the rolling motion included. Numerical results suggest that mounting a semi-span model on the wall will not give a true indication of the flutter speed. As a consequence of the rigidity added by the wall, the airspeed at flutter for a wall-mounted semi-model will be higher than that for the full-span model.

The final work in this dissertation is implementing the neural network predictive control technique for flutter suppression of a cantilever beam model for the wing. The universal approximation capability of neural networks makes them very suitable for the

identification and control of dynamic systems. In the neural network predictive control (NNPC) technique, the controller uses a neural network model to predict future plant responses to potential control signals. A search algorithm is used to select the best control input that optimizes future plant performance. In our approach, the control force is assumed to be given by an actuator that can apply a distributed torque along the spanwise direction of the wing. The solutions with the wing-tip twist or the wing-tip deflection as the plant output show that the flutter oscillations are successfully suppressed with the neural network predictive control scheme.

6.2   Remarks Regarding Further Work

With the rapid development of computer resources such as computing speed, memory, etc., the numerical analysis for the aeroelastic problem can certainly become more complicated and more delicate regarding both the aerodynamic model and the structural model. The aerodynamic model in this dissertation is limited to incompressible flow. To fully account for the compressibility or the viscosity, the Euler equations or preferably the Navier-Stokes equations must be resorted. The structural model can also be extended to the three-dimensional finite-element model of the whole aircraft and including the use of composite materials. However, the feasibility of complete model analysis does not take away what the present aerodynamic model and aeroelastic simulation algorithm bring us. The effectiveness and accuracy of the general unsteady vortex lattice method can be certainly extended to, but not limited to the following topics:

- Gust response.

- Gust load alleviation.

- New control strategies for flutter suppression.

- Applications in infrastructures such as bridges, tall building with floating foundations.

- Cargolifter stability and flutter.

- Hydrofoils.

- Unsteady ground effects.

- Employing nonlinear structural models for bifurcation analysis.

Bibliography

[1] Anderson J. A., (1972), "A Simple Neural Network Generating An Interactive Memory", *Mathematical Bioscience*, Vol. 14, pp. 197-220.

[2] Atta E. H., Kandil O. A., Mook D. T., and Nayfeh A. H., (1977), "Nonlinear, Unsteady Aerodynamic Loads on Rectangular and Delta Wings", AIAA Paper No. 77-157.

[3] Atta E. H. and Nayfeh A. H., (1978), "Nonlinear Aerodynamics of Wing-Body Combinations", AIAA Paper No. 78-1206, AIAA 11th Fluid and Plasma Dynamics Conference, Seattle, Washington, July 10-12.

[4] Baruh H., (1999), *Analytical Dynamics*, McGraw-Hill, New York.

[5] Benerjee A. K. and Kane T. R., (1989), "Dynamics of A Plate in Large Overall Motion", *Journal of Applied Mechanics*, Vol. 56, pp. 887-892.

[6] Bernelli-Zazzera F. and Lo-Rizzo V., (1997), "Adaptive Control of Space Structures: An Experiment Based on Recurrent Neural Networks", *Proceedings of the Eleventh Symposium on Structural Dynamics and Control*, Blacksburg, VA, May 12-14.

[7] Bernelli-Zazzera F. and Lo-Rizzo V., (1999), "Adaptive Controls of Space Structures via Recurrent Neural Networks", Dynamics and Control, Vol. 9, No. 1, pp. 5-20.

[8] Bernelli-Zazzera F., Mantegazza P., Mazzoni G., and Rendina M., (2000), "Active Flutter Suppression Using Recurrent Neural Networks", *Journal of Guidance, Control, and Dynamics*, Vol. 23, No. 6, pp. 1030-1036.

[9] Bisplinghoff R. L., Ashley H., and Halfman R. L., (1955), *Aeroelasticity*, Dover Publications, Inc., New York.

[10] Blake W. B. and Gingras D. R., (2001), "Comparison of Predicted and Measured Formation Flight Interference Effects", AIAA 2001-4126.

[11] Crespo da Silva M. R. M. and Hodges D. H., (1986), "Nonlinear Flexure and Torsion of Rotating Beams, with Application to Helicopter Rotor Blades - I. Formulation", *Vertica*, Vol. 10, No. 2, pp. 151-169.

[12] Dong B., (1991), "Numerical Simulations of Wakes, Blade-Vortex Interaction, Flutter, and Flutter Suppression by Feedback Control", Ph.D. Thesis, Department of Engineering Science and Mechanics, Virginia Polytechnic Institute and State University, Blacksburg, VA.

[13] Dowell E. H., Crawley E. F., Curtiss H. C., Peters Jr., D. A., Scanlan R. H., and Sisto F., (1995), *A Modern Course in Aeroelasticity*, 3rd Edition, Kluwer Academic Publishers, The Netherlands.

[14] Elzebda J. M., Mook D. T., and Nayfeh A. H., (1985), "Unsteady Aerodynamic Interference for Lifting Surfaces", AIAA Paper No. 85-1801.

[15] Elzebda J. M., (1987), "Two-Degree-of-Freedom Subsonic Wing Rock and Nonlinear Aerodynamic Interference", Ph.D. Thesis, Department of Engineering Science and Mechanics, Virginia Polytechnic Institute and State University, Blacksburg, VA.

[16] Elzebda J. M., Mook D. T., and Nayfeh A. H., (1989), "Influence of Pitching Motion on Subsonic Wing Rock of Slender Delta Wings", *Journal of Aircraft*, Vol. 26, No. 6, pp. 503-508.

[17] Elzebda J. M., Mook D. T., and Nayfeh A. H., (1994), "Numerical Simulation of Steady and Unsteady, Vorticity-Dominated Aerodynamic Interference", *Journal of Aircraft*, Vol. 31, No. 5, pp. 1031-1036.

[18] Fung Y. C., (1955), *An Introduction to the Theory of Aeroelasticity*, Dover Publications, Inc., New York.

[19] Gingras D. R. and Player J. L., (2001), "Static and Dynamic Wind Tunnel Testing of Air Vehicles in Close Proximity", AIAA 2001-4137.

[20] Hagan M. T., Demuth H. B., and Beale M., (1995), *Neural Network Design*, PWS Publishing Company, Boston, MA.

[21] Hall B.D., (1999), "Numerical Simulation of the aeroelastic response of an Actively Controlled Flexible Wing", Master thesis, Virginia Polytechnic Institute and State University.

[22] Hall B. D., Mook D. T., Nayfeh A. H., and Preidikman S., (2001), "A Novel Strategy for Suppressing the Flutter Oscillations of Aircraft Wings", *AIAA 2000-0904* and *AIAA Journal*, vol. 39, No. 10, pp.1843-1850.

[23] Haykin S., (1994), *Neural Networks-A Comprehensive Foundation*, Macmillan College Publishing Company, New York.

[24] Helmholtz H. von, (1858), "On Integrals of the Hydrodynamic Equations which Express Vortex Motion", translation by P. G. Tait, 1867, *Philosophical Magazine*, Vol. 4.

[25] Herbert H. E., and Lamar J. E., (1982), "Production Version of the Extended NASA-Langley Vortex Lattice FORTRAN Computer Program", Vol. II, Source Code, NASA TM 83304.

[26] Hopfield J. J., (1982), "Neural Networks and Physical Systems with Emergent Collective Computational Abilities", *Proceedings of the National Academy of Science*, Vol. 79, pp. 2554-2558.

[27] Hough G. R., (1973), "Remarks on Vortex-Lattice Methods", *Journal of Aircraft*, Vol. 10, No. 5, pp. 314-317.

[28] Johnson W. E., (1963), "Experimental Investigation and Correlation with Theory of The Surface Pressure Distribution on Several Sharp and Blunted Cones for Incompressible Flow", Master thesis, University of Washington.

[29] Kandil O. A., (1974), "Prediction of the Steady Aerodynamic Loads on Lifting Surfaces Having Sharp-Edge Separation", Ph.D. Thesis, Department of Engineering Science and Mechanics, Virginia Polytechnic Institute and State University, Blacksburg, VA.

[30] Kandil O. A., Mook D. T., and Nayfeh A. H., (1976), "Nonlinear Prediction of the Aerodynamic Loads on Lifting Surfaces", *Journal of Aircraft*, Vol. 13, pp. 22-28.

[31] Kane T. R., Ryan R. R., and Benerjee A. K., (1987), "Dynamics of A Cantilever Beam Attached to A Moving Base", *Journal of Guidance, Control, and Dynamics*, Vol. 10, pp. 139-151.

[32] Karamcheti K., (1980), *Principle of Ideal-Fluid Aerodynamics*, Krieger Publishing Company, Malabar, FL.

[33] Karkehabadi R., (1995), "Numerical Simulations of Wings in Unsteady Flows", Ph.D. Thesis, Department of Engineering Science and Mechanics, Virginia Polytechnic Institute and State University, Blacksburg, VA.

[34] Kaza K. R. and Kvaternik R. G., (1977), "Nonlinear Aeroelastic Equations for Combined Flapwise Bending, Chordwise Bending, Torsion and Extension of Twisted Nonuniform Rotor Blades in Forward Flight", NASA TM 74059.

[35] Kim M. J., (1985), "Application of Panel Methods for Subsonic Aerodynamics", Ph.D. Thesis, Department of Engineering Science and Mechanics, Virginia Polytechnic Institute and State University, Blacksburg, VA.

[36] Kim M. J. and Mook D. T., (1986), "Application of Continuous Vorticity Panels to General Unsteady Incompressible Two-Dimensional Lifting Flows", *Journal of Aircraft*, Vol. 23, No. 6, pp. 464-471.

[37] Kohonen T., (1972), "Correlation Matrix Memories", *IEEE Transactions on Computers*, Vol. 21, pp. 353-359.

[38] Konstadinopoulos P., Mook D. T., and Nayfeh A. H., (1983), "Numerical Simulation of the Subsonic Wing-Rock Phenomenon", AIAA Paper No. 83-2115.

[39] Konstadinopoulos P., (1984), "Numerical Simulation of the Subsonic Wing-Rock Phenomenon", Ph.D. Thesis, Department of Engineering Science and Mechanics, Virginia Polytechnic Institute and State University, Blacksburg, VA.

[40] Konstadinopoulos P., Mook D. T., and Nayfeh A. H., (1985), "Subsonic Wing Rock of Slender Delta Wings", *Journal of Aircraft*, Vol. 22, No. 3, pp. 223-228.

[41] Lamar J. E., and Gloss B. B., (1975), "Subsonic Aerodynamic Characteristics of Interacting Lifting Surfaces With Separated Flow Around Sharp Edges Predicted by a Vortex-Lattice Method", NASA TN D-7921.

[42] Lamar J. E., and Herbert H. E., (1982), "Production Version of the Extended NASA-Langley Vortex Lattice FORTRAN Computer Program", Vol. I, User's Guide, NASA TM 83303.

[43] Levin D. and Katz J., (1982), "Dynamic Load Measurements with Delta Wings Undergoing Self-Induced Roll-Oscillations", AIAA Paper No. 82-1320, AIAA 9th Atmospheric Flight Mechanics Conference, San Diego, CA.

[44] Liut D. A., (1999a), "Neural-Network and Fuzzy-Logic Learning and Control of Linear and Nonlinear Dynamic Systems", Ph.D. Thesis, Department of Engineering Science and Mechanics, Virginia Polytechnic Institute and State University, Blacksburg, VA, 1999.

[45] Liut D. A., Matheu E. E., Singh M. P., and Mook D. T., (1999b), "A Modified Gradient-Search Training Technique for Neural-Network Structural Control", *Journal of Vibration and Control*.

[46] Magill S., (2000), "Progress Report on Stability Tunnel and Computer Panel Method of Large Civil Transport", Department of Aerospace and Ocean Engineering, Virginia Polytechnic Institute and State University.

[47] Margason R. J. and Lamar J. E., (1971), "Vortex-Lattice FORTRAN Program for Estimating Subsonic Aerodynamic Characteristics of Complex Planforms", NASA TN D-6142.

[48] McCulloch W. and Pitts W., (1943), "A Logical Calculus of The Ideas Immanent in Nervous Activity", *Bulletin of Mathematical Biophysics*, Vol. 5, pp. 115-133.

[49] Meirovitch L. and Nelson H. D., (1966), "On the High-Spin Motion of a Satellite Containing Elastic Parts", *Journal of Spacecraft and Rockets*, Vol. 3, No. 11, pp. 1597-1602.

[50] Meirovitch L., (1991), "Hybrid State Equations of Motion for Flexible Bodies in Terms of Quasi-Coordinates", *Journal of Guidance, Control, and Dynamics*, Vol. 14, No.5, pp. 1008-1013.

[51] Meirovitch L., (1993), "Derivation of Equations for Flexible Multibody Systems in Terms of Quasi-Coordinates from the Extended Hamilton's Principle", *Journal of Shock and Vibration*, Vol. 1, Issue 2, pp. 107-119.

[52] Meirovitch L. and Stemple T. J., (1995), "Hybrid Equations of Motions for Flexible Multibody Systems Using Quasi-Coordinates", *Journal of Guidance, Control, and Dynamics*, Vol. 18, No. 4, pp. 678-688.

[53] Meirovitch L., (1997), "A Unified Theory for Flight Dynamics and Aeroelasticity of Whole Aircraft", *Proceedings of the Eleventh Symposium on Structural Dynamics and Control*, Blacksburg, VA, May 12-14.

[54] Meirovitch L. and Tuzcu I., (2001), "Multidisciplinary Approach to the Modeling of Flexible Aircraft", *International Forum on Aeroelasticity and Structural Dynamics*, Madrid, Spain, June 5-7.

177

[55] Meirovitch L. and Tuzcu I., (2002), "Integrated Approach to Flight Dynamics and Aeroservoelasticity of Whole Flexible Aircraft-Part 1: System Modeling", AIAA paper No. 2002-4747, *AIAA Guidance, Navigation, and Control Conference and Exhibit*, Monterey, CA, August 5-8.

[56] Mook D. T. and Maddox S. A., (1974), "An extension of a Vortex-Lattice Method to Include the Effects of Leading-Edge Separation", *Journal of Aircraft*, Vol. 11, No. 2, pp. 127-128.

[57] Mook D. T. and Dong B., (1994), "Perspective: Numerical Simulations of Wakes and Blade Vortex Interaction", *Journal of Fluids Engineering*, Vol. 116, pp. 5-21.

[58] Mracek C. P. and Mook D. T., (1991), "Aerodynamic Potential Flow Panel Method Coupled with Dynamics and Controls", AIAA Paper No. 91-2846, AIAA Atmospheric Flight Mechanics Conference, New Orleans, LA, August 12-14.

[59] Mracek C. P., (1988*a*), "A Vortex Panel Method for Potential Flows with Applications to Dynamics and Controls", Ph.D. Thesis, Department of Engineering Science and Mechanics, Virginia Polytechnic Institute and State University, Blacksburg, VA.

[60] Mracek C. P. and Mook D. T., (1988*b*), "Numerical Simulation of Three-Dimensional Lifting Flows by a Vortex Panel Method", AIAA Paper No. 88-4336-CP, *AIAA Atmospheric Flight Mechanics Conference*, Minneapolis, MN.

[61] Narendra K. S. and Parthasarathy K., (1991), "Gradient Methods for the Optimization of Dynamic Systems Containing Neural Networks", IEEE Transactions on Neural Networks, Vol. 2, No. 2, pp. 252-262.

[62] Natarajan A., Kapania R. K., and Inman D. J., (2002), "Dynamic Aeroelastic Response of Adaptable Airfoils Using Neural Networks", AIAA paper No. 2002-5599, *The 9th AIAA/ISSMO Symposium on Multidisciplinary Analysis and Optimization*, Atlanta, GA, Sep. 4-6.

[63] Nayfeh A. H., Mook D. T., and Yen A., (1979), "The Aerodynamics of Small Harmonic Oscillations Around Large Angles of Attack", AIAA Paper No. 79-1520.

[64] Nguyen L. T., Gilbert W. P., Gera J., Iliff K. W., and Enevoldson E. K., (1980), "Applications of High-α Control Systems Concepts to a Variable Sweep Fighter Airplane", AIAA Paper No. 80-1582, AIAA Atmospheric Flight Mechanics Conference, Danvers, MA, August 11-13.

[65] Nguyen L. T., Yip L., and Chambers J. R., (1981), "Self-Induced Wing Rock of Slender Delta Wings", AIAA Paper No. 81-1883, AIAA Atmospheric Flight Mechanics Conference, Albuquerque, N. Mexico, August 19-21.

[66] Nuhait A. O., (1988), "Numerical Simulation of Wing in Steady and Unsteady Ground Effects", Ph.D. Thesis, Department of Engineering Science and Mechanics, Virginia Polytechnic Institute and State University, Blacksburg, VA.

[67] Nuhait A. O. and Mook D. T., (1989), "Numerical Simulation of Wings in Steady and Unsteady Ground Effects", *Journal of Aircraft*, Vol. 26, No. 12, pp. 1081-1089.

[68] Ormiston R. A., (1988), "Survey of Army/NASA Rotorcraft Aeroelastic Stability Research", NASA TM 101026.

[69] Orr M., Magill S., Schetz J., Marchman J., Mason W., and Grossman B., (2001), "An Experimental Study of the Aerodynamics of the Inboard Wing Concept", AIAA paper No. 2001-0577.

[70] Peckham D. H., (1958), "Low-Speed Wing-Tunnel Tests on a Series of Uncambered Slender, Pointed Wings with Sharp Edges", R&M 3186, British Aeronautical Research Council, London.

[71] Preidikman S., (1998), "Numerical Simulations of Interactions Among Aerodynamics, Structural Dynamics, and Control Systems", Ph.D. Thesis, Department of Engineering Science and Mechanics, Virginia Polytechnic Institute and State University, Blacksburg, VA.

[72] Preidikman S. and Mook D. T., (2000), "Time-Domain Simulation of Linear and Nonlinear Aeroelastic Behavior", *Journal of Vibration and Control*, Vol. 6, pp. 1135-1175.

[73] Rao J., (1992), *Advanced Theory of Vibrations*, Wiley, New York.

[74] Rosenblatt F., (1958), "The Perceptron: A Probabilistic Model for Information Storage and Organization in The Brain", *Psychological Review*, Vol. 65, pp. 386-408.

[75] Rumelhart D. E. and McClelland J. L., (1986), eds., *Parallel Distributed Processing: Explorations in the Microstructure of Cognition, Vol. 1, Cambridge, MA: MIT Press*.

[76] Schlichting H. and Truckenbrodt E., (1979), *Aerodynamics of the Airplane*, translated by H. J. Ramm, McGraw-Hill.

[77] Scholz N., (1949), "Kraft und Drckverteilungsmessungen an Tragflächen kleiner Streckung", *Forsharb. Ing Wes.*, 16, pp. 85-92.

[78] Scott R. C. and Pado L. E., (2000), "Active Control of Wind-Tunnel Model Aeroelastic Response Using Neural Networks", *Journal of Guidance, Control, and Dynamics*, Vol. 23, No. 6, pp. 1100-1108.

[79] Spearman M. L. and Feigh K. M., (1998), "An Airplane Configuration with an Inboard Wing Mounted Between Twin Fuselages", AIAA paper No. 98-0440.

[80] Suykens J. A. K., Vandewalle J. P. L., and De Moor B. L. R., (1996), *Artificial Neural Networks for Modelling and Control of Nonlinear Systems*, Kluwer Academic Publishers, Boston, MA.

[81] Sarpkaya T., (1989), "Computational Methods with Vortices - The 1988 Freeman Scholar Lecture", *Journal of Fluids Engineering*, Vol. 111, pp. 5-52.

[82] Simo J. C. and Vu Quoc L., (1986), "On The Dynamics of Flexible Beams Under Large Overall Motions-The Plane Case: Parts I, II", *Journal of Applied Mechanics*, Vol 53, pp. 849-863.

[83] Simo J. C., (1985), "A Finite Strain Beam Formulation, The Three Dimensional Dynamics Problem, Part I", *Computer Methods in Applied Mechanics and Engineering*, Vol. 49, pp. 55-70.

[84] Strganac T. W. and Mook D. T., (1986), "Application of the Unsteady Vortex-Lattice Method to the Nonlinear Two-Degree-of-Freedom Aeroelastic Equations", AIAA Paper No. 86–0867-CP, *AIAA/ASME/ASCE/AHS 27th Structures, Structural Dynamics, and Materials Conference*, San Antonio, TX.

[85] Strganac T. W. and Mook D. T., (1987*a*), "A New Method to Predict Unsteady Aeroelastic Behavior", AIAA Paper No. 87-0736, *AIAA 28th Structures, Structural Dynamics, and Materials Conference*, April 6-8.

[86] Strganac T. W. and Mook D. T., (1987*b*), "The Numerical Simulation of Subsonic Flutter", AIAA Paper No. 87-1428, *AIAA 19th Fluid Dynamics, Plasma Dynamics and Laser Conference*, Honolulu, Hawaii, June 8-10.

[87] Strganac T. W., (1987*c*), "A Numerical Model of Unsteady, Subsonic Aeroelastic Behavior", Ph.D. Thesis, Department of Engineering Science and Mechanics, Virginia Polytechnic Institute and State University, Blacksburg, VA.

[88] Strganac T. W. and Mook D. T., (1990), "Numerical Model of Unsteady Subsonic Aeroelastic Behavior", *AIAA Journal*, Vol. 28, No. 5, pp. 903-909.

[89] Theodorsen T., (1935), "General Theory of Aerodynamic Instability and the Mechanism of Flutter", NACA Report 496.

[90] Theodorsen T. and Garrick I. E., (1940), "Mechanism of Flutter, a Theoretical and Experimental Investigation of the Flutter Problem", NACA Report 685.

[91] Thrasher D. F., Mook D. T., Kandil O. A., and Nayfeh A. H., (1977), "Application of the Vortex-Lattice Concept to General, Unsteady Lifting-Surface Problems", AIAA Paper No. 77-1157.

[92] Thrasher D. F., (1979), "Nonlinear Unsteady Aerodynamics with Application to Dynamic-Aerodynamic Interaction", M.S. Thesis, Department of Engineering Science and Mechanics, Virginia Polytechnic Institute and State University, Blacksburg, VA.

[93] Wang Z., Magill S., Preidikman S., Mook D. T. and Schetz J., (2001), "A Numerical and Experimental Aerodynamic Analysis of An Inboard-Wing/Twin-Fuselage Configuration", AIAA 2001-2431, The 19th Applied Aerodynamics Conference, Anaheim, CA, June 11-14.

[94] Wang Z. and Mook D. T., (2003a), "Numerical Aerodynamic Analysis of Formation Flight", AIAA paper No. 2003-610, The 41st Aerospace Sciences Meeting and Exhibit, Reno, Nevada, January 6-9.

[95] Wang Z., Preidikman S., Hall B., Mook D. T., and Nayfeh A., (2003b), "Time-domain Simulation of Nonlinear, Subsonic, Unsteady Aeroelastic Behavior", International Forum on Aeroelasticity and Structural Dynamics (IFASD 2003), June 4-6, Amsterdam, The Netherlands.

[96] Wagner C. G., Jacques L. D., Blake B., and Pachter M., (2001), "An Analytical Study of Drag Reduction in Tight Formation Flight", AIAA 2001-4075.

[97] Widrow B. and Hoff M. E., (1960), "Adaptive Switching Circuit", *1960 IRE WESCON Convention Record, New York: IRE Part 4*, pp. 96-104.

[98] Wieselsberger C., (1922), "Wing Resistance Near the Ground", NACA TM 77.

[99] Yoo H. H., Ryan R. R., and Scott R. A., (1995), "Dynamics of Flexible Beams Undergoing Overall Motions", *Journal of Sound and Vibration*, Vol. 181, pp. 261-278.

Vita

Zhicun Wang was born on August 8, 1969 in Guang-Shan, Henan Province, China. He entered in the Department of Mechanics at Peking University in the fall of 1986 and earned his Bachelor of Science degree in July 1990. He completed his Master of Science degree from the Fourth Academy of China Aerospace Industry Ministry in March 1993, and then joined the 41st Institute of China Aerospace Industry Cooperation (CASC) as a mechanical engineer working in the group of Structural Integrity of Solid Grains. He analyzed propellant grains under various loading conditions by the Finite Element Method. In the fall of 1999, Mr. Wang started his Ph.D. program in the Department of Engineering Science and Mechanics at Virginia Polytechnic Institute and State University. He completed all the requirements for his Ph.D. in Engineering Mechanics in May 2004.